INFORMATION TO USERS

This manuscript has been reproduced from the microfilm master. UMI films the text directly from the original or copy submitted. Thus, some thesis and dissertation copies are in typewriter face, while others may be from any type of computer printer.

The quality of this reproduction is dependent upon the quality of the copy submitted. Broken or indistinct print, colored or poor quality illustrations and photographs, print bleedthrough, substandard margins, and improper alignment can adversely affect reproduction.

In the unlikely event that the author did not send UMI a complete manuscript and there are missing pages, these will be noted. Also, if unauthorized copyright material had to be removed, a note will indicate the deletion.

Oversize materials (e.g., maps, drawings, charts) are reproduced by sectioning the original, beginning at the upper left-hand corner and continuing from left to right in equal sections with small overlaps.

ProQuest Information and Learning
300 North Zeeb Road, Ann Arbor, MI 48106-1346 USA
800-521-0600

UMI®

NMR STUDIES OF INTERCALATION MATERIALS FOR LITHIUM ION BATTERIES

by

XIAODONG GUO

A dissertation submitted to the Graduate Faculty in Physics in partial fulfillment of the requirements for the degree of Doctor of Philosophy,
The City University of New York

2003

UMI Number: 3083669

UMI Microform 3083669

ProQuest Information and Learning Company
300 North Zeeb Road
P.O. Box 1346
Ann Arbor, MI 48106-1346

This manuscript has been read and accepted for the Graduate Faculty in Physics in satisfaction of the dissertation requirement for the degree of Doctor of Philosophy.

4/28/03 — Date

Professor Steve G.Greenbaum, Ph.D., Chair of Examining Committee

4/28/03 — Date

Professor Sultan Catto, Ph.D., Executive Officer

Professor Marten denBoer, Ph.D.

Professor Ying-Chih Chen, Ph.D.

Professor Tatyana Polenova, Ph.D.

Professor Phillip Stallworth, Ph.D.

The City University of New York

Abstract

NMR STUDIES OF INTERCALATION MATERIALS FOR LITHIUM ION BATTERIES

By

Xiaodong Guo

Advisor: Professor Steve G. Greenbaum, Ph.D.

Although lithium ion batteries have been commercially available products, there are still a lot of unsolved questions stimulating basic materials research with the aim of further improving their properties. The goals include: higher capacity for lithium uptake; higher lithium diffusivity for higher discharge current; greater chemical and electrochemical stability and structural stability over a wider range of lithiation. Understanding the correlation between the structural and electrochemical properties of electrode materials is a key step to improve the performance of the batteries. These studies are often hampered by the lack of long-range order found only in well-defined crystalline phase. Nuclear magnetic resonance (NMR) spectroscopy is an ideal method and one of a few very powerful tools for exploring local structural and electronic environment of ions such as Li^+ ions in lithium ion battery electrode materials due to the high NMR sensitivity of the naturally abundant ^7Li nucleus.

Both pristine and partially oxidized graphite exhibit three ^7Li resonances corresponding to different reversible Li sites associated with high and low lithiation levels. The population of Li bonded to edge sites is enhanced in the partially

oxidized graphite, and increasing lithiation results in host structural rearrangement converting the edge-site Li into intercalated Li.

One of the primary failure mechanics believed to occur in the cells is the formation of a passivating layer on the positive electrode that eventually leads to a loss of electrical contact between active cathode particles. The ^{7}Li NMR spectra demonstrate the presence of a solid electrolyte interface (SEI), characterized by a relatively featureless absorption centered at 0 ppm. The SEI growth has been quantitatively monitored by integrating the spectral intensities of the SEI feature.

^{7}Li NMR spectra show at least two local phases that cannot be distinguished by X-ray diffraction (XRD) measurement for cation-substituted (Fe,Co) $LiNiO_2$. Substituting Fe for Ni creates larger local structure distortion.

Two sets of $LiCo_xNi_{1-x}VO_4$ samples prepared via two different methods are studied by ^{7}Li and ^{51}V NMR. The cation distribution is obtained by analyzing the ^{51}V NMR spectra; the results are different from the XRD data result. Deviation from ideal inverse spinel structure is observed.

ACKNOWLEDGMENTS

I would like to express my sincere gratitude towards my advisor, Dr. Steve Greenbaum, whose expertise, understanding, and patience, added considerably to my graduate experience. This thesis would not have been possible without his invaluable guidance and support.

I would like to thank the other members of my committee, Dr. Marten denBoer, Dr. Ying-Chih Chen, Dr. Tatyana Polenova and Dr. Phillip Stallworth for taking time out from their busy schedule to participate in the examination committee and read my thesis.

I would also like to thank Dr.V.Yufit and Dr.E.Peled at Tel Aviv University, Dr.Jun Liu and Dr.Khalil Amine at Argonne National Laboratory, Dr.Fabio Ronci and Dr.Bruno Scrosati at University of Rome, Dr. Marcella Arrabito at Politecnico di Torino for providing samples for NMR measurements.

Special thanks goes out to Dr. Yifeng Wang, Dr.Phillip Stallworth and Dr. Song H. Chung, for their help in learning NMR technique, performing experiments and discussing the measurements.

I would also like to thank all the other members at NMR lab, Hunter College of CUNY and all the people who have helped me during this work.

I dedicate this paper to my family for the support they provided me and in particular I must acknowledge my wife, without whose love and encouragement, I would not have finished this thesis.

This research was supported, in part, by grants from the U.S. Department of Energy, Division of Basic Energy Sciences.

Table of Contents

List of Tables

List of Figures

CHAPTER 1

Introduction

1.1 Application and advantages of Lithium batteries

Batteries energize a diverse range of devices, from mobile computing, communications applications, electric vehicles, satellites, microelectronics, cordless power tools, camcorders and a multitude of other applications that are so essential for modern living. The continuing and growing need for energy-efficient devices and concerns about environmental degradation call for concerted measures to conserve, store, and develop non-polluting energy storage devices. Advanced battery technology is a practical way to address issues related to energy storage.

A number of battery-making technologies have evolved during the past century. The traditional battery workhorse - the lead-acid battery - has adequately served the technological needs of a variety of industries. Other battery types, such as nickel-cadmium and nickel-metal-hydride, have also fulfilled the demands of niche products and systems. However, these battery chemistries possess low power and energy densities, inflict environmental damage, and are expensive. These concerns have driven research and development efforts toward an advanced type of battery chemistry, popularly known as lithium batteries.

Lithium is the lightest metal, has the greatest electrochemical potential and provides the largest energy content. Rechargeable batteries using lithium are capable

of providing both high voltage and capacity, resulting in an extraordinary energy density.

A lithium power source offers a significant advantage if:

- A high voltage is needed (i.e. 3.0 to 3.9 volts per cell)
- The power source has to be as light weight as possible
- Long shelf life is required
- A wide temperature range is required
- Reliability is crucial
- High energy density is needed

1.2 Lithium ion battery background

The lithium metal battery was first developed by G.N.Lewis in 1912. It was not until the 1970s that the first single-use commercial lithium batteries were made available. Rechargeable lithium metal batteries were commercialized in the 1980s but did not reach a wide commercial market. The main reason for the commercial limitations is safety concerns. The cells are susceptible to shorts from lithium dendrites that grow during use, increasing the total surface area of Li and leading to thermal runaway. As the cell temperatures approach the melting temperature of lithium, violent reactions take place with the flammable electrolyte. Passivation at lithium surface also limits the cyclability of the entire battery.

To overcome the problem, host materials for storing and exchanging a large quantity of lithium ions have been examined as alternative electrodes for the pure metallic lithium anode.

Rather than lithium precipitating and dissolving as in the conventional systems, the electrochemical process at the anode is the intercalation and deintercalation of lithium ions during charge and discharge, respectively. If the cathode is also a nonmetal lithium ion accepting compound, the lithium ions are "rocking" from negative electrode to positive electrode. This kind of lithium concentration cells have been termed "rocking chair battery".[1,2] Based on this novel concept, a major Japanese battery company developed cells using petroleum coke, Li_xC_6, as the anode electrode in the early of 1990's. T.Nagaura et al [3] named this cell "Lithium ion rechargeable battery", which is now the generally used term for all lithium rechargeable batteries using the rocking chair concept. The scheme of a typical lithium ion battery is shown in Figure 1-1.

The cell is made up of a coke (carbons with limited crystalline structure) or graphite negative electrode , an electrolyte which serves as an ionic path between electrodes and separates the two materials, and a metal oxide (such as $LiCoO_2$) positive electrode.

1.3 Intercalation materials for lithium ion batteries

The battery can be symbolized as:

$$A^-/El_i/C^+$$

Where A^- is the anode, El_i is the electrolyte and C^+ the cathode. The electrolyte, El_i, is an ionic conductor and an electronic insulator. The low electronic conductivity prevents self-discharge of the cell. The electrolyte is also a physical separator between electrodes. In this thesis, electrolyte will not be discussed further.

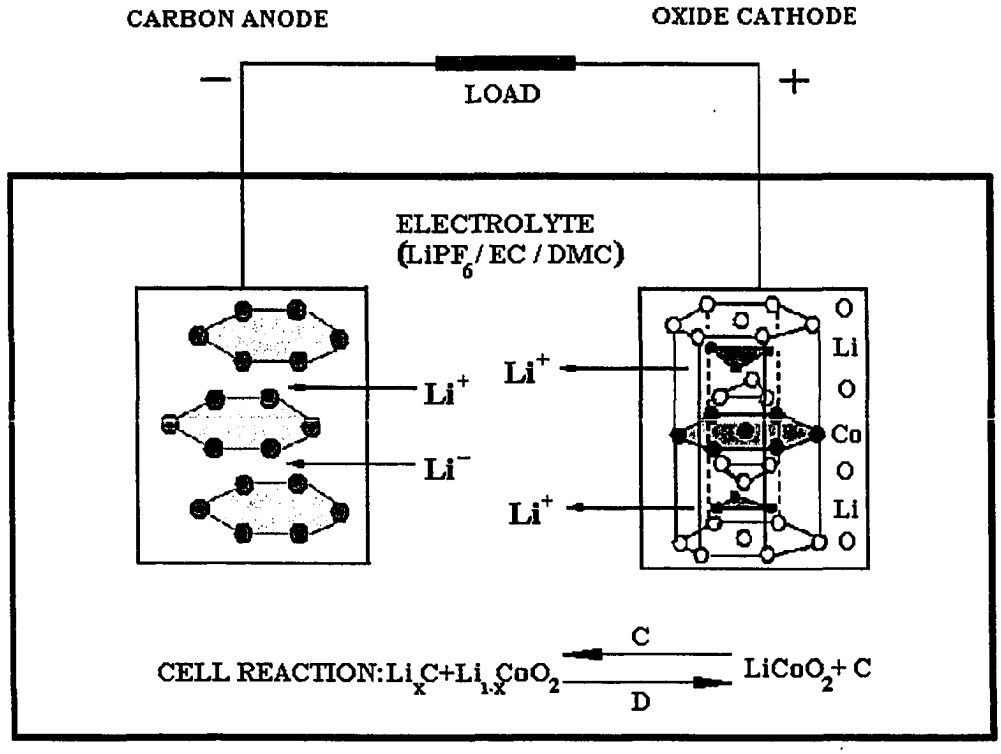

Figure 1-1 The scheme of a lithium ion battery

1.3.1 Anode materials

The anode materials, A^-, are selected to exhibit the following properties: A large lithium capacity, a low voltage with respect to lithium, fast kinetics for lithium charge/discharge reactions, high reversibility, good electronic conductivity, chemical and thermal compatibility with the electrolyte. After a period of intensive research, carbon was found to be the most attractive candidate anode material[4] due to its excellent characteristics in meeting the requirements mentioned above.

There are a wide variety of carbon materials, and these materials can be broadly classified into two types: soft and hard carbons, depending on the processing temperature of the organic precursor (Figure 1-2). Soft carbons can be graphitized by

heat-treatment above 2300°C and hard carbons cannot be graphitized well by heat-treatment even above 2800°C.

The structural variation of carbon materials plays an important part in the voltage profile, reversibility, and the final stoichiometry of the lithium intercalated carbon. Graphite or graphitable carbons, have a nearly perfect layered structure, show well-identified, reversible stages in the intercalation progress with a flat voltage curve near zero volts relative to lithium, corresponding to progressive intercalation of Li^+ within discrete graphene layers to a stoichiometry of LiC_6 with a corresponding theoretical capacity of 372 mAh/g. Petroleum coke, which has a turbostratic structure, shows a steep voltage profile, and intercalates up to x=0.5 in Li_xC_6[5].

In order to develop better carbon anodes, consistent research efforts have been concentrated on the relation between the electrochemical properties and the host structure[6-9]. However, it has been difficult to identify the key structural and morphological parameters of carbon that affect the characteristics of the electrochemical lithium intercalation because carbonaceous materials have a large variation in crystallinity, microtexture and so on. The following table shows the general correlation between the structures of carbon and their lithium intercalation capacities.

The substitution of lithium metal by lithiated carbons inherently leads to sacrifices in capacity, hence, considerable attention is being devoted to increasing the capacity of various disordered carbons. For example, hard carbons appear to have much higher capacities than LiC_6[9,10]. The mechanism of the electrochemical processes, leading to such a high capacity, has not been understood thoroughly as yet. Various models have

been proposed[11], Dahn's model , so called " house of cards " , proposed absorption of lithium on internal surfaces of nanopores formed by monolayer and multilayer graphene sheets in the hard carbon. These hard carbon anodes, however, suffer a very large irreversible capacity and no consistent data are available on their effective operation on prolonged cycling.

Table 1-1 Lithium intercalation capacities of carbonaceous materials.

	Lithium intercalation capacity
Carbon black	20-40 mAh/g
Coke	140-180 mAh/g
Graphite	250-350 mAh/g

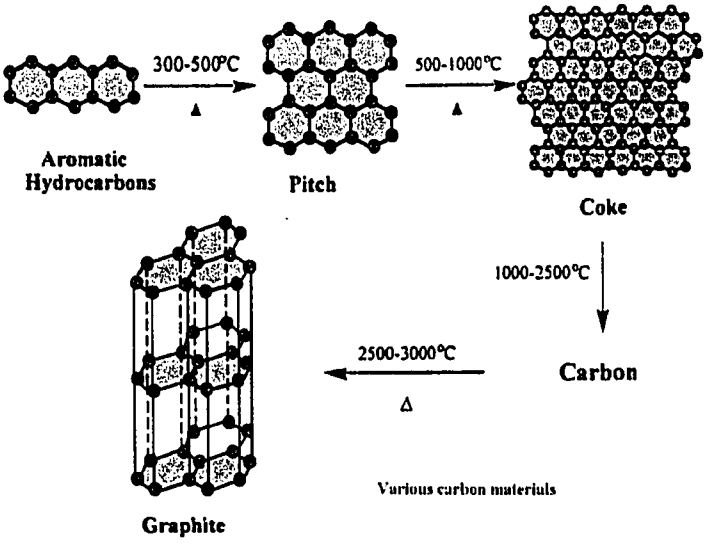

Figure 1-2 Carbon structures depend on the processing temperature.

1.3.2 Cathode materials

The cathode materials, C^+, comprising up to 70% of the total battery mass, largely determine the quality factors, such as specific energy and power, of the battery. Many quality factors must be considered for materials having cathodic function. In lithium ion batteries, the cathode material needs to function as lithium source for the intercalation and deintercalation reactions at the anode. The other requirements for lithium ion cathode materials are: high voltage vs. Li (> 3.0 V) to compensate the voltage losses due to the use of alternate lithium anode materials such as lithium carbon; good reversibility; high lithium ion mobility; minimal changes in the crystal structure due to Li intercalation and deintercalation reactions; good electronic conductivity; chemical and electrochemical stability and non-toxicity. Transition metal oxides are employed as cathode materials.

The most preferred material for Li ion batteries is $LiCoO_2$, shown in Figure 1-3. $LiCoO_2$ has a structure based on rock-salt, but with alternate layers of Li^+ and Co^{3+}. The layered structure allows for relative facile extraction and insertion of lithium ions. $LiCoO_2$ can be prepared easily and has good reversibility with an average capacity of 140 mAh/g. The disadvantages of using $LiCoO_2$ include high cost, low electronic conductivity, and toxicity.

Layered $LiNiO_2$ is another cathode material, the structure also shown in Figure 1-3. Compared to $LiCoO_2$, $LiNiO_2$ has lower cost and higher cyclable capacity of the order of 200 mAh/g. But it is much more difficult to prepare in the electrochemically active form and it suffers capacity fading upon cycling (due to the irreversible structural changes).

The three dimensional $LiMn_2O_4$ spinel is most suited for the lithium intercalation-deintercalation. Spinel structure, named after the parent mineral $MgAl_2O_4$, consists of a face-centered cubic lattice of O^{2-} anions which is held together by interstitial cations. Twice as many cations are distributed in octahedral as tetrahedral sites. If there is only one kind of cations in the octahedral sites, the spinel is called normal. If there are equal amounts of both kinds of cations in the octahedral sites, the spinel is inverse. If there is an unequal number of each kind of cation in the octahedral sites, the spinel is mixed.[80] $LiMn_2O_4$ is the least expensive among the available cathode materials and is non-toxic. The disadvantages are: low specific capacity (limited around 120 mAh/g), which in addition tends to fade upon cycling and storage, especially at high temperature.

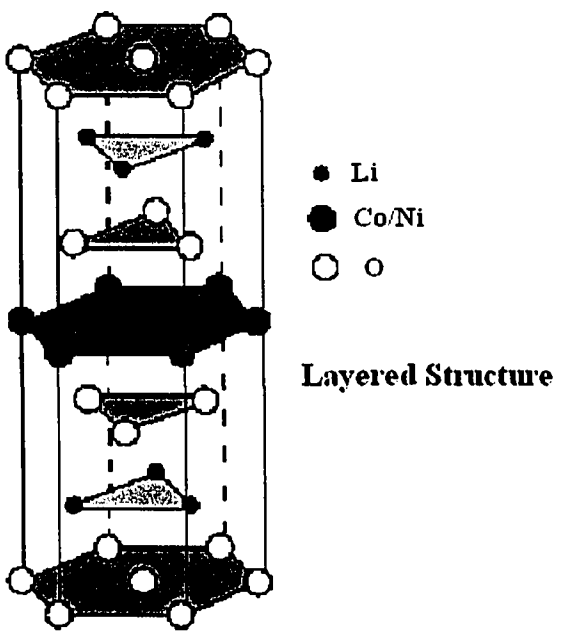

Figure 1-3 The layered rock salt structure.

1.4 Purpose of research

Although lithium ion batteries have been commercially available products for almost one decade, there are still some unsolved questions, which stimulate basic materials research with the aim of further improving their properties. Some goals include the determination of the key parameters that govern the ability of carbonaceous materials to have low potential vs. Li, high capacity and long cycle life; the replacement of carbonaceous materials with alternative low-voltage, Li-accepting anode compounds; the replacement of cobalt with nickel , manganese or other metals in the cathode structure, with the aim of reducing cost, environmental impact or increasing voltage (5 V vs. Li/Li^+).

CHAPTER 2

Methods of Investigation

Understanding the correlation between the structural and electrochemical properties of electrode materials is a key step for improving the performance of lithium ion batteries. Many techniques have made contributions to this research. These techniques include electrochemistry (e.g. cycle voltammetry and charge/discharge capacity determination), transmission electron microscopy (TEM), X-ray diffraction, Extended X-ray absorption fine structure (EXAFS) and nuclear magnetic resonance (NMR) spectroscopy.

Pulsed NMR is an ideal method and powerful tool to explore local structural and electronic environment of Li^+ ions in lithium ion battery electrode materials due to the high NMR sensitivity of the naturally abundant ^7Li nucleus.

2.1 Interactions in solid state NMR

In addition to charge and mass, which all nuclei have, many isotopes possess spin. There is associated with this spin a magnetic moment. The magnetic properties of nuclei were first postulated by Pauli to explain certain hyperfine structural features of atomic spectra. The phenomenon of nuclear magnetic resonance has long been known in molecular beams and has been effectively exploited by the Rabi group at Columbia University[12] to give much useful information concerning nuclear properties. But, the term NMR is commonly reserved for phenomena occurring in bulk matter rather than

in a beam of essentially non-interacting atoms. As a consequence of this convention the first observations of NMR are usually attributed to two groups: Purcell, Torrey and Pound at Harvard and Bloch, Hansen and Packard at Stanford. Their almost simultaneous discoveries are reported in the same volume of the Physical Review published in 1946[13,14].

The basic theories and techniques of NMR can be found in standard texts[15-17] and pulsed experimental methods have been the subject of several books[18,19].

The nuclear spin $\mathbf{I}\hbar$ and magnetic moment μ are related by

$$\mu = \gamma \mathbf{I}\hbar \tag{2.1}$$

where γ is the magnetogyric ratio, a characteristic property of the nucleus. **I** is the spin quantum number. The component of spin in the z-direction will be $\mathbf{I}_z\hbar$ and will take values given by the magnetic quantum number, m, which can have (2I+1) values from $-|\mathbf{I}|$ to $+|\mathbf{I}|$ in integer steps. In the presence of a static applied magnetic field $\mathbf{H_0}$ the magnetic dipoles align to give a series of energy levels, the Zeeman levels (Shown in Figure 2-1), each with energy

$$H_{zeeman} = -\mu \cdot \mathbf{H_0} = -\gamma m\hbar H_0 \tag{2.2}$$

and separated by $\gamma\hbar H_0$. These levels will be populated according to the Boltzmann distribution in the sample at thermal equilibrium. In essence, the NMR experiment consists of detecting transitions between these levels. These transitions can be induced by electromagnetic radiation at the resonant frequency, ω_0, where $\hbar\omega_0 = \hbar\gamma H_0$, ω_0 is also called the Larmor precession frequency. For practical magnets the values of γ define ω_0 in the radio-frequency (r.f.) region of the electromagnetic spectrum.

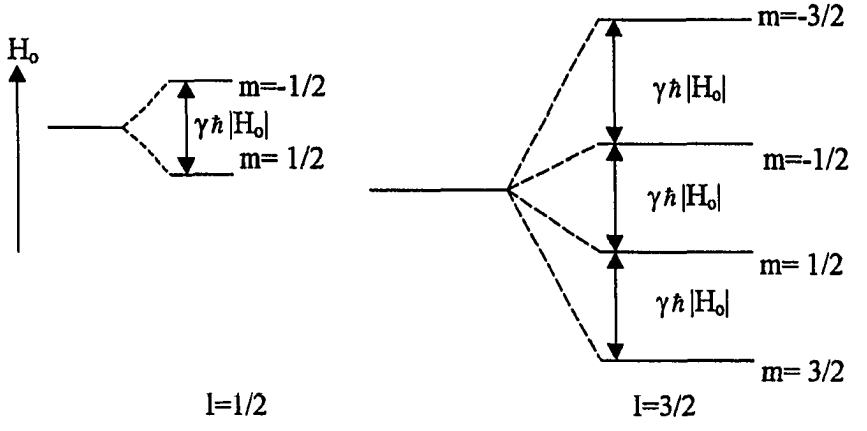

Figure 2-1 Zeeman energy levels for spin 1/2 and spin 3/2.

The Zeeman levels usually are perturbed by interactions of nuclear spins with their local environment. NMR spectra carry information about the local interactions which reveal structural and dynamic information about the material under study. The main terms of interactions for a solid state system are dipole-dipole coupling, electrical quadrupole interaction and chemical-shift.

1) Dipole-dipole interaction

The Hamiltonian describing the interaction between two magnetic moments with distance $\mathbf{r}_{12}$ is[16]:

$$H_D = \frac{\gamma_1\gamma_2\hbar^2}{r_{12}^3}\left\{\mathbf{I}_1\cdot\mathbf{I}_2 - \frac{3(\mathbf{I}_1\cdot\mathbf{r}_{12})(\mathbf{I}_2\cdot\mathbf{r}_{12})}{r^2_{12}}\right\} \qquad (2.3)$$

Rewriting the above Hamiltonian in the spherical coordinate system, shown in Figure 2-2, with $\mathbf{H}_0$ in the Z direction,

$$H_D = \frac{\gamma_1\gamma_2\hbar^2}{r_{12}^3}(A + B + C + D + E + F) \qquad (2.4)$$

Where

$$A = I_{1z}I_{2z}(1-3\cos^2\theta)$$

$$B = -\frac{1}{4}(I_1^+I_2^- + I_1^-I_2^+)(1-3\cos^2\theta)$$

$$C = -\frac{3}{2}(I_{1z}I_2^+ + I_1^+I_{2z})\sin\theta\cos\theta e^{-i\phi}$$

$$D = -\frac{3}{2}(I_{1z}I_2^- + I_1^-I_{2z})\sin\theta\cos\theta e^{+i\phi}$$

$$E = -\frac{3}{4}I_1^+I_2^+\sin^2\theta e^{-i2\phi}$$

$$F = -\frac{3}{4}I_1^-I_2^-\sin^2\theta e^{-i2\phi}$$

The terms A and B are diagonal, they shift the Zeeman level by a small amount. While the other four terms C-F only have off-diagonal elements and hence they make second-order contribution to the energy and can usually be ignored. The remaining dipolar term A+B may be combined to give the following

$$H_d^0 = \frac{1}{2}\frac{\gamma^2\hbar^2}{r^3}(1-3\cos^2\theta)(3I_{1z}I_{2z} - \mathbf{I}_1\cdot\mathbf{I}_2)$$

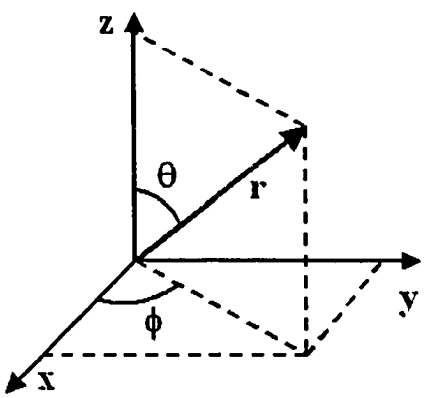

Figure 2-2 Relationship between rectangular coordinates x,y,z and the polar coordinates r, θ, ϕ.

2) Nuclear electric quadrupole interaction

Nuclei with spins of 1/2 possess a spherical distribution of the nuclear charge and are therefore not affected by electric environment. Nuclei with spins of 1 or greater, however, are found to have electric quadrupole moments. The interaction between the electric quadrupole moment of a nucleus and the electric field gradient (EFG) produced by surrounding electrons is called the quadrupole interaction.

In the principal axis system of the electric field gradient tensor, shown in Figure 2-3, the Hamiltonian of the electric quadrupole interaction can be written[15] as

$$H_Q = \frac{e^2qQ}{4I(2I-1)}\left\{3I_z^2 - I(I+1) + \frac{1}{2}\eta(I_+^2 + I_-^2)\right\} \qquad (2.5)$$

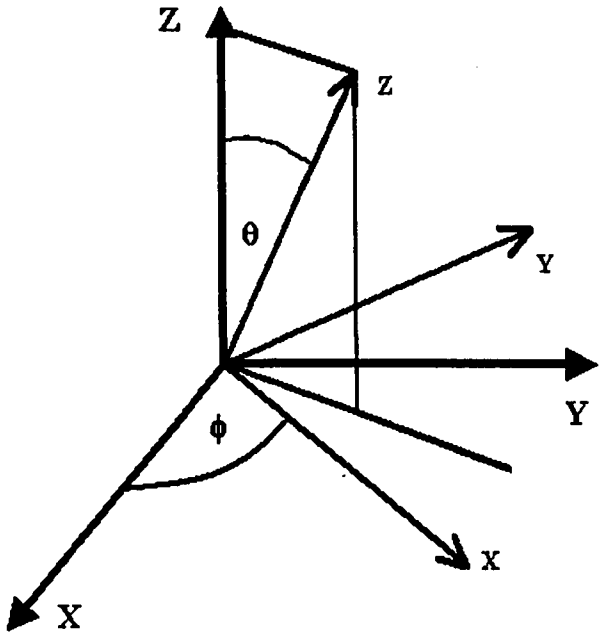

Figure 2-3 The orientation of the principal-axis frame of EFG(x,y,z) relative to laboratory frame(X,Y,Z). The V_{zz} component of EFG tensor is along the z-axis.

With the definitions, eq = V_{zz} and $\eta = \frac{V_{xx} - V_{yy}}{V_{zz}}$. It is the convention to define the components of the traceless tensor $|V_{zz}| \geq |V_{yy}| \geq |V_{xx}|$. The value q alone has no physical meaning in SI units. eQ is the electric quadrupole moment. The quadrupole coupling constant, C_{qcc}, is commonly defined as:

$$C_{qcc} = \frac{e^2 qQ}{\hbar} \tag{2.6}$$

C_{qcc} is a measure of how strong the interaction between the quadrupole moment and the EFG is. The quadrupole frequency is defined as:

$$\omega_Q = \frac{3e^2 qQ}{2I(2I-1)\hbar} \tag{2.7}$$

In laboratory frame (X,Y,Z) , the first-order quadrupole interaction is

$$H_Q^{(0)} = \frac{\hbar\omega_Q}{6}\left\{\frac{3\cos^2\theta - 1}{2} + \frac{\eta}{2}\sin^2\theta\cos 2\phi\right\}\left(3I_z^2 - I(I+1)\right) \tag{2.8}$$

In a stationary EFG, the quadrupole interaction shifts the Zeeman levels according to the square of the quantum nmuber m to a first approximation.Thus, for nuclear ^{7}Li with spin I = 3/2, m can be 3/2, 1/2, -1/2, or -3/2, and the m = ±3/2 levels shift identically while the m = ±1/2 levels shift identically as shown in Figure 2-4.

The first order perturbation energy shift , in frequency units, is

$$\omega_{m,m-1}^{(1)} - \omega_L = -\frac{\omega_Q}{4}\left[\left(3\cos^2\theta - 1\right) + \eta\sin^2\theta\cos 2\phi\right](2m-1) \tag{2.9}$$

Observing the above expression, the central transition, corresponding to m=-1/2→m=+1/2, has no shift in the first order quadrupole interaction. The transitions on either side of the central one are called satellite lines and are equally separateed.

For an axially symmetric EFG case, η=0, the quadrupole splitting Δ is

$$\Delta = \frac{1}{2}\omega_Q\left(3\cos^2\theta - 1\right) \tag{2.10}$$

The second order quadrupole shift for the central transition is

$$\omega^{(2)}_{-1/2,1/2} - \omega_L = -\frac{\omega_Q^2}{6\omega_L}\left\{I(I+1) - \tfrac{3}{4}\right\}\left\{A(\phi,\eta)\cos^4\theta + B(\phi,\eta)\cos^2\theta + C(\phi,\eta)\right\} \tag{2.11}$$

where

$$A = -\tfrac{27}{8} - \tfrac{9}{4}\eta\cos 2\phi - \tfrac{3}{8}\eta^2\cos^2 2\phi$$

$$B = +\tfrac{15}{4} - \tfrac{1}{2}\eta^2 + 2\eta\cos 2\phi + \tfrac{3}{4}\eta^2\cos^2 2\phi$$

$$C = -\tfrac{3}{8} + \tfrac{1}{3}\eta^2 + \tfrac{1}{4}\eta\cos 2\phi - \tfrac{3}{8}\eta^2\cos^2 2\phi$$

The random distribution of orientations in a polycrystalline or powder sample gives rise to a continuous distribution of frequencies.The resulting line-shape is termed a powder pattern, an example is given in Figure 2-4.

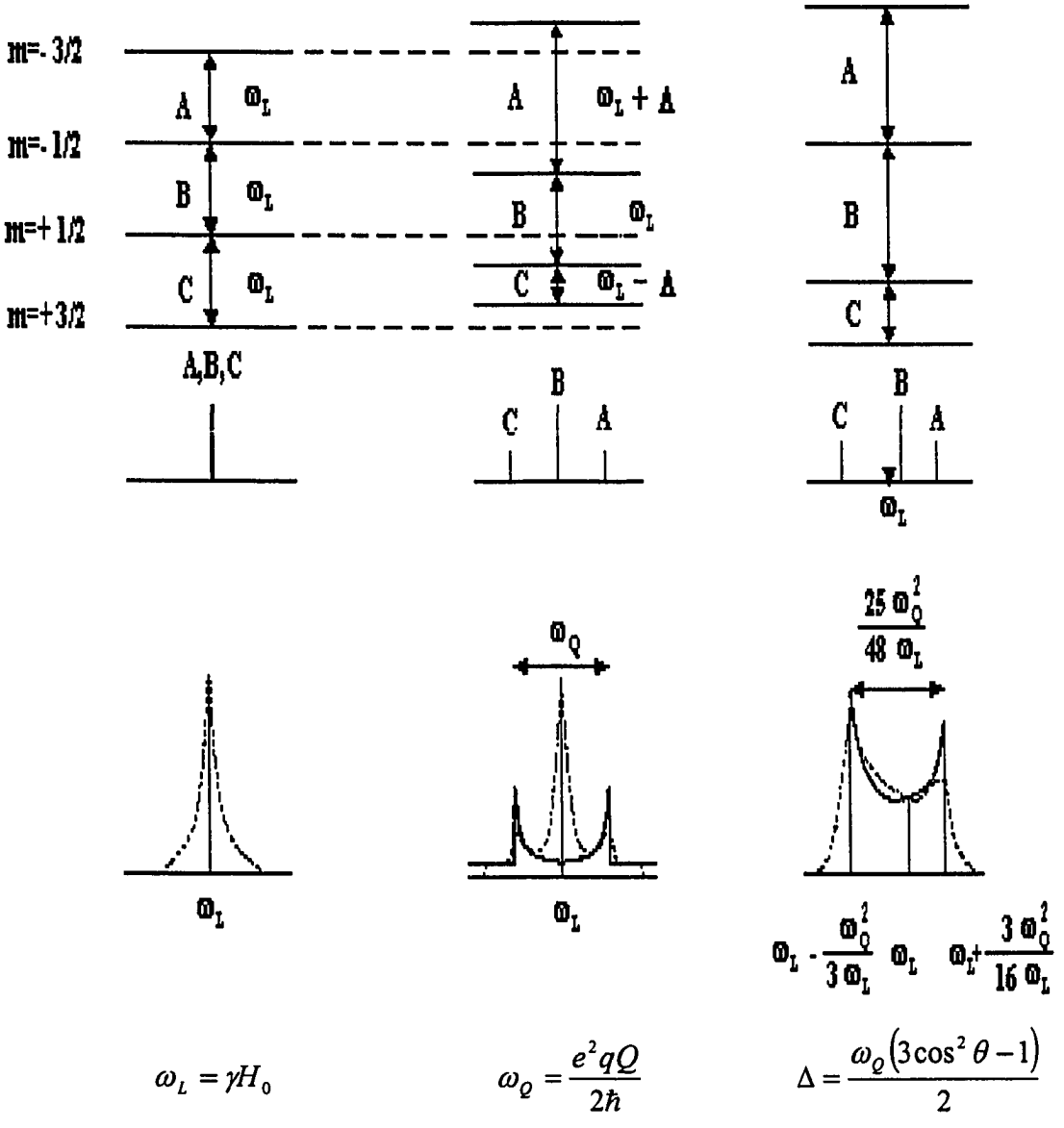

Figure 2-4 Quadrupole splitting of the magnetic resonance of a nucleus of spin 3/2. Left: no quadrupole interaction. Center: first order splitting of satellite. Right: second order shifting of the central component.
Top: energy spectrum. Middle:spectrum of a single nucleus without dipole broadening.
Bottom: spectrum of a powered sample with axially symmetric field gradient. With the dipolar broadening superimposed, the dotted curves result.

3) Interactions with electrons

The characteristic resonance frequency of a nucleus depends to a very small, but measurable, extent upon its chemical environment. The origin of this variation in the resonance frequency is the cloud of electrons about each of the nuclei. For a diamagnetic substance in an external magnetic field, orbital currents are induced in the electron cloud and these give rise to small, local magnetic fields, which are always proportional to $\mathbf{H}_0$ but opposite in direction (it is assumed that all the electrons are paired off, so that there is no net magnetic moment in the sample; if there are unpaired electrons, there will be a magnetic field arising from the unpaired electron along the direction of $\mathbf{H}_0$). This is called chemical shift effect. The Hamiltonian of chemical shift can be written as

$$H_{CS} = \gamma\hbar\mathbf{I}\cdot\sigma\cdot\mathbf{H}_0 \qquad (2.12)$$

Where σ is the chemical shift tensor. In the principle axis coordinate system of chemical shift tensor, the first order shift in Zeeman frequency is[83] :

$$\Delta\nu_{CS} = -\nu_{Zeeman}\left[\sigma_{iso} + \sigma_{aniso}\left(3\cos^2\theta - 1\right) + \sigma_{axial}\sin^2\theta\cos 2\phi\right] \qquad (2.13)$$

Where

$$\sigma_{iso} = \tfrac{1}{3}(\sigma_1 + \sigma_2 + \sigma_3)$$

$$\sigma_{aniso} = \tfrac{1}{6}(2\sigma_3 - \sigma_1 - \sigma_2)$$

$$\sigma_{axial} = \tfrac{1}{2}(\sigma_2 - \sigma_1)$$

where $\sigma_1, \sigma_2, \sigma_3$ are the principal components of the chemical shift tensor σ and $\sigma_1 \leq \sigma_2 \leq \sigma_3$.

Paramagnetic substances are characterrized by the presence of unpaired electron spins which arise from d or f electrons in unfilled shells of atoms or ions. Due to the strong interaction between the unpaired electron spin and the nuclear spin, NMR spectra of these materials usually are characterized by large shifts and line broadening.[81] The NMR spectral shift arising from interaction with the unpaired spin is a sum of two terms: contact and dipolar (sometimes called pseudocontact). The Fermi contact interaction is the interaction between the nuclear spin and a net electron spin density at the nucleus. When the electron spin relaxation time is sufficiently short, the shift due to contact interaction can be written as

$$\left(\frac{\Delta H}{H_0}\right)_{con} = -\left(\frac{g_e\mu_B}{g_N\mu_N}\right)\frac{a_N S(S+1)}{3kT} \tag{2.14}$$

where ΔH is the shift of nuclear resonance signal, H_0 is the external static field, a_N is the electron hyperfine interaction constant at the nucleus N, $\frac{S(S+1)}{3kT}$ is the mean value of the electron spin component along the applied magnetic field H_0. The dipolar shift arises from the direct magnetic interaction of the electron spin and the nuclear spin. An example of dipolar shift for tetragonal symmetry is[82]

$$\left(\frac{\Delta H}{H_0}\right)_{dip} = -(3\cos^2\theta - 1)r^{-3}\mu_B^2\frac{S(S+1)}{3kT}F(g) \tag{2.15}$$

where r is the separation between the nucleus N and the unpaired electrons, and θ is the angle between the vector **r** and the symmetry axis of the molecule. $F(g)$ is a function depending on the g tensor components which reduced to $(g_{\parallel}^2 - g_{\perp}^2)/3$ for axial symmetry.

A distinctive effect, called the Knight shift , produced by the conduction electron spin in nuclear resonance spectra is due to the very strong local magnetic fields, which result from the so-called contact interaction. The quantitive theoretical expression for the shift can be written as[31]:

$$\frac{\Delta H}{H_0} = \frac{8\pi}{3} \left\langle |U_k(0)|^2 \right\rangle_{E_F} \chi_e^s \qquad (2.16)$$

$\left\langle |U_k(0)|^2 \right\rangle_{E_F}$ gives the density of electrons near the Fermi level. χ_e^s is the magnetic susceptibility. As an example, the metallic Li has a Knight shift of 265 ppm[32].

2.2 Pulse NMR techniques

Most of the modern NMR measurements are performed in a pulsed experiment, i.e. the sample is subjected to short pulses of high-intensity r.f. power and the resulting time dependence of the magnetization is observed along particular directions (usually in the plane perpendicular to the external static magnetic field $\mathbf{H_0}$). The pulses can be varied in terms of carrier frequency, tip angle with respect to $\mathbf{H_0}$, phase and length, and often the experiments involve a complex sequence of pulses. The effect of these pulses can be considered in a classical terms as the motion of precessing magnets of moment μ in magnetic field $\mathbf{H_0}$. On this basis a single magnet will precess around $\mathbf{H_0}$ with a frequency ω_0 describing a cone at angle φ. The assembly of magnets in a sample can be regarded as spread evenly over this cone to give a net, small magnetization along the $\mathbf{H_0}$ direction, **M**, but no magnetization perpendicular to this direction. Pulses of r.f. power can be used to tip the precessional cone and change the

direction of the magnetization. (in rotating frame of reference)The tip angle θ of **M** is given by

$$\theta = \gamma H_1 t_p \qquad (2.17)$$

where H_1 is the r.f. magnetic field($|\mathbf{H}_1| << |\mathbf{H}_0|$), t_p is the duration of H_1.

A basic pulsed experiment is to apply an intense r.f. pulse at resonance to tip the magnetization **M** 90° from the $\mathbf{H}_0$ direction. This gives rise to a decaying and oscillating magnetization, $\mathbf{M}_{xy}$, in the xy-plane, which can be observed as an induced voltage in a detector coil. $\mathbf{M}_{xy}$ will decay with time as the nuclei dephase due to spin-spin interaction and inhomogeneity of the field $\mathbf{H}_0$ (Figure 2-5).The decaying signal in the detector coil, proportional to $\mathbf{M}_{xy}(t)$, is known as the Free Induction Decay (FID) and the spectral lineshape is its Fourier Transform.(Figure 2-6)

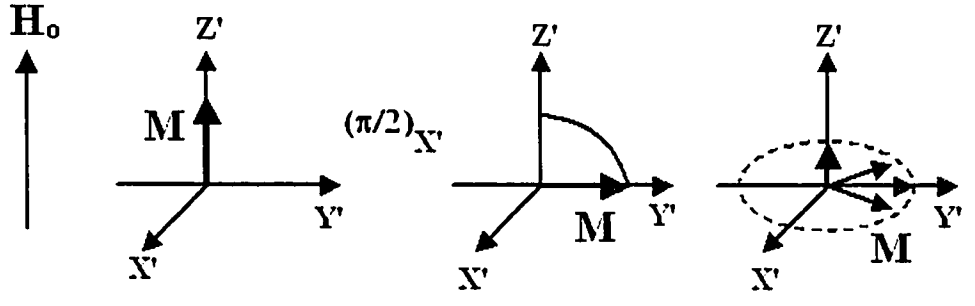

Figure 2-5 Effect of R.F. pulse on magnetization M

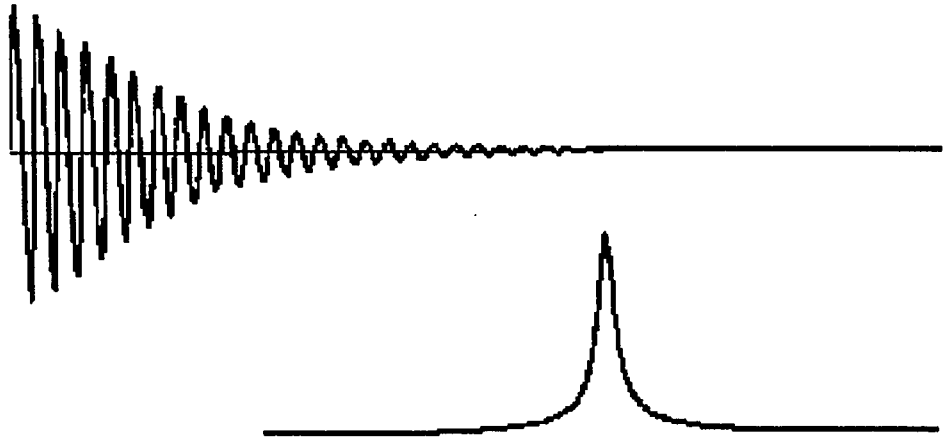

Figure 2-6 A FID (top) and corresponding spectrum (botton).

The time constant for this decay is termed the transverse relaxation time, T_2^*, and is approximately to $1/\Delta\omega$. $\Delta\omega$ is the full width at half magnitude or the linewidth for the NMR spectrum. Spin-echo sequence[20] can be used to measure spin-spin relaxation time T_2 directly. T_2 is defined as an intrinsic relaxation time which is characteristic of the magnetization decay without any field inhomogeneity effects. Figure 2-7 shows the effect on magnetization by an ordinary or Hahn echo sequence $\left(\frac{\pi}{2}\right)_{x'} - \tau - (\pi)_{y'} - \tau$. Hahn echoes in this sense cannot be formed in dipolar coupled solids where the local field is not static. It is possible to form echoes in solids by using the sequence $\left(\frac{\pi}{2}\right)_{x'} - \tau - \left(\frac{\pi}{2}\right)_{y'} - \tau$. This is the solid echo and under the condition $\tau << T_2$, the trailing half of the echo is equal to the FID. Therefore, another important application of spin-echo technique is overcoming the "dead time" problem[21] in pulsed NMR, especially when measuring the rapid decaying signals of solid state samples.

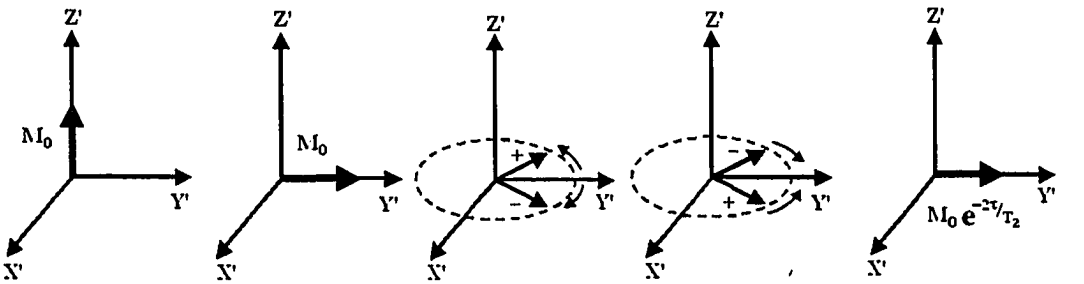

Figure 2-7 Classical picture of spin echo

After a sufficiently long time following a 90° pulse the spin system will return to the equilibrium. The characteristic relaxation time for this process is termed the longitudinal or spin-lattice relaxation time, T_1. For this relaxation to occur the spins must exchange energy with their environment, the 'lattice'.

One basic method to measure T_1 is inversion-recovery (Figure 2-8). The initial 180° pulse is used to tip the magnetization so that $\mathbf{M_z(t=0) = -M_0}$. After time τ some of the $\mathbf{M_z}$ will have returned, as given by the expression

$$\mathbf{M_z(\tau) = M_z(0)[1-2e^{-\tau/T1}]} \qquad (2.18)$$

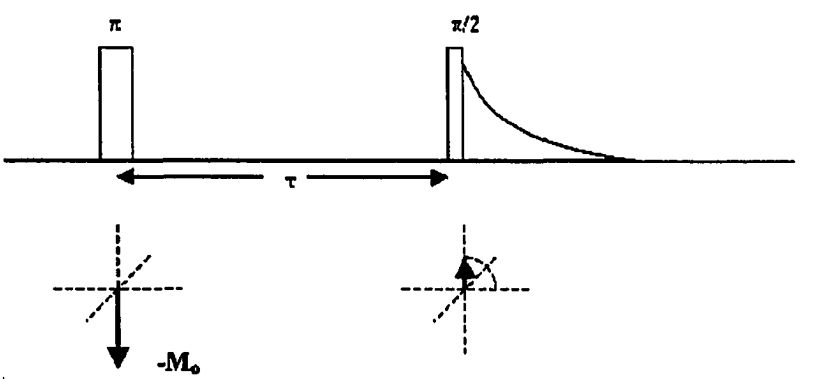

Figure 2-8 Measure T1 using Inversion-recovery method

The second 90° pulse is applied to generate a FID and the amplitude of the FID after this pulse is proportional to $\mathbf{M_z(\tau)}$. Thus, T_1 can be determined by varying τ and fitting to equation (2.18).

"Magic Angle Spinning" technique is often used to improve the resolution of NMR signal. In the interactions between the nucleus and its environment, dipole-dipole coupling, chemical shift effect and the first order nuclear electrical quadrupole interaction all have an angular dependence of Legendre polynomial of second kind $P_2(\cos\theta) = \frac{1}{2}(3\cos^2\theta - 1)$, where θ is the angle between the magnetic field and an intrinsic axis of the crystal, depending on the interaction involved. Rotating the sample makes the average intrinsic axis the same as the rotation axis, shown in Figure 2-9. When the rotation axis is chosen to be at the magic angle θ = 54.74°, all interactions of the form $(3\cos^2\theta - 1)$ will vanish. This technique has been used successfully to reduce the dipolar interaction, chemical shift anisotropy and first order quadrupole interaction that lead to substantial line-broadening of the NMR resonances in solid materials. [22,84-88]

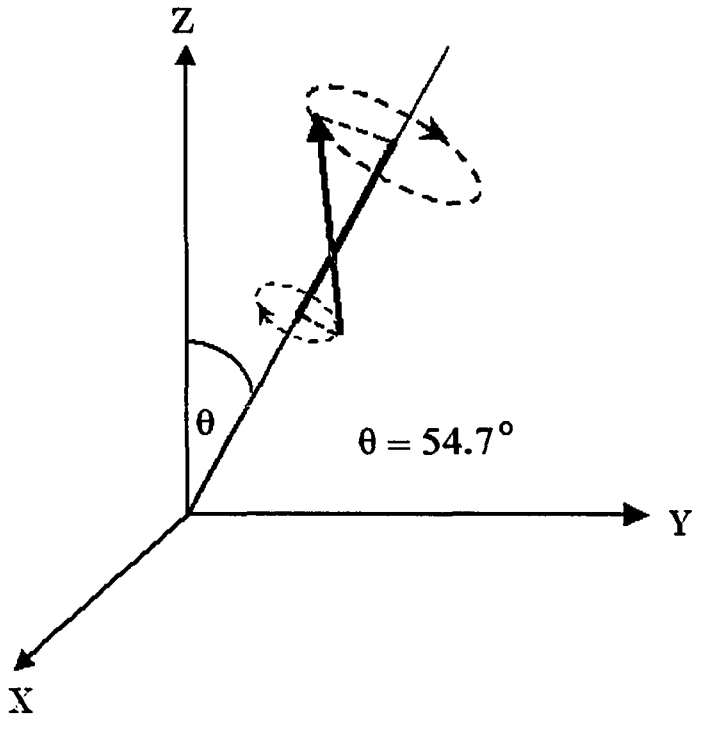

Figure 2-9 Rapid spin of the sample makes the effect intrinsic axis along the rotation axis.

2.3 NMR equipment

NMR experiments were performed with Chemagnetics CMX-300 spectrometer.

1) Two separate R.F. channels with separate high power amplifiers.

   H-channel: output of high frequency power amplifier is up to 1 KW ; frequency range is 282 –310 MHz.

   X-channel: output of low frequency power amplifier is up to 1.5 KW ; frequency range is 10-125 MHz.

2) Magnet : field strength is 7 Tesla (superconducting magnet). Homogeneity of H_0 is determined by the linewidth for a liquid D_2O sample, which is about 0.095 ppm for 5 mm coil and 0.15 ppm for 10 mm coil .
3) The temperature controller: temperature range is $-150^{\circ}C$ to $250^{\circ}C$ with accuracy $\pm 0.2^{\circ}C$.
4) MAS speed controller: monitors and controls the rotors with maximum spinning rate of 7 KHz.
5) Probes: The Chemagnetics commercial probes are employed in experiments.

Figure 2-10 shows the schematic diagram of CMX-300 system.

Figure 2-10 CMX-300 NMR facility

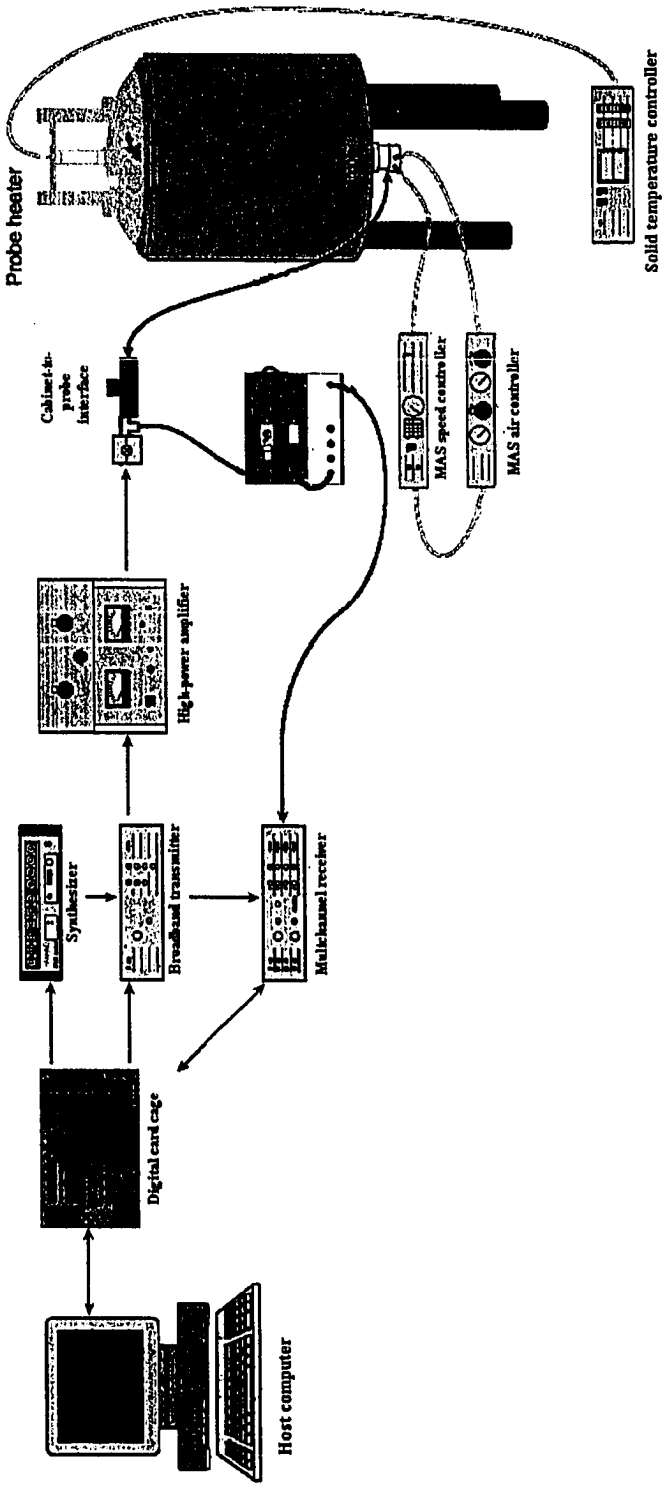

CHAPTER 3

^{7}Li nuclear magnetic resonance study of lithium insertion in pristine and partially oxidized graphite

(Collaboration with V.Yufit and E.Peled, School of Chemistry, Tel Aviv University, Ramat Aviv, 69978 Israel, where materials were prepared and characterized.)

3.1 Introduction

The lithiated graphite anode, as a safe alternative to lithium metal, is a major factor in the commercial success of lithium ion batteries. The primary insertion mechanism of alkali metals into graphite is topotactic intercalation, which is a highly reversible reaction.[23] The fact that this reaction can be induced electrochemically is the reason for its importance to battery technology. ^{7}Li NMR has been shown to be a useful tool to investigate the local structural and electronic environment of intercalated Li ions. Since the first reported NMR study of lithium-intercalated graphite in 1977,[24] many papers on the subject have appeared[25-28]. The most important aspect of ^{7}Li NMR in this context is its sensitivity to the electronic environment of the Li^+ ions. In particular, the stage 1 compound LiC_6 is metallic, which yields a relatively large Knight shift of the ^{7}Li resonance. Higher-stage compounds give different Knight shifts than that of stage 1. In addition, electrochemical decomposition of the electrolyte results in formation of a solid electrolyte interphase (SEI) on the surface of the carbon grains. The SEI consists of both inorganic (i.e. salts) and organic Li compounds that usually

can be distinguished spectroscopically from intercalated Li. Moreover, NMR is a quantitative method by which the relative fractions of Li with different spectroscopic signatures can be determined in a straightforward manner.

Previous work by our group has shown that mild oxidation of graphite can improve its performance as a lithium ion battery anode material by increasing its reversible lithium capacity, decreasing its irreversible capacity and by facilitating the formation of a chemically bonded SEI.[29,30]

3.2 Experiments

Natural (NG7-Kansai Coke) and partially oxidized graphite were electrochemically lithiated against lithium counter electrode with different values of x (as in Li_xC_6 corresponding to the nomenclature for Li-intercalated graphite) obtained during the first or the second deintercalation step. NMR measurements were performed with a Chemagnetics CMX-300 spectrometer operating at a ^{7}Li-resonance frequency of 117 MHz. Both wide-line and high resolution (MAS) ^{7}Li spectra were obtained. The MAS spinning rates were between 5 and 6 kHz. R.F. pulse widths corresponding to a 90°C flip angle were about 4μs. Aqueous LiCl solution was employed as a chemical shift reference. Spin-lattice relaxation time (T_1) were measured by inversion recovery.

3.3 Results

The samples studied are listed in Table 3-1 and Table 3-2, including their calculated electrochemically reversible lithium contents. A typical charge-discharge

curve (for sample Y26, Table 3.2) of the samples being studied is depicted in Figure 3-1.

Wide-line ^{7}Li NMR spectra of lithiated pristine graphite, Li_xC_6, with x ranging from 0.18 to 0.60, are displayed in Figure 3-2. The relatively small amount of irreversible Li contained in the SEI is not included in the x-value. At low Li-content(up to x = 0.22) there is a single spectral component corresponding to a typical spin-3/2 power pattern; i.e. a central transition and two satellite transitions. From the latter separation, quadrupole coupling constant (QCC) of about 37 kHz can be deduced. The peak of the central transition occurs at around 3 ppm. Close examination of the spectrum reveals a slight asymmetry about the central transition peak, which is attributed to Li residing in the SEI at around zero ppm. The spectra for x = 0.51, 0.57 and 0.60 are similar to each other in appearance, but are dramatically different than those of the x~0.2 spectra. The higher Li content samples exhibit two distinct Li sites, the dominant one with a central transition peak at 43 ppm and QCC of 33 kHz, and a smaller component with a central transition peak of 11 ppm and QCC of 39 kHz. The spectral parameters are summarized in Table 3-3. The 11 ppm feature exhibits its maximum intensity at x = 0.51 and decrease with further increased lithiation.

Table 3-1: Lithiated pristine graphite

Sample	State	Li_xC
Y17 pristine	Cycle 2, Charge	X = 0.18
Y19 pristine	Cycle 2, Charge	X = 0.19-0.22
Y20 pristine	Cycle 2, Charge	X = 0.19-0.22
Y27 pristine	Cycle 2, Charge	X = 0.57
Y28 pristine	Cycle 2, Charge	X = 0.51
Y29 pristine	Cycle 2, Charge	X = 0.6
Y30 pristine	Cycle 2, Charge	X = 0.6

Table 3-2: Lithiated oxidized graphite

Sample	State	Li_xC
Y13 Oxidized 8%	Cycle 1, Charge	X = 0.42
Y14 Oxidized 8%	Cycle 1, Charge	X = 0.57
Y15 Oxidized 8%	Cycle 1, Charge	X = 0.18
Y16 Oxidized 8%	Cycle 1, Charge	X = 0.20
Y23 Oxidized 8%	Cycle 2, Charge	X = 0.47
Y24 Oxidized 8%	Cycle 2, Charge	X > 0.7
Y25 Oxidized 8%	Cycle 2, Charge	X = 0.17
Y26 Oxidized 8%	Cycle 2, Charge	X = 0.17

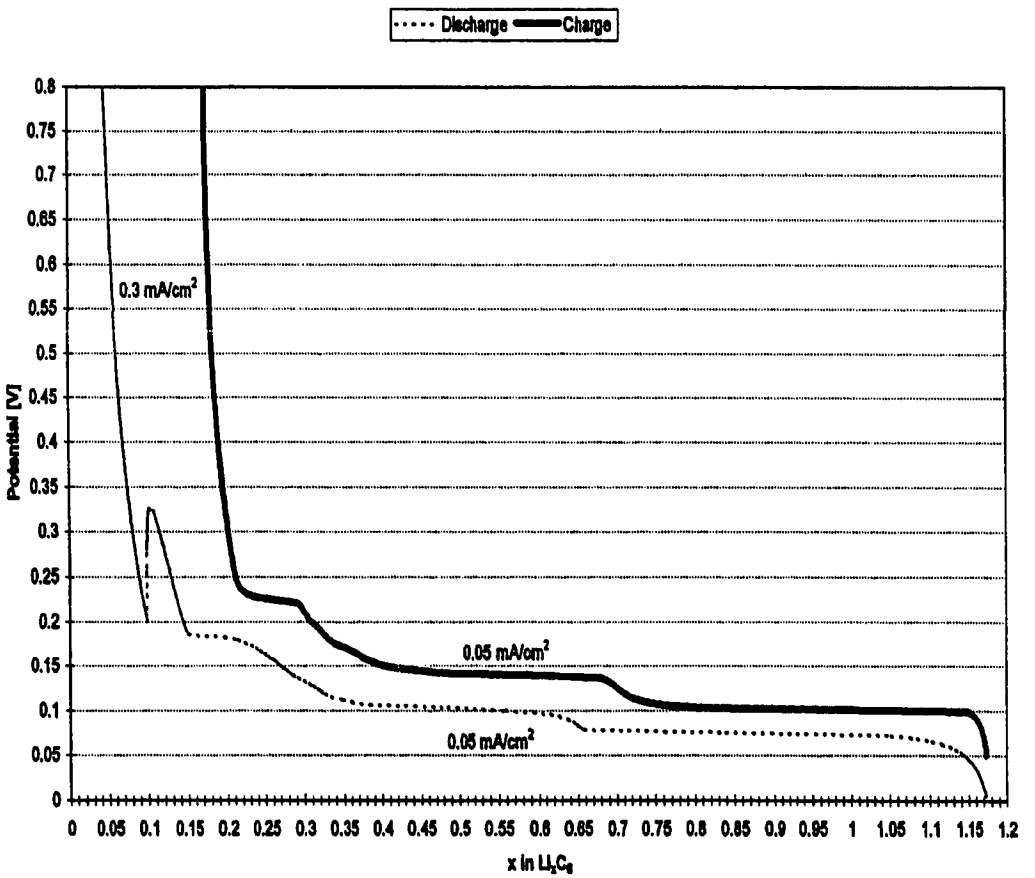

Figure 3-1 Charge and discharge curves as a function of composition x in Li_xC.

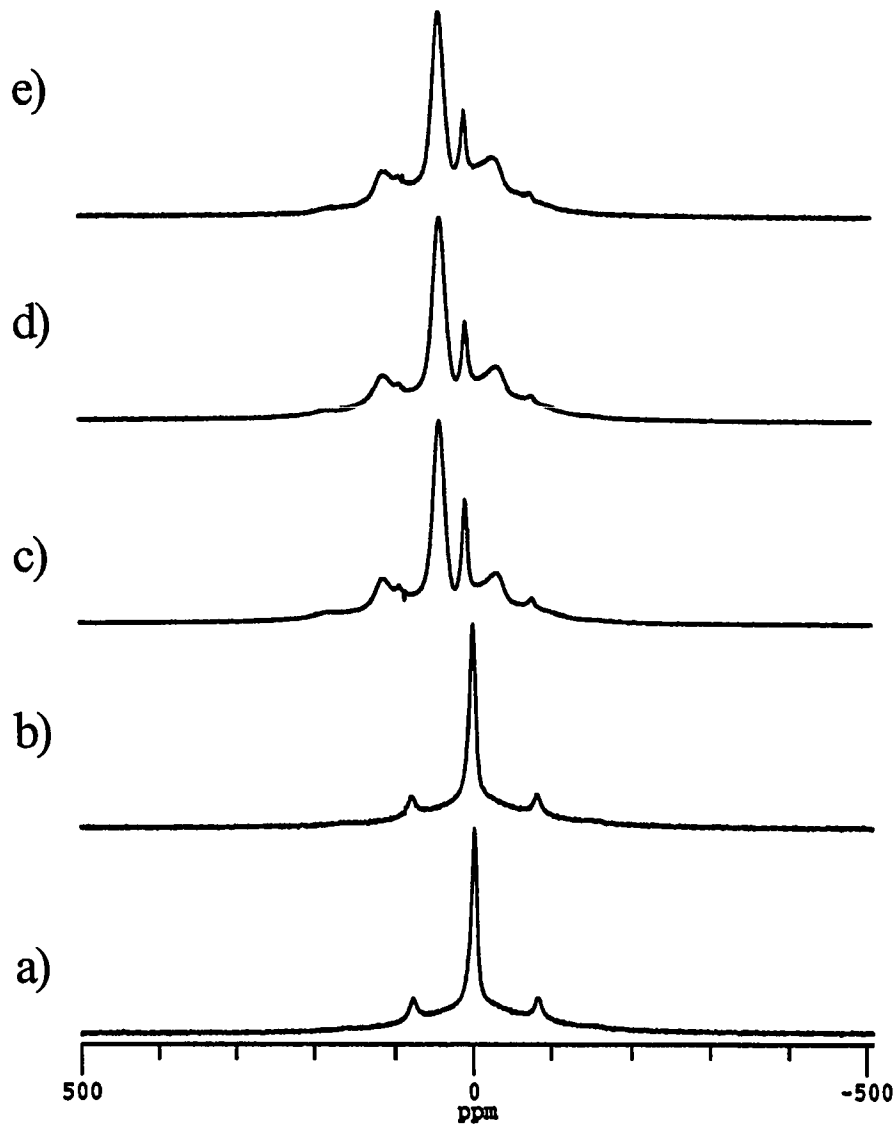

Figure 3-2 Wide-line ^{7}Li NMR spectra of lithiated natural graphite. Sample designations are from Table 1. a) x = 0.18 (Y17); b) x = 0.19-0.22 (Y19); c) x = 0.51 (Y28); d) x = 0.57 (Y27); e) x = 0.60 (Y30).

Table 3-3 NMR chemical shifts and quadrupole coupling constants of lithiated pristine graphite.

Pristine Graphite	Li_xC X	Peak1			Peak2			Peak3		
		Wide (ppm)	Spin (ppm)	e^2qQ/h (kHz)	Wide (ppm)	Spin (ppm)	e^2qQ/h (kHz)	Wide (ppm)	Spin (ppm)	e^2qQ/h (kHz)
Y17	0.18	2.5	3.8	36.8						
	0.19-0.22	1.8	2.4	36.8						
Y20	0.19-0.22	1.1	2.7							
Y27	0.57		1.7		10.9	10.9	39.0	43.2	41.1	32.6
Y28	0.51		1.0		11.3	11.0	39.0	44.0	41.2	33.0
Y29	0.60		2.7		10.9	10.2	39.0	43.9	41.5	32.8
Y30	0.60		1.1		11.0	10.6	39.0	43.6	41.2	32.8

High-resolution MAS measurements were performed to assist in site assignment and analysis of their relative populations. For x~0.2, the two bottom spectra in Figure 3-3, only a single site is resolvable at 3 ppm, however with some asymmetry due to a small component at zero ppm from the SEI lithium. At higher Li content, it is possible to observe three sites, the SEI component at zero ppm, the 11 ppm component and the 43 ppm component. Although the SEI is not directly observable in the low Li content samples because of overlap with the 3 ppm signal, it can be resolved at low temperature by utilizing an inversion recovery pulse sequence in concert with MAS, as shown in Figure 3-4. At −130°C, the difference in T_1 between the SEI Li and the

3 ppm feature, the latter with a longer T_1 than the former, results in selective inversion of the latter.

Wide-line ^{7}Li NMR spectra of oxidized graphite (8% burn-off) are displayed in Figure 3-5. As in the case of pristine graphite, the lithiated oxidized graphite exhibits a single site for x~0.2, with a central transition peak of 3 ppm and QCC of about 36 kHz. At higher lithiation, there are two dominant peaks, one at 13 ppm with QCC of 39 kHz, and one at 41-43 ppm with QCC of 33 kHz. This is again, similar to the parameters noted for pristine graphite except that the intensity of the 13 ppm peak in oxidized graphite is considerable larger than that of the 11 ppm feature on the graphite. Several spectra of lithiated oxidized graphite, with 9.5% burn-off, are displayed in Figure 3-6. The spectral parameters corresponding to Figure 3-5 and 3-6 are summarized in Table 3.4. High-resolution MAS ^{7}Li spectra corresponding to the wide-line ones in Figure 3-5 and 3-6 are shown in Figure 3-7 and 3-8, respectively. From both Figure 3-6 and 3-8 (spectra of 9.5% burn-off graphite), the SEI content is about the same as the 8% burn-off material. This indicates that the formation of SEI is not strongly influenced by modest changes in the burn-off treatment. On the other hand, upon comparing SEI intensities with pristine graphite with a similar charging history, it is clear that the oxidized samples exhibit a larger SEI component. This observation was reported in a previous study, which was attributed to a chemically-bonded SEI formed by electrochemical reaction with the partially oxidized graphite surface[30]. However, it was found that the irreversible capacity is larger for the pristine samples. Combining this finding with the intensity data for peak 1 (3 ppm) leads to the conclusion that the SEI on the oxidized samples is richer in inorganic

compounds like LiF or carbonates (and poorer in polymers) or that the formation process of the SEI is more efficient and requires less capacity.

In an attempt to shed additional light on the nature of 11(13) ppm peak in pristine (oxidized) graphite, wide-line NMR spectra of a deliberately air–exposed sample (x = 0.42 in 8% burn-off material) were obtained and displayed in Figure 3-9. It is clear that with increased air exposure, the 13 ppm (with QCC of 39 kHz) component increases in intensity. This suggests that this feature is a surface rather than intercalated site. A similar observation was made for 11 ppm (39 kHz QCC) site in air-exposed lithiated pristine graphite.

3.4 Discussion

Carefully analysis of the ^{7}Li chemical shift (CS) presented in Table 3-3 and 3-4 reveal slight differences between the first and the second intercalation- deintercalation cycles and perhaps between the pristine and oxidized samples.

1) The average CS for peak 1 of pristine samples (Y19 and Y20, Table 3-3) after the first cycle is 2.6±0.2 ppm; the one measures after the second cycle (Y27-Y30, Table 3-3) is lower, only 1.6±0.6 ppm.
2) Similar changes were found for peaks 1,2 and 3 of the oxidized samples. The average CS values for peaks 1,2 and 3 after the first cycle are 3.6±0.5, 13.3±0.0 and 43.2±0.4, respectively (Y13-Y16, Table 3-4), the ones measured sfter the second cycle are lower, 1.8±0.2,11.5±0.6 and 42.1±0.1 ppm respectively(Y23-Y26, Table 3-4).

The changes in the CS are attributed to graphite structural changes taking place in the first few cycles.

In order to formulate a coherent model of the mechanism of electrochemical lithium insertion in graphite, it is necessary to determine quantitatively the various site occupancies in addition to identifying the distinct Li sites. The results of this analysis are listed in Table 3-5, corresponding to MAS spectra. Spectral intensities of the various species are reported in Table 3-5 as a percentage of the total ^{7}Li NMR intensity of that particular sample. Wide-line spectra were also analyzed for consistency, and the modest disagreements in intensity distributions between the wide-line and MAS data are attributed to spectral overlap for the wide-line case, and incomplete accounting of spinning side-band intensities for the MAS case. In the case of strong spectral overlap between the SEI component near 0 and the 3 ppm feature, no attempt was made to resolve their relative intensities, except for having shown that they can be distinguished by selective inversion (Figure 3-4). The 3 ppm (and 36kHz QCC) signal appears at low levels of lithiation, and has been previously attributed to a high stage intercalation phase, such as LiC_{18}[30]. At higher Li content this phase is difficult to distinguish from the SEI and its corresponding quadrupole satellite transitions are unobservable. This is consistent with the conversion of high stage to low stage intercalated graphite as the lithium content increases. After detailed comparison of the peak intensity data in Table 3-5 with charge-discharge results, we conclude that the 3 ppm peak is assigned to stage 4 intercalated graphite, i.e. to LiC_{24} and not to stage 3.

The 11 ppm feature is absent in pristine graphite at low lithiation (x~0.2). Because of the unavailability of samples with $0.22<x<0.47$, it is impossible to tell precisely where (at what Li content) the onset of the 11 ppm feature occurs. However, it is clear that this site decreases in intensity with increasing lithiation. This is also observed in the case of oxidized graphite (note, in particular the very small 13 ppm component for the $x>0.7$ sample in Figure 3-6 and 3-8). On the other hand, close examination of oxidized graphite at low lithiation (x~0.2) reveals a very small component at around 10-11 ppm which we believe is the same (or similar) site as that which gives rise to the 13 ppm feature at higher lithiation. On the basis of the increased intensity of this feature in oxidized compared to pristine graphite and its strong increase upon modest air exposure, we assign this spectral component to a surface-bonded, or edge site, rather than an interior or intercalated one. Zaghib and coworkers have assigned a similar 11 ppm (with 39 kHz QCC) site to a higher stage (stage 3) intercalated phase, and this would certainly account for its decrease with increasing lithiation, as has been stated above for the 3 ppm feature. However, as it did not disappear in samples with x=0.5-0.6 and for the reasons cited above, having to do with factors that are expected to be more surface than bulk sensitive, we do not think that it relates to a higher stage. We believe that the 11(13) ppm feature in pristine (oxidized) graphite is mainly associated with metastable edge site that is electrochemically reversible. On the basis of charge-discharge behavior, due to the fact that the unlithiated graphite has (mostly) a ABAB packing, atomic-size voids exists between adjacent microphases (at the B edges). It is plausible that lithium atoms can reside at these sites. During the lithiation process (at higher x values) the graphite stacking changes to AAA and these edge

sites are lost and the edge lithium ions move into the graphite galleries. The oxidized graphite has additional edge sites inside the nanosize voids created by the oxidization. The lithium at these sites may or may not move to the gallery at the end of the intercalation. Although the mechanism is unclear at the present time, lithium ions occupying this edge site seems to become intercalated into the structure at higher lithiation. The 43 ppm peak is assigned to both stage 2 (LiC_{12}) and stage 1 (LiC_6) intercalated graphite, both species having been shown to have very similar electronic environments and hence similar Knight shift.[24-28]

3.5 Conclusions

Electrochemically lithiated natural graphite in this study exhibits three reversible Li species, stages-1 and 2 intercalation compound (LiC_6 and LiC_{12}) manifested by an average ^{7}Li Knight shift of 43 ppm, a 3 ppm feature assigned to high stage compound and Li (located at 11 to 13 ppm) bonded to edge sites, the edge site occupancy is enhanced by partial oxidation of the graphite (up to 9.5% mass burn-off), and increasing lithiation results in host structural rearrangement which converts the edge-site Li into stage 1 intercalated Li.

Table 3-4 NMR chemical shifts and quadrupole coupling constants of lithiated oxidized graphite.

Oxidized Graphite	Li_xC X	Peak1			Peak2			Peak3		
		Wide (ppm)	Spin (ppm)	e^2qQ/h (kHz)	Wide (ppm)	Spin (ppm)	e^2qQ/h (kHz)	Wide (ppm)	Spin (ppm)	e^2qQ/h (kHz)
Y13 8%	0.42		3.7		10.5	13.3	39	43.2	43.5	33.2
Y14 8%	0.57		2.5		9.7	13.3	39	41.3	42.8	33.2
Y15 8%	0.18	1.4	3.8	36.4						
Y16 8%	0.20	2.7	4.2	36.4						
Y23 9.5%	0.47		1.8		10.2	12	39.4	43.2	42.2	33.0
Y24 9.5%	>0.7		1.6		11.0	11.4		42.5	42.0	33.6
Y25 9.5%	0.17	0.4	2.1	35.8		10.4				
Y26 9.5%	0.17	0.4	1.7	36		12.3				

Table 3-5 Relative spectral intensities based on MAS data

Graphite	$Li_xC(x=)$	NMR intensity of peak 1<3 ppm(%)	NMR intensity of peak2<13 ppm(%)	NMR intensity of peak 3<43 ppm(%)
Y14(O)	0.57	14	24	62
Y23(O)	0.47	19	22	59
Y24(O)	>0.7	12	2	86
Y25(O)	0.17	66	34	0
Y26(O)	0.17	76	24	0
Y27(P)	0.57	15	14	70
Y28(P)	0.51	9	23	68
Y29(P)	0.6	17	29	54
Y30(P)	0.6	18	12	70

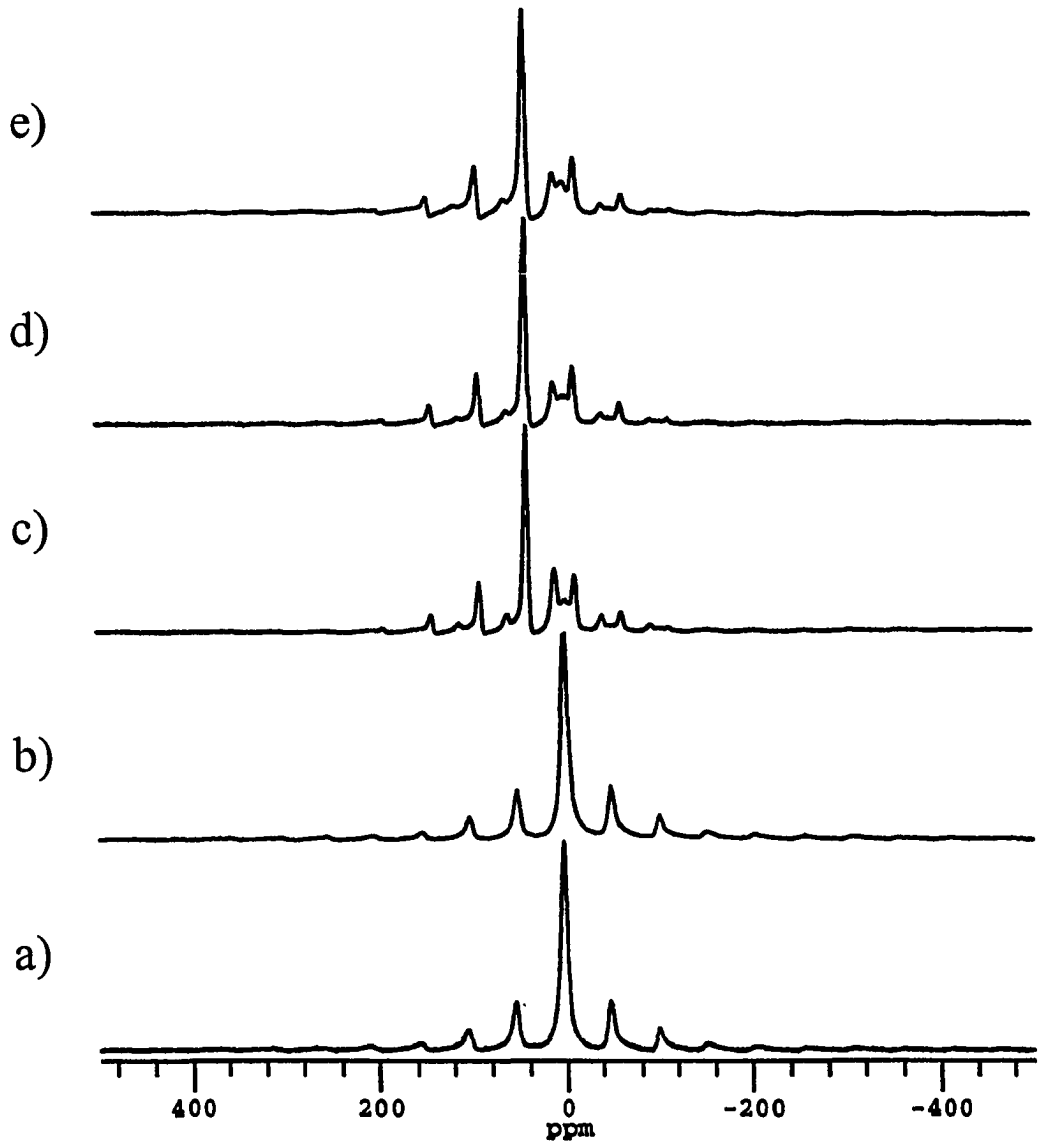

Figure 3-3 High resolution ^{7}Li NMR spectra of lithiated natural graphite. Sample designations are from Table 1. a) x=0.18(Y17); b) x=0.19-0.22(Y19); c) x=0.51(Y28); d) x=0.57(Y27);e) x=0.60(Y30).

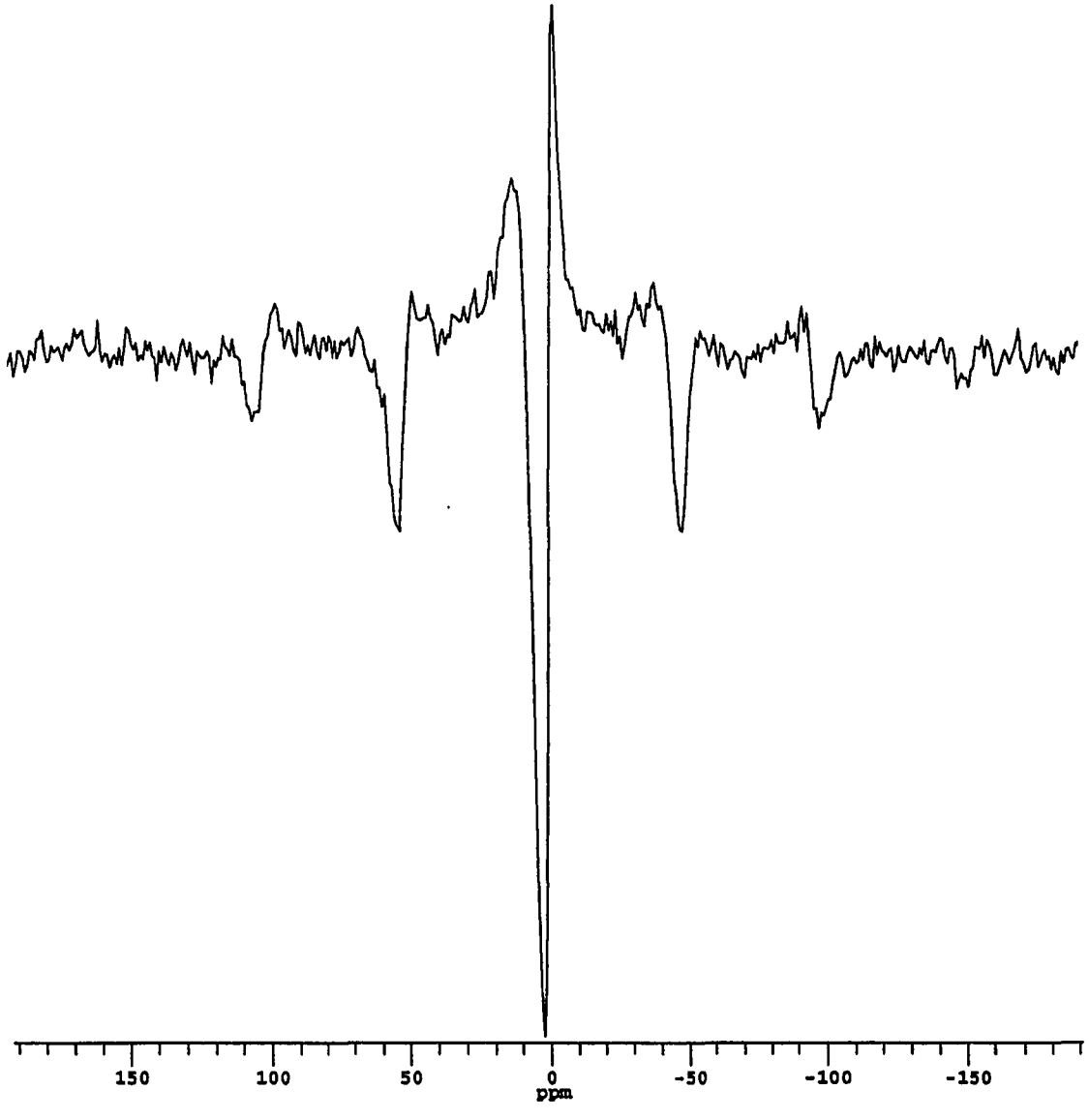

Figure 3-4 Partially inverted ^{7}Li NMR spectrum of lithiated natural graphite at $-130^{\circ}C$, illustrating different spin-lattice relaxation of 3 ppm feature and SEI.

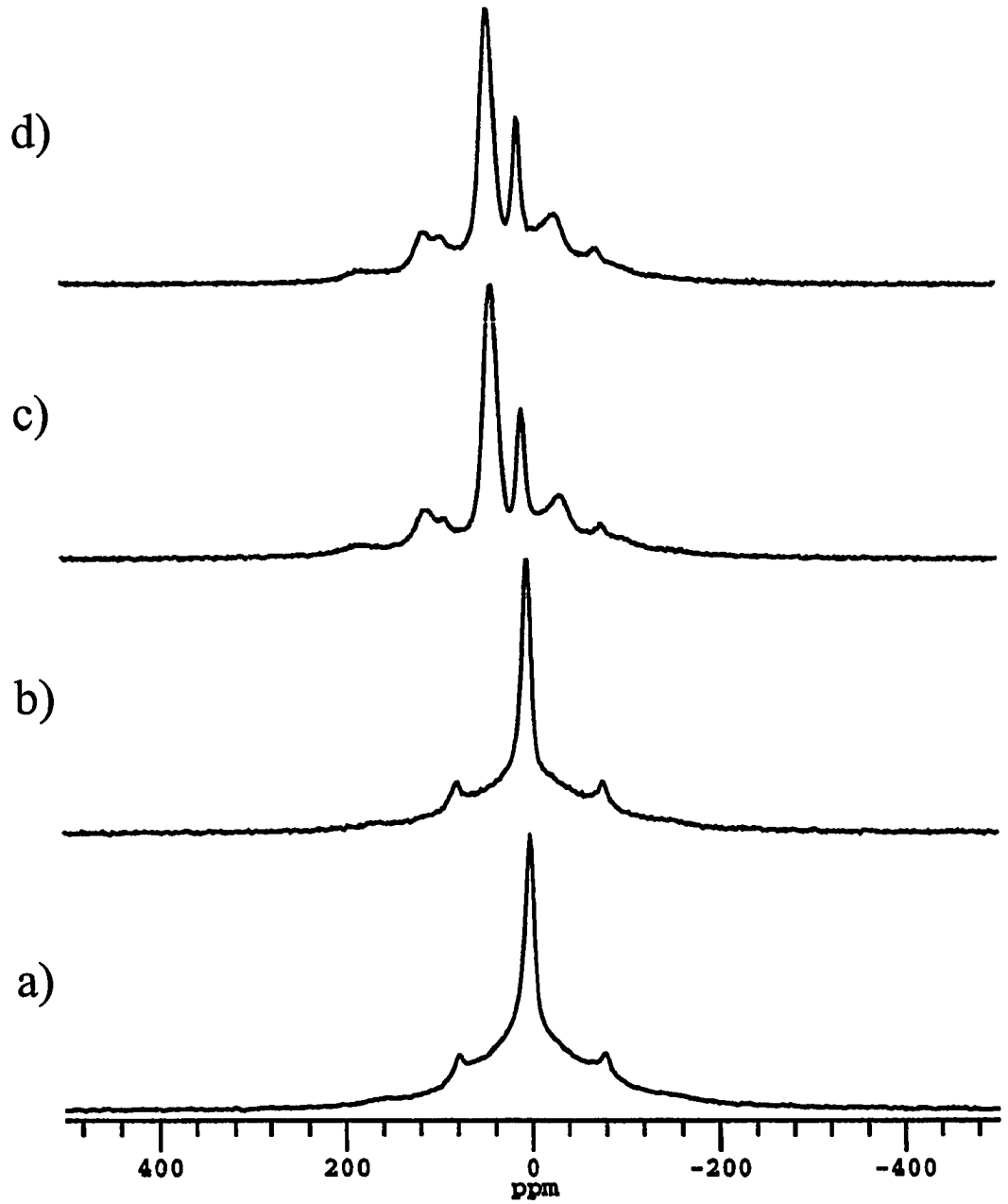

Figure 3-5 Wide-line ^{7}Li NMR spectra of lithiated, partially oxidized (8% burn-off) natural graphite. Sample designations are from Table 2. a) x =0.18 (Y15); b) x = 0.20 (Y16); c) x = 0.42 (Y13); d) x = 0.57 (Y14).

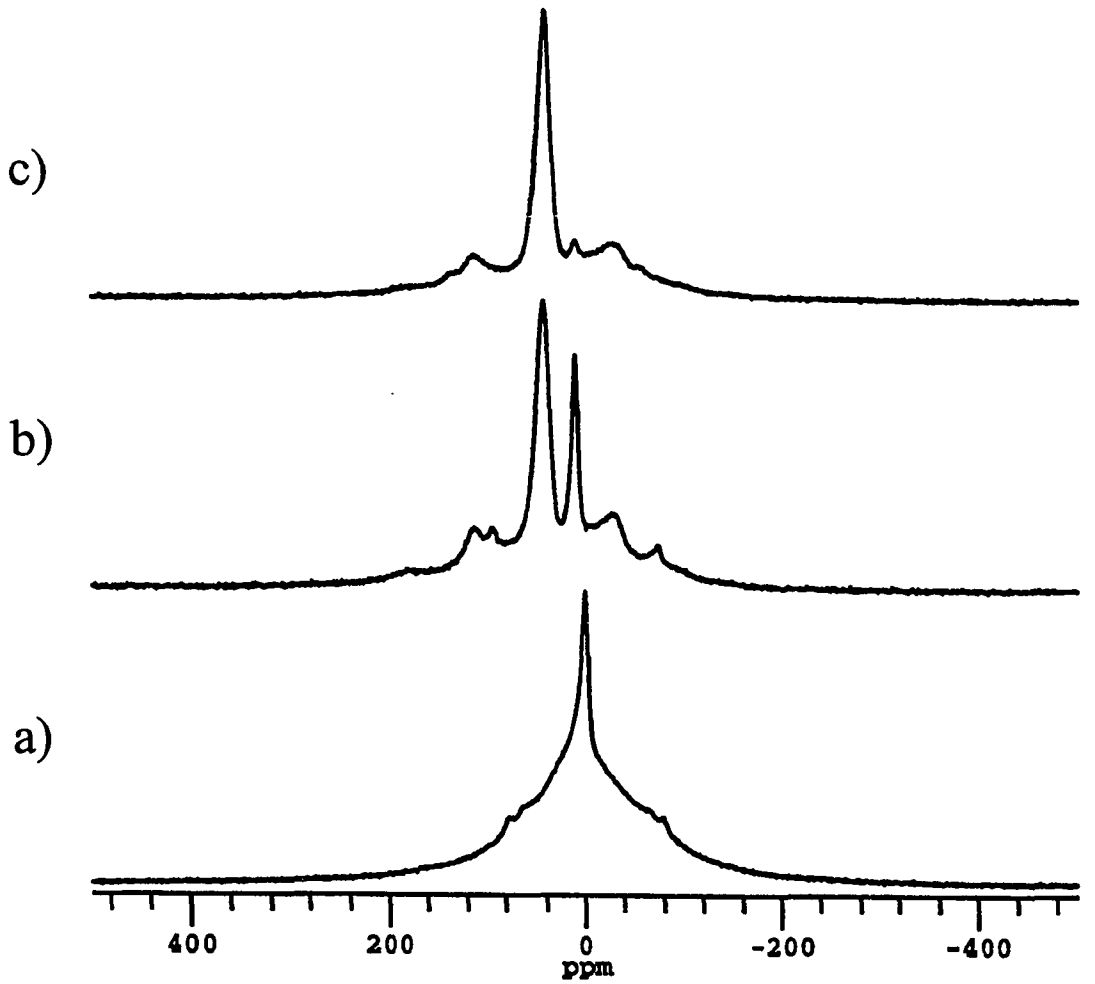

Figure 3-6 Wide-line ^{7}Li NMR spectra of lithiated, partially oxidized (9.5% burn-off) natural graphite. Sample designations are from Table 2. a) x =0.17 (Y25); b) x = 0.47 (Y23); c) x >0.7 (Y24).

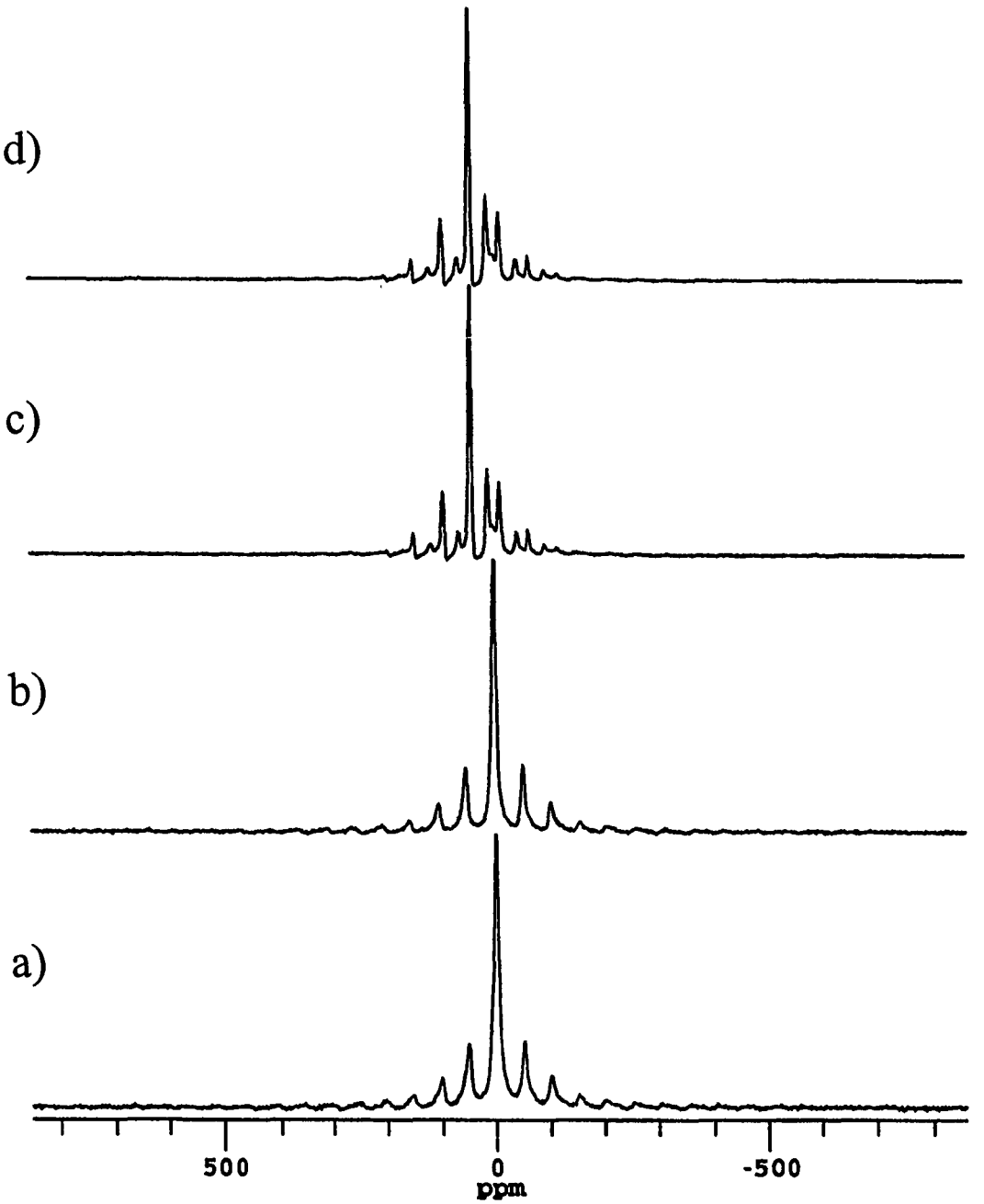

Figure 3-7 High resolution MAS ^{7}Li NMR spectra of lithiated, partially oxidized (8% burn-off) natural graphite. Sample designations are from Table 2. a) x =0.18 (Y15); b) x = 0.20(Y16); c) x = 0.42 (Y13); d) x = 0.57 (Y14).

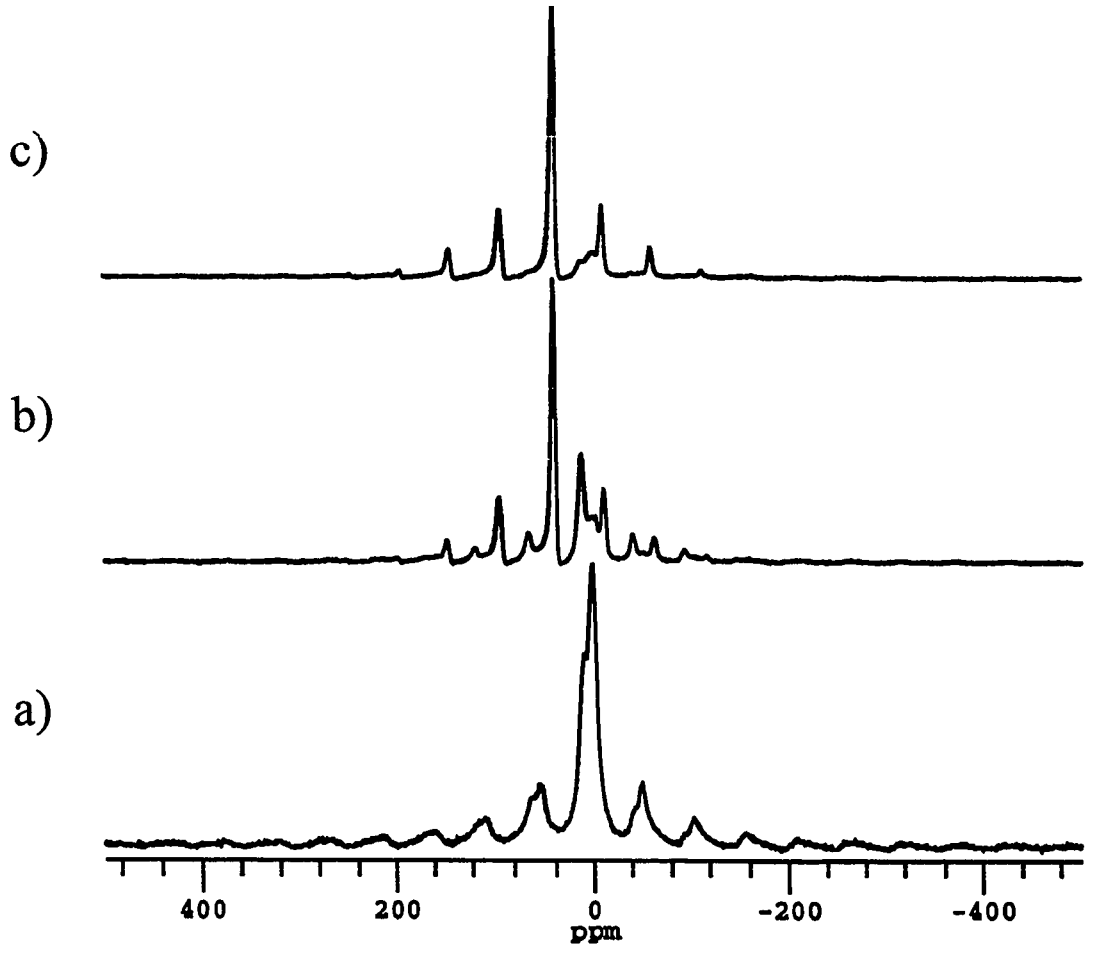

Figure 3-8 High resolution MAS ^{7}Li NMR spectra of lithiated, partially oxidized (9.5% burn-off) natural graphite. Sample designations are from Table 2. a) x =0.17 (Y25); b) x = 0.47 (Y23); c) x >0.7 (Y24).

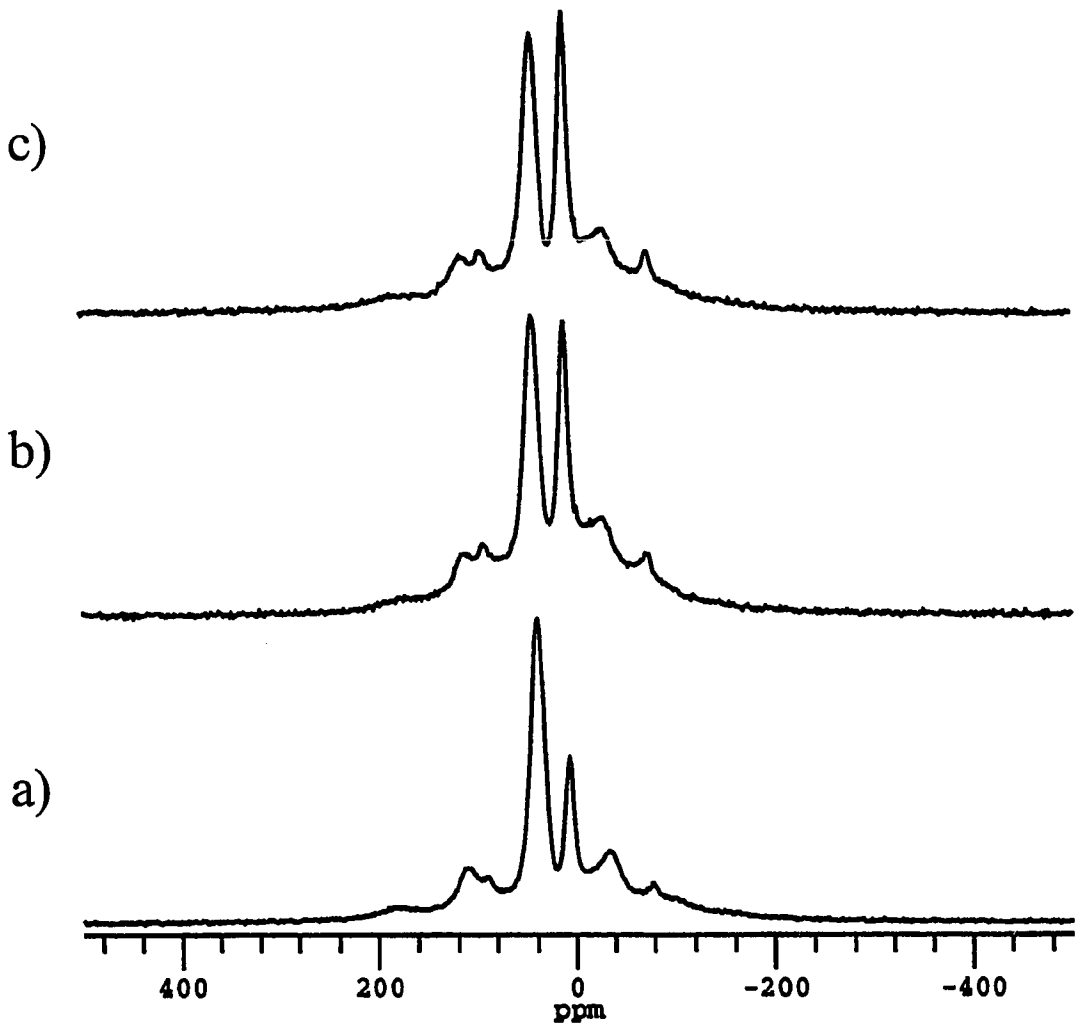

Figure 3-9 Wide-line ^{7}Li NMR spectra of lithiated (x = 0.42), partially oxidized (8% burn-off) natural graphite. a) before exposed to air; b) 2 hours after exposed to air; c) 48 hours after exposed to air.

CHAPTER 4

Solid Electrolyte Interphase Formation on Lithium-Ion Electrodes: A ^{7}Li Nuclear Magnetic Resonance Study

(Collaboration with Jun Liu and Khalil Amine, Argonne National Laboratory, Division of Chemical Technologies, Argonne, Illinois 60439, USA; materials prepared at Argonne National Laboratory)

4.1 Introduction

Lithium-ion batteries show great promise in meeting or exceeding the high-power goals established for hybrid electric vehicle (HEV) energy storage devices by the Partnership for a New Generation of Vehicles (PNGV).[33] However, one of the major barriers for this technology is short calendar life. The best lithium –ion cell technologies have a 3-5 year calendar life, which falls short of the 10 year PNGV life goal.

Area specific impedance measurements, conducted at Argonne National Laboratory, of cells aged at 60% state-of-charge at 50 and 70°C for 8 and 2 weeks, respectively , showed that the cell impedance increased by somewhat more than a factor of two after aging. Furthermore, microreference electrode study confirmed that the increase in the interfacial resistance at the positive electrode is the main cause of the power fade in high power lithium-ion batteries.[34] An important factor governing both performance and calendar life in lithium-ion batteries concerns the formation of

the SEI on the electrode particles during initial and subsequent charging of the cell[35] as described in the previous chapter. There are several reports in the literature on identification of chemical species in the SEI by X-ray photoelectron spectroscopy and other methods,[36,37] although most of this effort has been confined to the graphitic anode. Lithium-7 NMR has been shown to be a useful tool for characterizing SEI formation in graphite[28,38] as described in the previous chapter even though it lacks the chemical specificity to distinguish between SEI components, that is, the SEI usually yields a featureless NMR line centered at a frequency characteristic of ionic Li in solution.[38] However, because NMR is quantitative, it is relatively straightforward to determine the relative fraction of Li residing in the SEI, compared to reversible (intercalated) Li.

To date there have been few reports of SEI formation on the cathode, but evidence from ac impedance studies cited above suggests that passivating films are being formed on the cathode as a function of cycling and accelerated aging conditions[34]. Furthermore, high-resolution transmission electron microscopy measurements carried out on particles isolated from aged positive electrode reveal the formation of an amorphous film at the grain boundaries of the particles.[39] As this film is electrically insulating (as suggested by the impedance results) its growth will eventually lead to loss of electrical contact between cathode particles, resulting in cell failure. In this chapter, solid state ^{7}Li NMR measurements of SEI formation on both graphite anodes and, for the first time to the best of our knowledge, the cathode, the latter based on $LiNi_{0.8}Co_{0.2}O_2$.

4.2 Experimental

High-power 18650(18mm diam, 65 mm cylindrical) cells, employing multitab current collection, were fabricated by Polystor corporation and were used for accelerated calendar life testing at different state of charge and temperatures. The cells incorporated a $LiNi_{0.8}Co_{0.2}O_2$ positive electrode, a blend of MCMB-6 and SFG-6 graphite negative electrode, and a 1 M $LiPF_6$ ethylene carbonate: diethyl carbonate (1:1) electrolyte in a Celgard 2500 separator. Both anode and cathode contained 8% by weight poly (vinylidene difluoride) (PVDF) binder, and to the cathode was also added 4% by weight each of SFG-6 graphite and acetylene black. After initial performance characterization, cells were subjected to elevated temperature calendar life testing at 60% state-of-charge (SOC), for 8 weeks at 50°C and 2 weeks at 70°C. The calendar life test was carried out by potentiostating the cell at a fixed SOC. The cell was then stored in an oven at the desired temperature. After each 2 week storage, the area specific impedance of the cell was measured to check if the cell still met the power requirement set by PNGV. The cells were discharged prior to disassembly for NMR analysis.

For the NMR measurements, one set of materials was rinsed in dimethyl carbonate to remove residual electrolyte salt and dried. The electrodes were scraped off the current collectors and ground into a powder. Although the rinse process is regarded as a necessary step to eliminating potentially strong background NMR signals from the salt, there is a question of whether this procedure also dissolves some of the SEI being studied. For this reason, a second set of materials was simply dried without rinsing for

comparison with the first set. All procedures were performed in an Ar glove box. About 300 mg of sample powder was packed into 5 mm o.d. Pyrex tubes and sealed under dry N_2. Wide line NMR spectra were acquired at a ^{7}Li-resonance frequency of 117 MHz on a Chemagnetics CMX300 spectrometer. Aqueous LiCl solution was used as a chemical shift reference (0 ppm). For broad lines typical of transition metal-based cathodes, quadrupole echo sequence ($\left(\frac{\pi}{2}\right)_x - \tau - \left(\frac{\pi}{2}\right)_y - \tau$)[79] with 3 μs pulse width and 15 μs pulse separation was employed; a single pulse sequence was used for anode spectra. Spin-lattice relaxation times (T_1) were determined by inversion recovery. For quantitative NMR determinations, pulse repeat delays were set at 10 s in order to ensure complete relaxation of the total signal.

4.3 Results and Discussion

Lithium-7 wide-line NMR spectra of graphite anodes are displayed in Figure 4-1. Results for anodes prepared under three different conditions are included; stored in the 60% charged state at 50°C, at 70°C, and cycled three times at ambient temperature (25°C). All anodes were then discharged. Two sets of spectra are shown for each of the three preparations, in one case the electrodes were rinsed in dimethyl carbonate (DMC) prior to being stripped from the current collector, and in the other case they were not. The spectra are all similar in appearance, with a single relatively broad line centered at about zero ppm, and no quadrupole satellite transitions. Thus there is no evidence of reversible intercalated Li species, which are characterized by Knight shifts of around 40-45 ppm (for the stage I and stage II intercalation compounds) and

resolved quadrupole transitions[28,38]. This verifies that the anodes were completely discharged prior to NMR analysis, and that the ^{7}Li NMR signal is mostly associated with irreversible Li compounds constituting the SEI.[28,38] Not surprisingly, the unrinsed samples exhibit higher overall spectral intensity, as determined by integration of the signals. Taking into account differences in sample quantities (determined by weighing the samples after the NMR measurements were completed) and uncertainties associated with absolute intensity measurements when changing samples, it has been established that the rinsed samples have less than about one half of the Li as the unrinsed samples. The extra Li in the latter is attributed primarily to residual electrolyte salt.

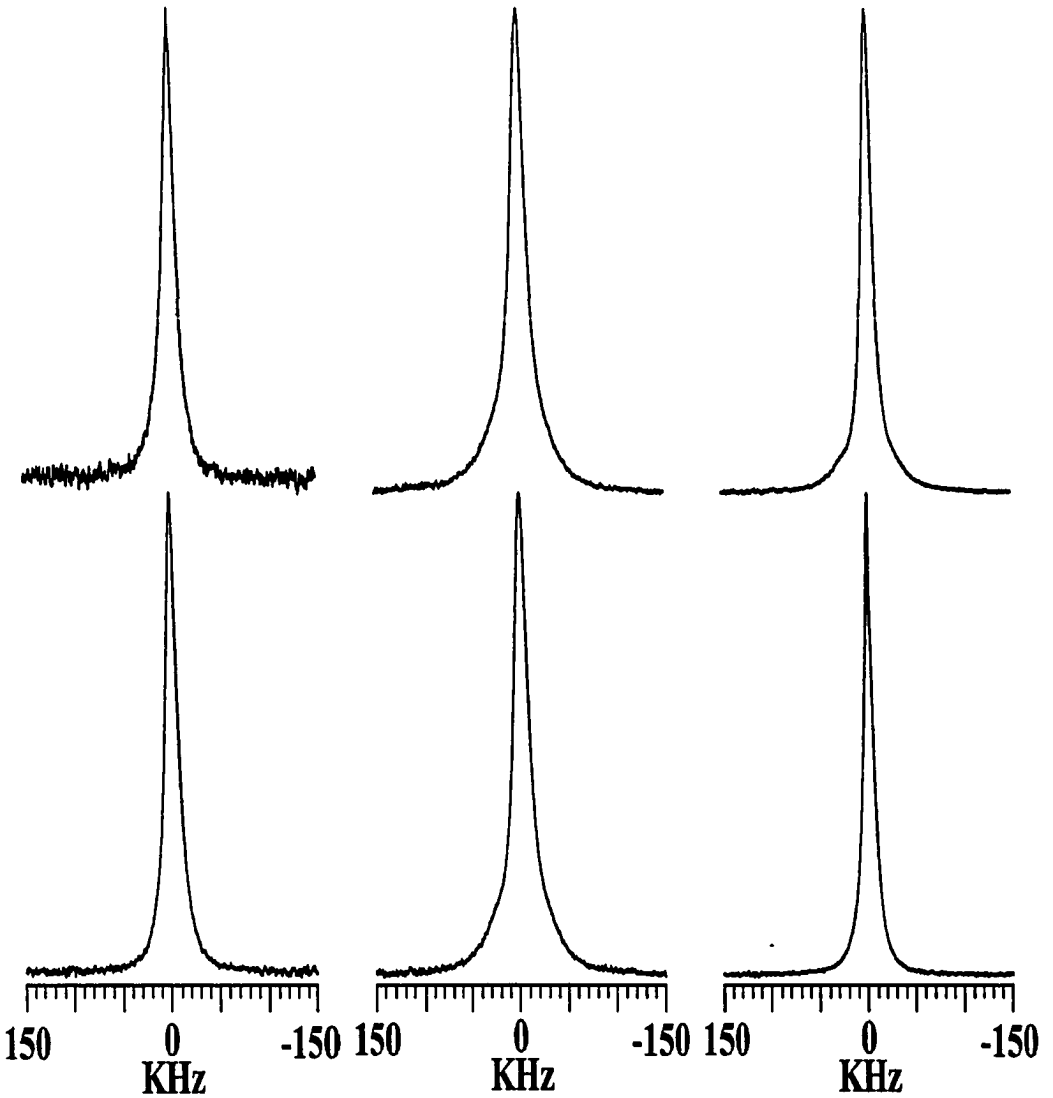

Figure 4-1 (left to right) ^{7}Li NMR spectra of discharged anodes stored in the 60% charged state at 50°C, at 70°C, and cycled three times at ambient temperature (25°C).(top) Anodes rinsed in DMC. (bottom) Unrinsed anodes.

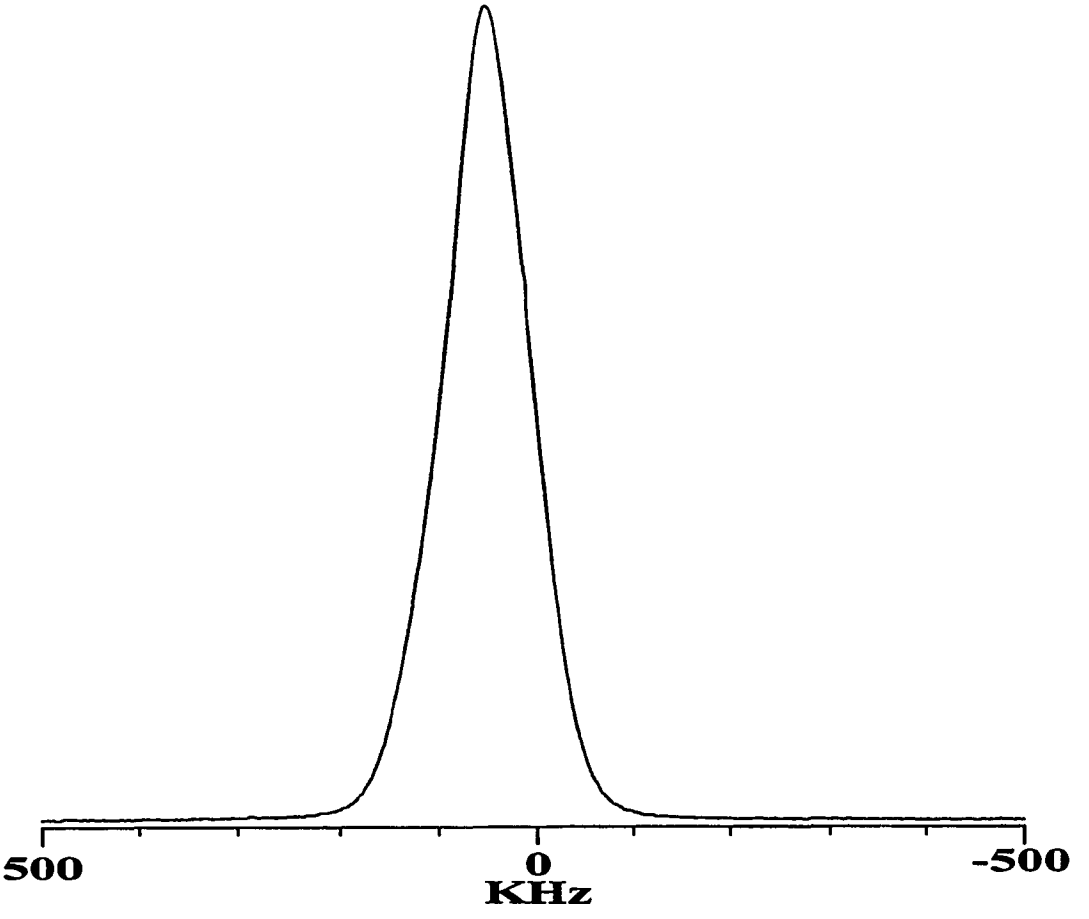

Figure 4-2 ^{7}Li NMR spectrum of $LiNi_{0.8}Co_{0.2}O_2$.

For comparison purposes it is most useful to examine the effect of high temperature storage on the rinsed samples. Again, after considering all the experimental factors which determine the total integrated MNR intensity, we concluded that, to within ±20% of the total intensity (including differences in sample mass), the 70°C storage does not produce appreciably more SEI than storage at 50°C. The observation that SEI formation can be accelerated at elevated temperature is

probably correlated with cell performance degradation (even failure) in high temperature aging tests. However, any difference in anode SEI content between the 50 and 70°C storage is within the experimental uncertainty and, in any case, most of the impedance rise associated with aging is attributed to the cathode[34]. The same kind of analysis can be employed to monitor SEI growth as a function of cycle number, but in this investigation we show results for only three cycles.

Of even greater interest, however, is the analysis of NMR spectral intensities on the cathode side, because of the previously mentioned dearth of cathode SEI-formation studies and the critical role that cathode aging plays in cell degradation. Figure 4-2 displays a wide line ^{7}Li NMR spectrum of pure active cathode, $LiNi_{0.8}Co_{0.2}O_2$. There is a single broad resonance centered at 580 ppm, characteristic of the strongly paramagnetic Ni^{3+} environment. The presence of a single peak indicates the absence of nanoscopic phase segregation of Co-rich regions, which yield a diamagnetic environment with a resonance near 0 ppm, in addition to the Ni^{3+} response.[40]

Figure 4-3 shows ^{7}Li spectra of three sets of cathodes corresponding to the same cells from which the anodes were taken. Again, spectra for both rinsed and unrinsed cathodes are presented. All of these spectra contain two identifiable Li environments, one associated with the stoichiometric $LiNi_{0.8}Co_{0.2}O_2$ phase, and a second with the cathode SEI. These two environments are also characterized by vastly different T_1 values, less than 10 ms for the $LiNi_{0.8}Co_{0.2}O_2$ phase, and on the order of seconds for the SEI. The greater apparent NMR intensity of the latter phase in the unrinsed cathodes is, again, attributed to the presence of residual electrolyte salt. Comparison

between the zero ppm components of rinsed and unrinsed cathodes yield a shorter average T_1 for the former. This is consistent with selective inversion measurements in unrinsed cathodes which show different phases with different relaxation times, longer for the materials higher in lithium salts (i.e., from residual electrolyte in the unrinsed cathodes). Because of the "baseline" NMR signal from the pure $LiNi_{0.8}Co_{0.2}O_2$ component of the cathode, it is quite straightforward to compare relative integrated intensities of the SEI phase between different samples. This idea is illustrated in Figure 4-4, in which one of the cathode spectra is simulated by two components of specific intensities corresponding to the number of Li nuclei in those phases. Comparing results for rinsed cathodes, this analysis shows that storage at 70°C yields a Li-containing SEI about 10% greater than that present in the 50°C cathodes. It is also clear that the cathode cycled at room temperature builds up an SEI that is similar in spectral appearance to those of the cathodes stored at elevated temperature, although somewhat less abundant than the latter.

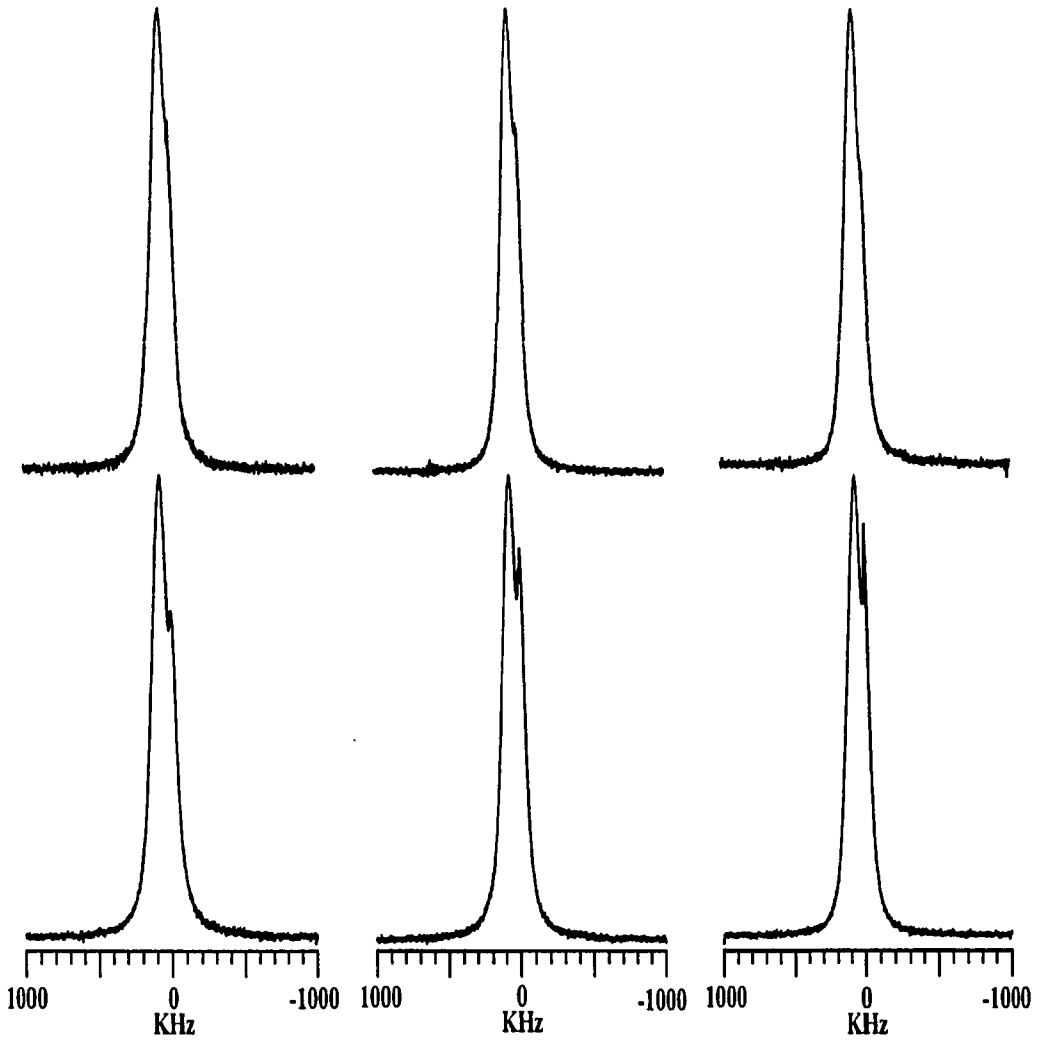

Figure 4-3 (left to right) ^{7}Li NMR spectra of discharged cathodes stored in the 60% charged state at 50°C, at 70°C, and cycled three times at ambient temperature (25°C). (top) Cathodes rinsed in DMC. (bottom) Unrinsed cathodes.

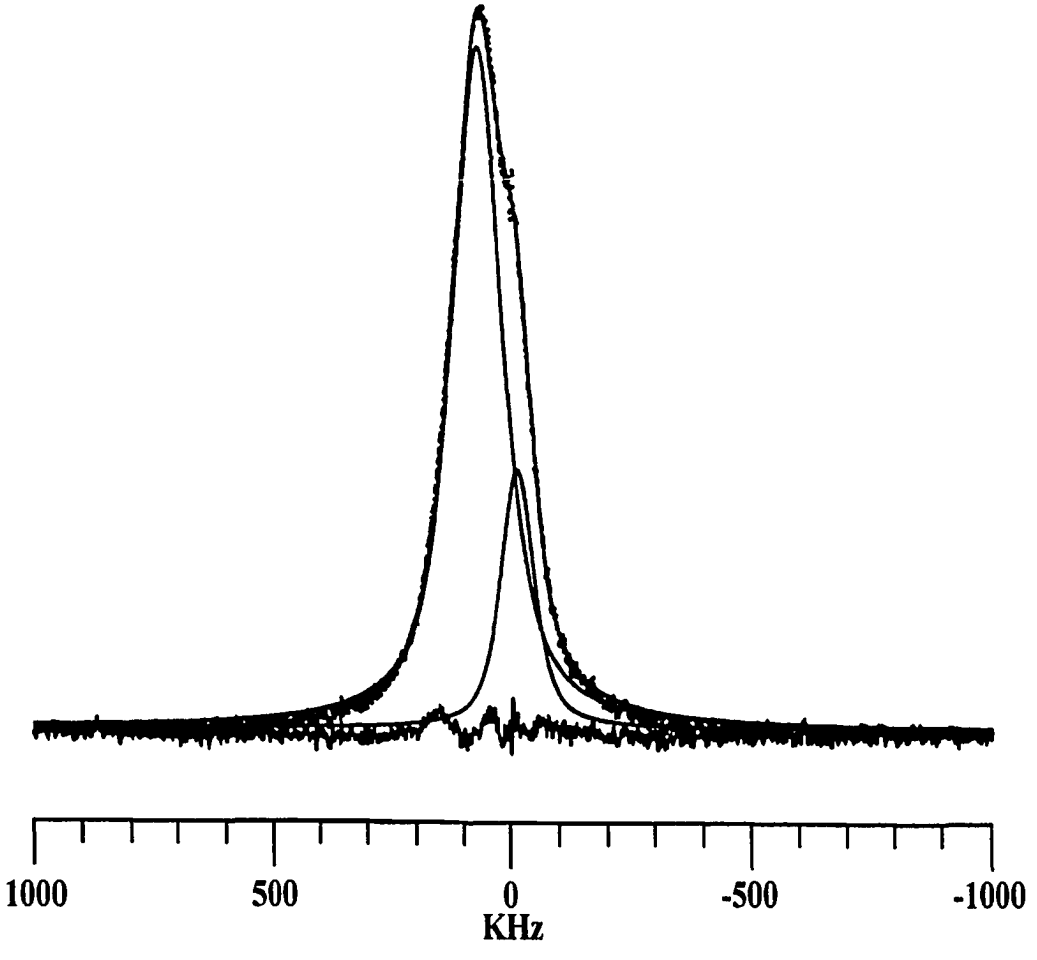

Figure 4-4. Experimental and simulated ^{7}Li NMR spectra of rinsed cathode stored at 50°C. The bottom trace is the difference between experimental and simulated spectra.

CHAPTER 5

^{7}Li NMR Studies of Iron Substituted Lithium Nickelate

(Collaboration with F.Ronci and B.Scrosati, Department of Chemistry, University of Rome, Italy, where the materials were prepared and characterized by XRD)

5.1 Introduction

As mentioned previously, it is very difficult to prepare $LiNiO_2$ with ideal stoichiometry, and consequently most preparations suffer from capacity fade upon cycling due to irreversible structural changes. $LiNiO_2$ is a member of the series $Li_xNi_{2-x}O_2(0 \leq x \leq 1)$[41, 49-54] and partial cation ordering occurs for $x>0.6$[54] with some Ni ions in Li layers. In fact, its actual formula must be written as $Li_{1-z}Ni_{1+z}O_2$. This departure from theoretical $LiNiO_2$ stoichiometry results simultaneously from the small difference in size between Li^+ and Ni^{3+} and from the instability of Ni^{3+} which entails the presence of Ni^{2+} within the material. The Ni^{2+} in the Ni rich layers require the same amount of Ni^{2+} ions to be present also in Li rich layers for charge neutralization. The Ni ions in the Li layers not only directly decrease the utilization of Li_xNiO_2 but also impede the Li ion diffusion, resulting in a dramatic worsening of the cycling properties.[55,56] Substituting foreign cations such as Co[42], Mn[43], or Fe[44,45] with Ni is commonly used to improve the 2D character of the $LiNiO_2$ structure and to enhance the cycling ability. Iron substitution seems interesting mainly because of its much lower cost and nontoxicity compared to cobalt.

A very important purpose consists in finding methods of synthesizing $Li(Ni_{1-x}Me_x)O_2$ close to the ideal stoichometry and structure. The "solid state" method is usually performed mixing the precursor powders by grinding, pressing the mixture into pellets and finally firing the pellets at the appropriate temperature. Alternatively the "soft chemistry" method consists of dissolving the precursor salts in an appropriate solvent in order to obtain a solution that is dried until a powder is produced. This powder then undergoes the firing treatment as in the solid state method. The aim of this procedure is to produce a precursor mixture with the reagents mixed at a molecular level. The normal soft chemistry method uses organic compounds as complexing agents for transition metal cations, and easily give carbon contaminated compounds because organic compounds decompose to carbonates.[57] In this work, nitrate salts were used as precursor to synthesize $LiNi_{1-x}Fe_xO_2$ ($0.1 \leq x \leq 0.3$), no organic compound being added. Different firing time sequence and temperature were used to produce a series of samples. $LiNi_{1-x}Co_xO_2$ ($0.1 \leq x \leq 0.3$) were also synthesized to investigate the effect of different substituted species on the structure. ^7Li NMR spectroscopy was used to characterize the structure of the $LiNi_{1-x}Fe_xO_2$ materials. As a probe of the immediate environment of the nucleus under investigation, NMR is an ideal method for investigating the small changes in local structure that occur with variable cation substitution or firing procedure.

5.2 Experimental

Various samples studied by NMR are listed in Table 5-1. The first six samples have different composition and have been synthesized under the same condition using

the nitrate "soft chemistry method" described in reference [66,67]. Samples 7-11 which were synthesized by the classical solid state method, with the same nominal composition, have been studied as a function of increasing firing temperature. Samples 12-14 have the same composition as samples 1-3 but the firing time is 12 hours instead of 5 hours. Samples 15 and 16 are respectively samples 2 and 5 fired for additional two cycles of 5 hours (total time is 15 hours). All samples were heated in a pure oxygen atmosphere in order to prevent Li loss via Li_2O sublimation.

Samples were packed in 5mm O.D. NMR tube. The two-pulse quadrupole echo excitation sequence ($\left(\frac{\pi}{2}\right)_{0^\circ} - \tau - \left(\frac{\pi}{2}\right)_{90^\circ} - \tau$) was used in measurements in order to eliminate instrument deadtime effects and thus obtain undistorted spectra, and 1M aqueous LiCl solution was used as a chemical shift reference.

5.3 Results and discussion

5.3.1 The effect of synthesis temperature

Figure 5-1a shows the room temperature ^7Li spectra for the $LiNi_{0.9}Fe_{0.1}O_2$ samples 7-11 which were synthesized by solid state method firing at different temperatures. The spectral line width of the samples with firing temperature lower than 700°C (samples 7-9) is symmetric, relatively narrow, and the center of the spectrum is close to the position of the reference LiCl solution. Sample 10 and 11 were fired at 700°C and 800°C, respectively and their spectral line width becomes drastically broader

compared to the previous samples. Figure 5-1b plots the linewidth vs firing temperature and gives a more detailed visualization of these changes. The spectra of sample 10 and 11 may be separated into at least two components. C.Marichal et al.[46] and P.Ganguly et al[47] reported a shift of 650 ppm and 580 ppm respectively in the position of the central transition of ^7Li in $LiNiO_2$ synthesized by the same method. They interpreted this shift in terms of Li ions interacting with paramagnetic Ni^{3+} as its nearest 3d series transition metal neighbors. Thus, the first component, which is strongly shifted to high frequency direction (peak position between 420~530 ppm), can be assigned to Li ions located at 3b octahedral sites. The second component is centered around –300 and –400 ppm and its intensity decreases with increasing firing temperature. The origin of this second peak will be discussed later. There is a third peak close to the LiCl reference position and its relative intensity essentially has no change with increasing firing temperature. This third feature, characteristic of a diamagnetic enviroment, could come from the same source as those samples of lower synthesizing temperature (sample 7-9), which, we believe, is from the residual precursors of the samples. The Thermo Gravimeter Analysis (TGA) and Differential Thermal Analysis (DTA) demonstrate that temperature of about 700°C must be reached in order to obtain the completely reacted samples. The NMR results show correspondingly large changes at and above the 700°C firing temperature. The simulation of the spectra results are summarized in Table 5-1. Gaussian+Lorentzian peak type was used in the simulation by using software PeakFit (by Jandel Scientific Software, now SPSS).

5.3.2 The effect of synthesis method

Figure 5-2 shows the ^{7}Li NMR spectra of $LiNi_{0.9}Fe_{0.1}O_2$, sample 1 and sample 10, synthesized at the same temperature of 700°C by nitrate and solid state synthesis methods, respectively. The ^{7}Li NMR spectrum of the nitrate precursor sample shows a little asymmetry with a dominant feature at 479 ppm which can be assigned to Li ions in octahedral 3b sites. A small shoulder with relative intensity less than 7% of the total is observable at -396 ppm. The spectrum of sample 10 has two obvious features as discussed in Figure 5-1a and also the same two components with much different relative intensities as sample 1. The static ^{7}Li NMR spectrum should consist of only one broad peak centered at about 600 ppm, as in $LiNiO_2$.[46,47] The XRD measurements on the series samples synthesized by solid state show the presence of foreign peaks that disappear at 800°C. Furthermore, the relative intensities of the Bragg peaks of the main phase are not as the same as expected in the ideal $LiNiO_2$ structure. Most probably this is due to cation disordering. As for the nitrate synthesized samples, the XRD spectra are as expected and can be simulated to obtain the appropriate lattice parameters[68] . The ^{7}Li NMR spectra of nitrate synthesized samples have much lower relative intensity of the feature at -400ppm than those of samples synthesized by solid state method. Thus, peak at –400 ppm can be used as a criterion for estimation the purity and/or cation mixing of $LiNi_{1-x}Fe_xO_2$. Although this criterion is only qualitative, it is still much more sensitive than XRD spectroscopy.

5.3.3 The effect of Fe substitution

Figure 5-3a shows samples having various ratio of Ni/Fe under the same synthesis condition. These samples were all fired at 700°C by applying the soft chemistry method. All spectra show a feature shifted to high frequency previously attributed to $LiNiO_2$[46,47]. At low frequency side, a shoulder shows up around –400ppm ~ -500ppm. The relative intensity of the shoulder increases with the increment of Fe/Ni ratio, as shown in Figure 5-3b. This is consistent with the results of XRD measurement that subtituting Fe ion will increase the cation mixing degree, i.e. more Ni^{2+} or Fe^{3+} ions will distribute in the Li-rich layers. The width of the –450 ppm feature also increases with Fe/Ni ratio indicating the substituting of Fe ion creates larger local distortion.

5.3.4 Effect of firing time

Spectra of soft chemistry synthesized samples with the same nominal Fe/Ni ratios but different firing time are shown in figure 5-4. As the firing time increases, The widths of the respective spectra exhibit little or no change. The center of gravity of the spectra shifts a little toward low frequency side. The spectrum with $x = 0.3$ shows a peak at –74 ppm when only fired for 5 hours which disappears after 12 hours heat treatment. After 15 hours firing at 700°C, the spectrum of sample $LiNi_{0.8}Fe_{0.2}O_2$ has only one dominant feature at high frequency side that is assigned to Li^+ at 3b site, indicating that the reaction is complete. The XRD spectra show sharper peaks in the

spectra of samples treated for 12 hours in comparison with that for just 5 hours, suggesting an improvement in the long range ordering. Thus, the -400~ -500ppm feature should be assigned to Li^+ located at the vicinity of defeats or the sites with larger structure distortion, consistent with the result of section 5.3.3.

5.3.5 Effect of substituted ion species

Figure 5-5 shows the four pairs of the spectra of $LiNi_{1-x}Me_xO_2$, where the two substituted cations Me = Fe, Co are directly compared. For Co substituted samples, the spectra are much narrower than those of Fe substituted samples. This can be explained based on the difference of radius between Fe^{3+} and Co^{3+}. As reported in many works on these materials,[45,52,58-62] Fe^{3+} should be in the high spin (HS) state, while Co^{3+} and Ni^{3+} ($t^6_{2g}e^1_g$, R_{LS} = 0.56 Å) should be present in the low spin (LS) configuration. Since the radius of Fe^{3+} ($t^3_{2g}e^2_g$, R_{HS} = 0.645 Å) is larger than that of Co^{3+} ($t^6_{2g}e^0$, R_{LS} = 0.545 Å)[48], doping Fe^{3+} into the host of $LiNiO_2$ will lead to a larger distortion of local structure such as the Li-O-Ni/Fe bond length and bond angle. Furthermore, Fe^{3+} is paramagnetic enhancing the spectrum broadening while Co^{3+} is diamagnetic resulting in a narrower spectrum. The C.O.G. (center of gravity) of these spectra are summarized in Table 5-2 and displayed in Figure 5-6. The corresponding C.O.G. of the spectrum of $LiNi_{1-x}Fe_xO_2$ is smaller than that of $LiNi_{1-x}Co_xO_2$ due to the large intensity belonging to the peak between –400 ppm and –500ppm. The Fe substituted samples have larger lattice parameters. Based on the XRD measurement of these samples, the structure of Co substituted samples is not

ideal yet, with a small amount of Ni^{2+} ions in the Li layers; and sample $LiNi_{0.9}Fe_{0.1}O_2$ has almost ideal structure with negligible Ni^{2+} and/or Fe^{3+} ions in Li layers. Studying the relative spectral intensity of Co doping samples collected in Table 5-1, The peak close to the zero ppm and the peak at 700 ppm indicate phase separation into Co^{3+}-rich region and Ni^{3+}-rich region, respectively. After 15 hours firing time, Co^{3+} ions will distribute randomly in Ni slabs and only one peak was observed as shown in Figure 5-5. C.Marichal et al observed the similar clustering of Co in $LiNi_{1-y}Co_yO_2$ ($0 \leq y \leq 1$) solid solution[46]. A similar analysis can be applied to Fe substituted samples.

Comparing the spectra of two samples of 15 hours firing time, both spectra can be simulated by a single site, indicating Ni^{3+} and Fe^{3+} ions are also distributed randomly in MeO_6 (Me=transition metal) layers. Therefore, the peak at -400 ppm to -500 ppm of $LiNi_{1-x}Fe_xO_2$ results from the clustering of Fe^{3+} ions with all/most of the six nearest metal ion neighbors of Li^+ are Fe^{3+} ions. The segregation is a local phenomenon since XRD measurement shows patterns perfectly compatible with the expected $R\bar{3}m$ space group symmetry. Despite the very short annealing times, no detectable presence of foreign peaks could be observed, even in the samples fired for just 5 hours. In addition, the difference between the XRD patterns of the 10 hours and 15 hours samples is negligible, providing yet another example of NMR's sensitivity to local structural arrangements.

By changing the time delay between the acquisition sequences, the feature around -450 ppm showed longer T_1 than the 500 ppm peak. Therefore, the ~ -450 ppm feature is attributed to a significantly different lithium environment than Li in Ni-rich

regions. A magnetic superexchange mechanism has been applied to explain the ^6Li and ^7Li NMR peak shift of lithium manganate cathode materials. Different peak shifts were ascribed to different combinations and angles of Li-O-Mn path. In addition, the different shift mechanisms between t_{2g} and e_g orbitals have been considered when applying the rules for analyzing local magnetic environments[63,64]. However, the high spin electronic configuration $t^3_{2g}e^2_g$ of Fe^{3+} can only result in paramagnetic interaction with Li^+ via Li-O-Fe path whether the bond angle is 90° or 180°. To explain the large negative shift of the Fe^{3+} associated line component requires an alternative scenario. A simple bi-octahedral V_2O_{10} model, based on indirect couplings between spins localized at vanadium, has been used to describe an anomalous diamagnetically shifted line in ^7Li NMR spectra for $Li_xV_6O_{13}$ (x>2)[65]. Applying the same model to the present case, the distortion of FeO_6 lifts the degeneracy of the five d orbitals of iron. The bi-octahedral Fe_2O_{10} unit donates d electrons to the lowest t_{2g} "molecular" levels. Depending on the energy separation between the levels, either high-spin or low-spin alignment may occur. The –450ppm shift could be a complete antiferromagnetic ordering of the spins on surrounding iron atoms. Since this is only local phenomenon, there is no contradiction of the result of high spin state of Fe^{3+} based on X-ray diffraction. Another possible explanation is that the distorted octahedral field is so strong that Fe^{3+} is in the low-spin state. Low spin Fe^{3+} makes e_g orbitals less than half filled, which will result in the transfer of negative spin density into the Li^+ 2s orbital via σ bonding arrangement with 2p oxygen orbital[63].

5.3.6 Variable temperature NMR experiment

Figure 5-7 displays ^{7}Li NMR variable temperature (–140 to 200°C) spectra of $LiNi_{0.9}Fe_{0.1}O_2$ synthesized by the solid state method at 600°C. Only one dominant peak is present. The center of gravity of the peak shifts from -90 ppm to –54 ppm with increasing temperature. No significant motional narrowing effect can be observed within the whole temperature range. The variable temperature behavior of this sample indicates only a small percentage of paramagnetic material (i.e. Ni^{3+}) has been produced, and thus the precursors are far from complete reaction. Figure 5-8 shows ^{7}Li NMR spectra of $LiNi_{0.7}Fe_{0.3}O_2$ synthesized at 700°C for 12 hours by soft chemistry method. The room temperature spectrum displays two dominant peaks as in Figure 5-3a. As the temperature increases, the separation between the two peaks decreases as does the overall line width. The other nitrate route synthesized samples show similar temperature-dependent behavior and the temperature-dependent peak shifts of these samples are plotted in Figure 5-9.

The result confirms that 700°C is the proper temperature for synthesizing Fe substituted lithium nickelate even if 700°C may seem to be a value too close to the minimum limit necessary for reaction completeness as indicated by the TGA and DTA data.

5.4 Conclusions

Soft chemistry route and solid state route synthesized $LiNi_{1-x}Me_xO_2$ (Me=Fe,Co) where $0.1 \leq x \leq 0.3$ have been studied via ^7Li NMR spectroscopy. For annealing temperatures < 600°C, the resonance width and shift of samples by solid state route are significantly narrower and smaller than those fired above 700°C. The NMR results show complete conversion to Ni^{3+} by 700°C, implying all Ni ions reside in the ideal layered structure corresponding to NiO_6 layers. ^7Li NMR spectra of Fe substituted samples of short firing time show at least two local phases that cannot be detected by XRD measurement. Substituting Fe creates larger distortion to local structure than substituting Co.

Comparing the two synthesis methods, the soft chemistry method is superior to solid state method as it needs much lower temperature for complete reaction of the precursors. Keeping a low annealing temperature is important from the point of view of practical applications.

Table 5-1 Simulation results of the peak position and relative intensity of the spectra of samples 1-16.

Index	Nominal composition	Peak 1 δ(ppm)/%	Peak 2 δ(ppm)/%	Peak 3 δ(ppm)/%	Peak 4 δ(ppm)/%	HWFH (KHz)	Synthesis conditions
1	$LiNi_{0.9}Fe_{0.1}O_2$	-397 / 6.8 %		476 / 93.2 %		148	Nitrates 5h @ 700°C in O_2
2	$LiNi_{0.8}Fe_{0.2}O_2$	-399 /32.0%		501 / 68.0%		201	Nitrates 5h @ 700°C in O_2
3	$LiNi_{0.7}Fe_{0.3}O_2$	-504 / 28.4 %	-74 / 17.9 %	552 / 53.7 %		224	Nitrates 5h @ 700°C in O_2
4	$LiNi_{0.9}Co_{0.1}O_2$			470 / 100 %		117	Nitrates 5h @ 700°C in O_2
5	$LiNi_{0.8}Co_{0.2}O_2$		-37 / 40.7%	386 / 24.3 %	676 / 35.0%	125	Nitrates 5h @ 700°C in O_2
6	$LiNi_{0.7}Co_{0.3}O_2$		4.5 / 50.3 %	407 / 28.3 %	775 / 21.4 %	112	Nitrates 5h @ 700°C in O_2
7	$LiNi_{0.9}Fe_{0.1}O_2$	-50.1 / 100 %				54	Solid state 3h @ 400°C in O_2
8	$LiNi_{0.9}Fe_{0.1}O_2$	-62.0 / 100 %				56	Solid state+ 3h @ 500°C in O_2
9	$LiNi_{0.9}Fe_{0.1}O_2$	-64.8 /100 %				58	Solid state+ 3h @ 600°C in O_2
10	$LiNi_{0.9}Fe_{0.1}O_2$	-277 / 54.8 %	-40/ 1.9 %	543 / 43.3 %		179	Solid state+ 3h @ 700°C in O_2
11	$LiNi_{0.9}Fe_{0.1}O_2$	-409 / 46.1 %	-35 / 1.9 %	537 / 52.0 %		220	Solid state+ 3h @ 800°C in O_2
12	$LiNi_{0.9}Fe_{0.1}O_2$	-406 / 12.0 %		492 / 88.0%		167	Nitrates 12h @ 700°C in O_2
13	$LiNi_{0.8}Fe_{0.2}O_2$	-535 / 22.7 %	-54 / 2.7 %	423 / 74.7 %		203	Nitrates 12h @ 700°C in O_2
14	$LiNi_{0.7}Fe_{0.3}O_2$	-504 / 30.0 %	-39 / 0.5 %	458 / 68.6 %		214	Nitrates 12h @ 700°C in O_2
15	$LiNi_{0.8}Fe_{0.2}O_2$			420 / 100 %		183	Nitrates 5+5+5h @ 700°C in O_2
16	$LiNi_{0.8}Co_{0.2}O_2$			480 / 100 %		118	Nitrates 5+5+5h @ 700°C in O_2

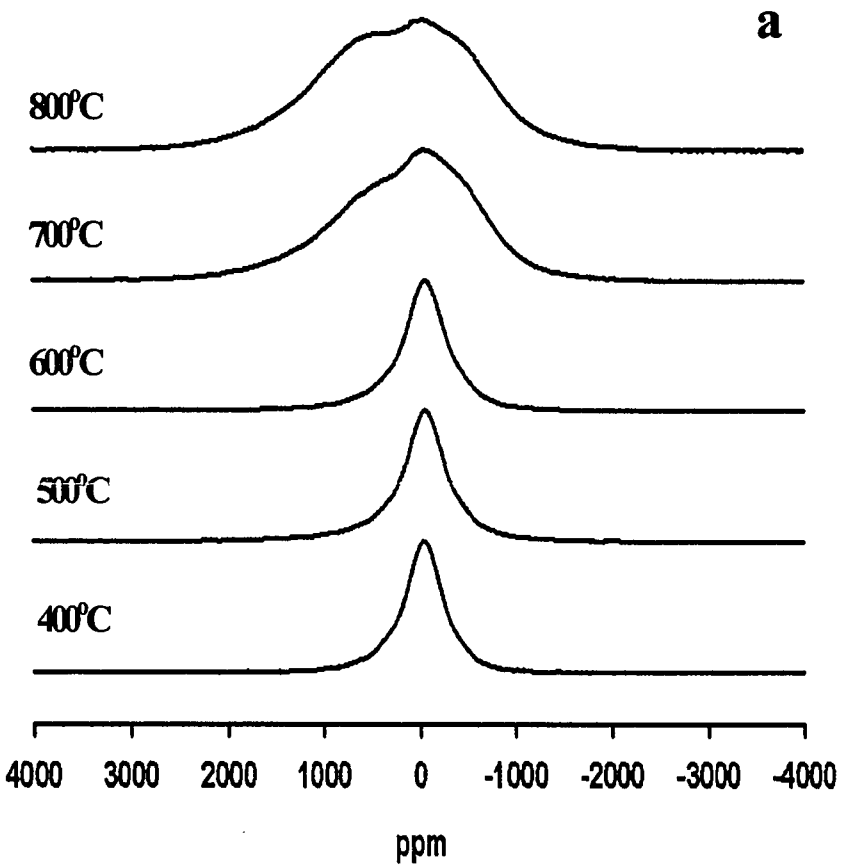

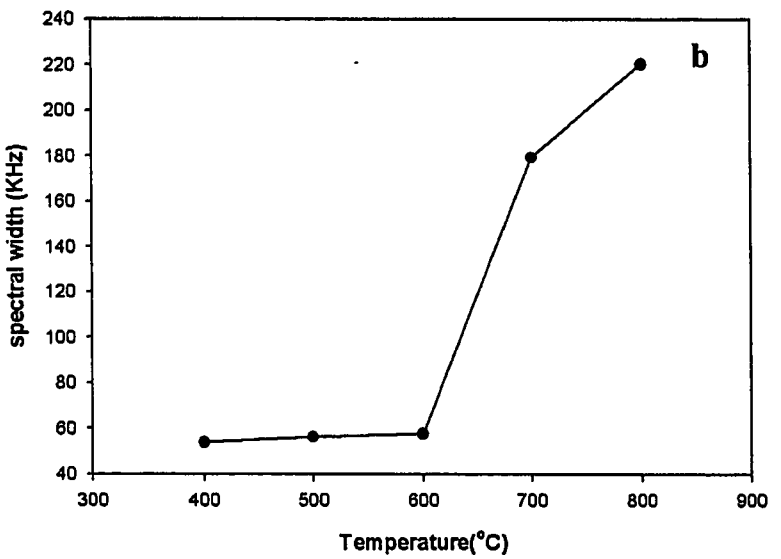

Figure 5-1 a) Li^7 NMR spectra of samples of $LiNi_{0.9}Fe_{0.1}O_2$ synthesized at different temperatures by solid state method. b) spectral width vs. temperature.

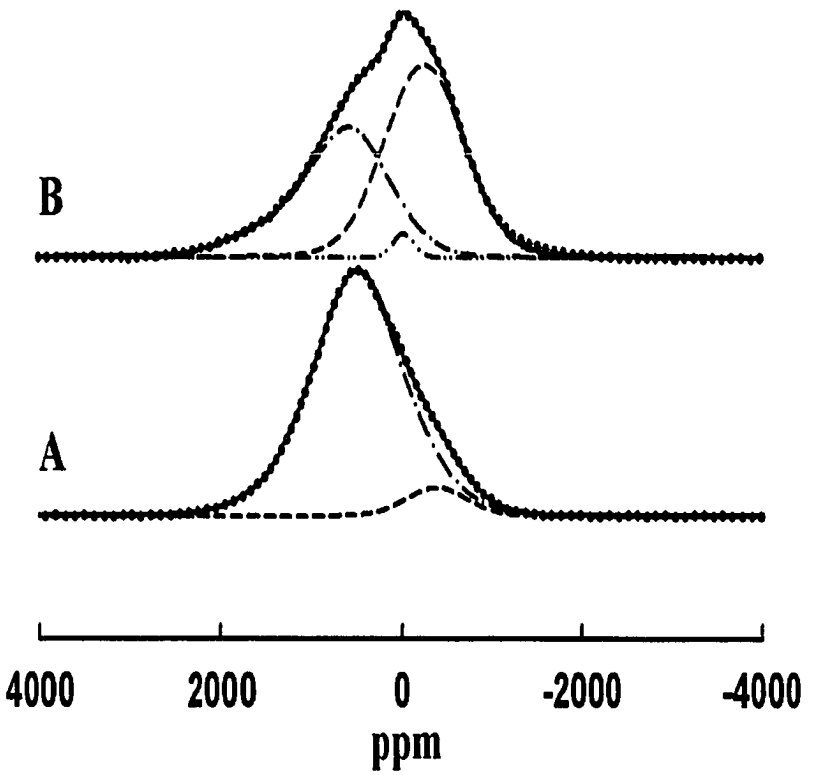

Figure 5-2 Spectra of $LiNi_{0.9}Fe_{0.1}O_2$ synthesized by different method at 700°C. The dotted lines are experiment data, solid lines are simulated data, the dashed lines are simulated peaks. A) sample 1--- Nitrate method B) sample 10--- solid state method.

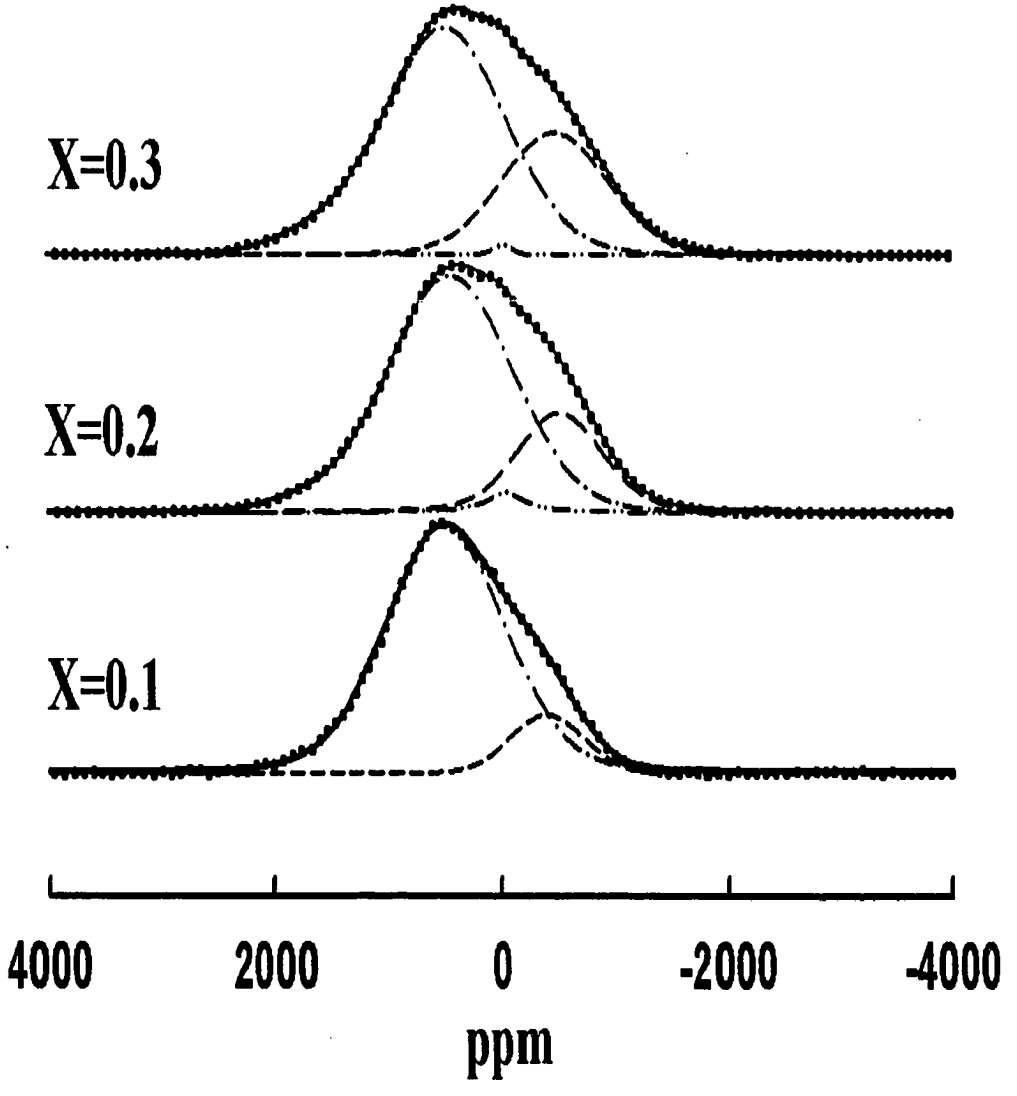

Figure 5-3.a Li^7 NMR spectra of soft chemistry synthesized $LiNi_{1-x}Fe_xO_2$. All the samples (sample 12, 13 and 14) were annealed at 700°C.

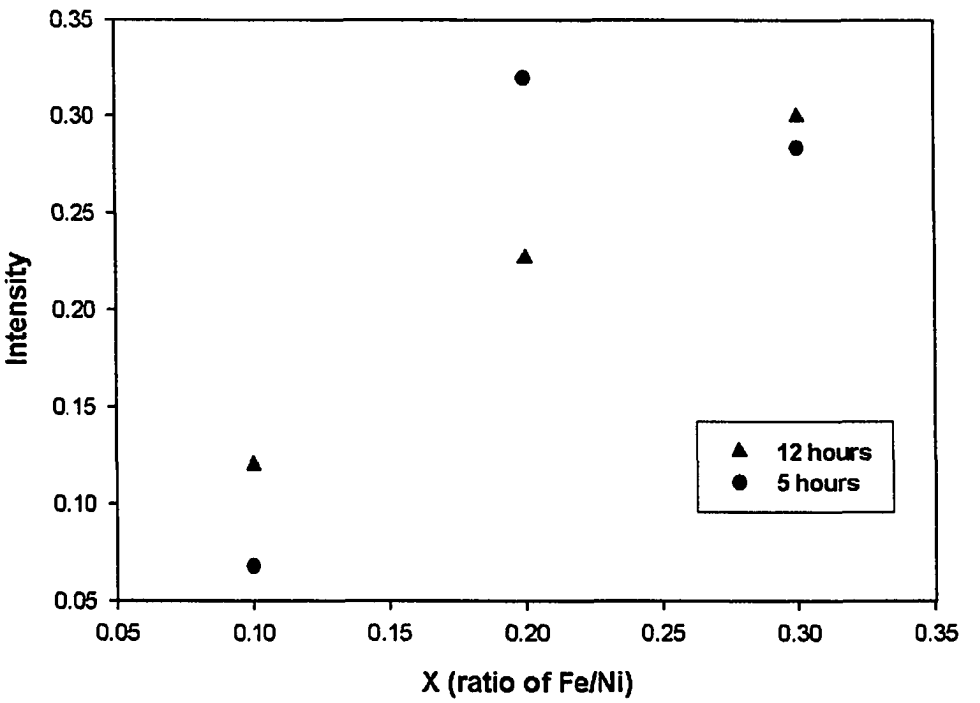

Figure 5-3.b relative intensity of the -400 ppm feature of $LiNi_{1-x}Fe_xO_2$ with 5 and 12 hours heating time.

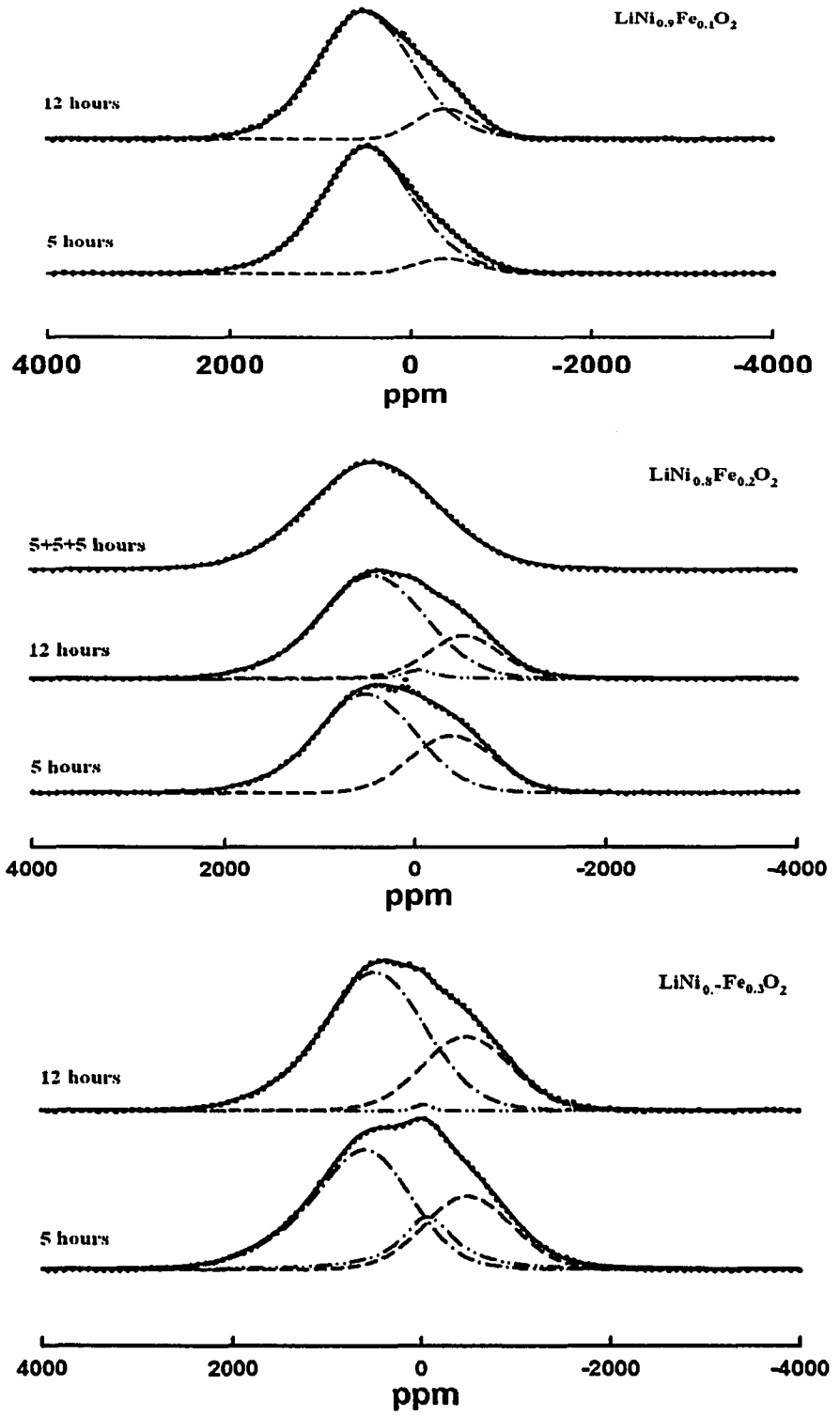

Figure 5-4 Effect of firing time on ^{7}Li NMR spectra. Dotted lines are experiment data. Solid lines are simulated data. The rest are simulated peaks.

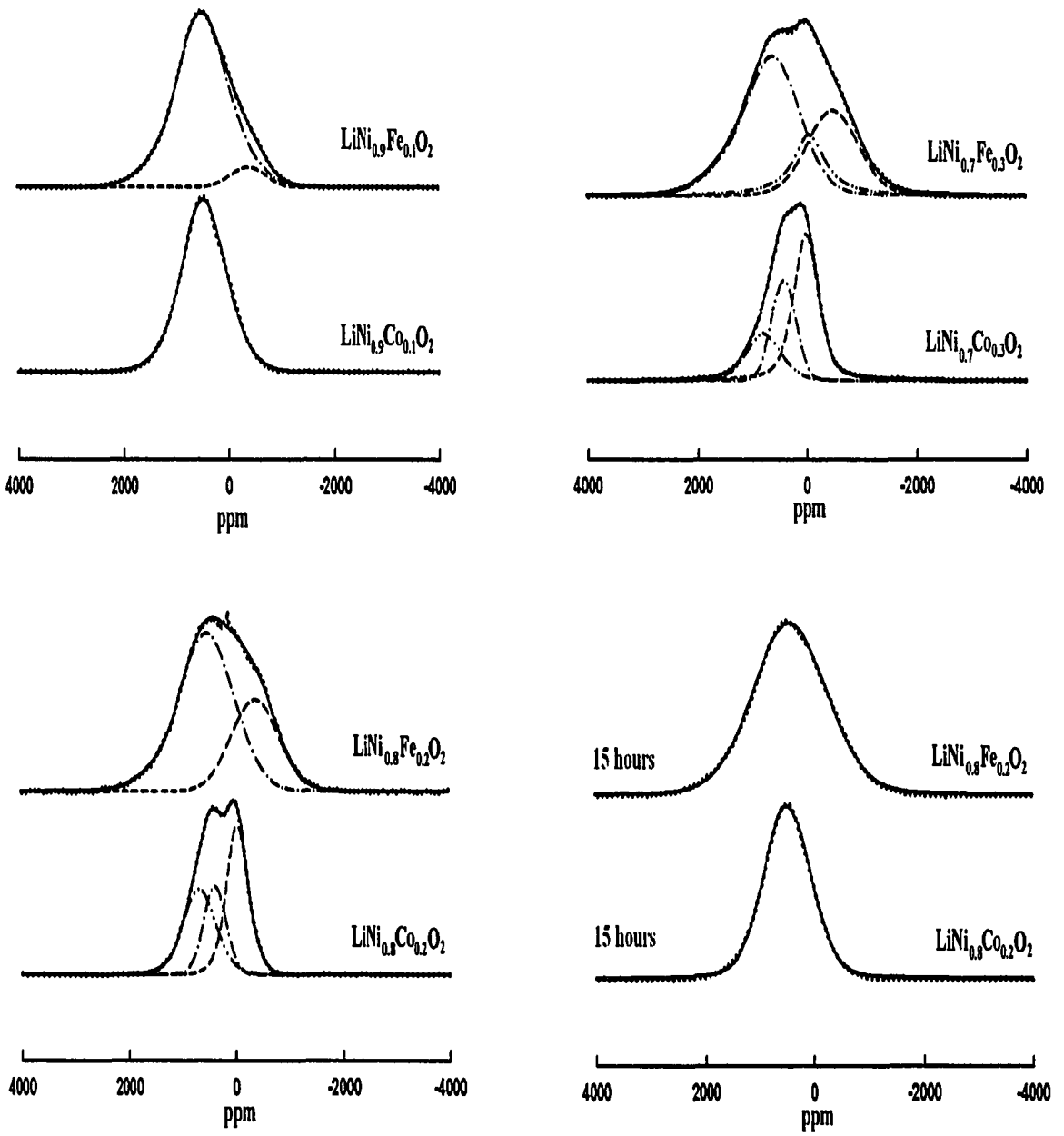

Figure 5-5 Li^7 NMR spectra of $LiNi_{1-x}Fe_xO$ and $LiNi_{1-x}Co_xO$ synthesized under same condition. All samples were fired for 5 hours excepting the two specifying 15 hours. Dotted lines are experiment data, solid lines are simulated data.

Table 5-2 Center of gravity of selected samples

Index	sample	C.O.G. (ppm)
1	$LiNi_{0.9}Fe_{0.1}O_2$	416
2	$LiNi_{0.8}Fe_{0.2}O_2$	241
3	$LiNi_{0.7}Fe_{0.3}O_2$	205
4	$LiNi_{0.9}Co_{0.1}O_2$	470
5	$LiNi_{0.8}Co_{0.2}O_2$	315
6	$LiNi_{0.7}Co_{0.3}O_2$	283
15	$LiNi_{0.8}Fe_{0.2}O_2$	420
16	$LiNi_{0.8}Co_{0.2}O_2$	480

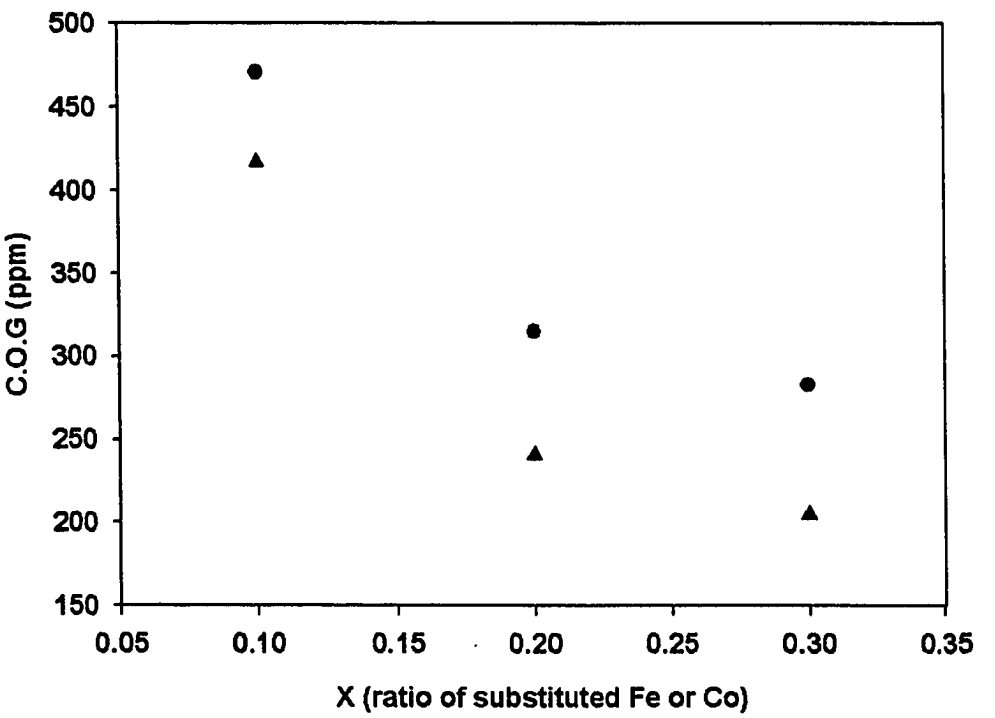

Figure 5-6 The center of gravity of the spectra of $LiNi_{1-x}Me_xO_2$ (Me=Fe,Co) vs X , the ratio of Me/Ni.

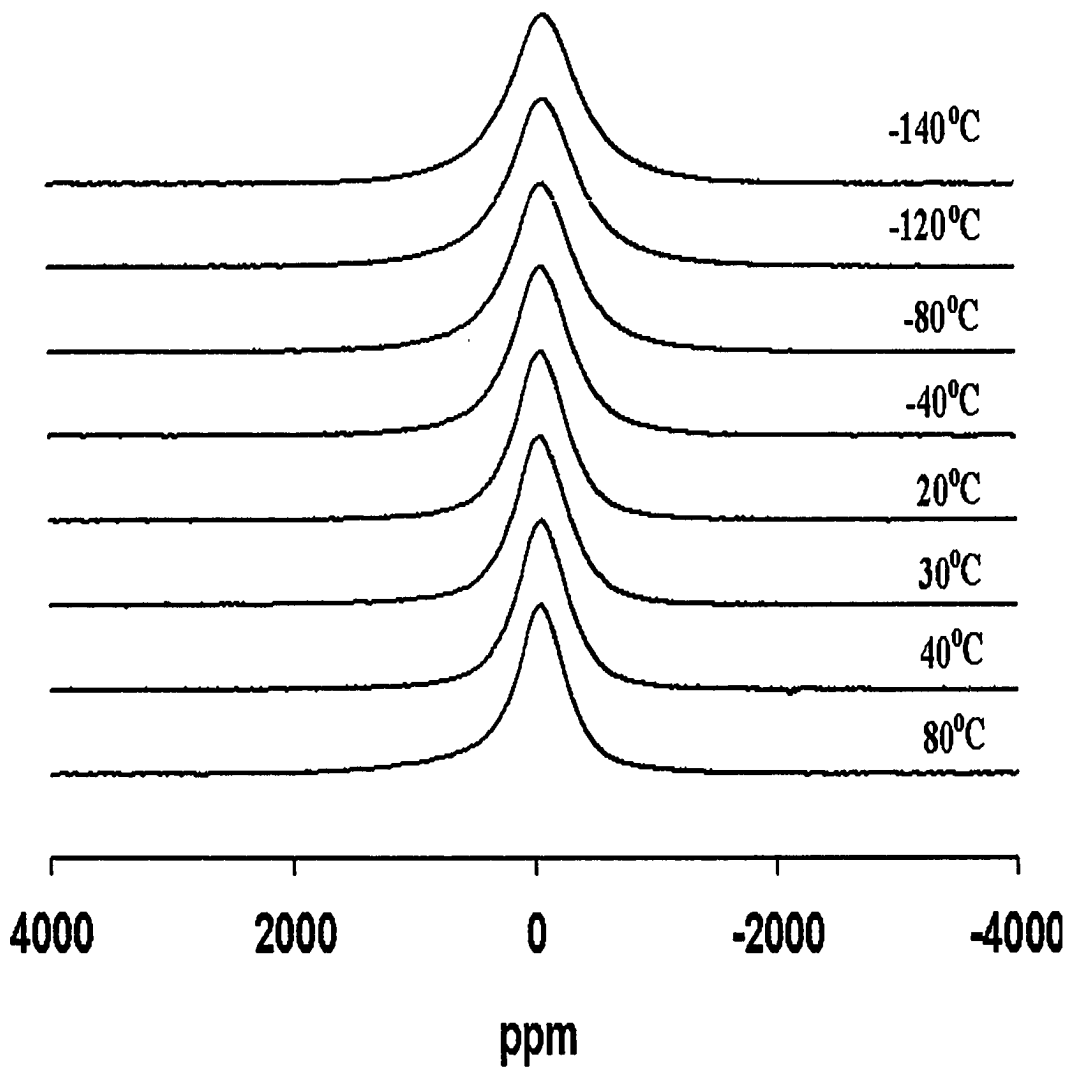

Figure 5-7 ^{7}Li NMR spectra of $LiNi_{0.9}Fe_{0.1}O_2$ vs. temperature.

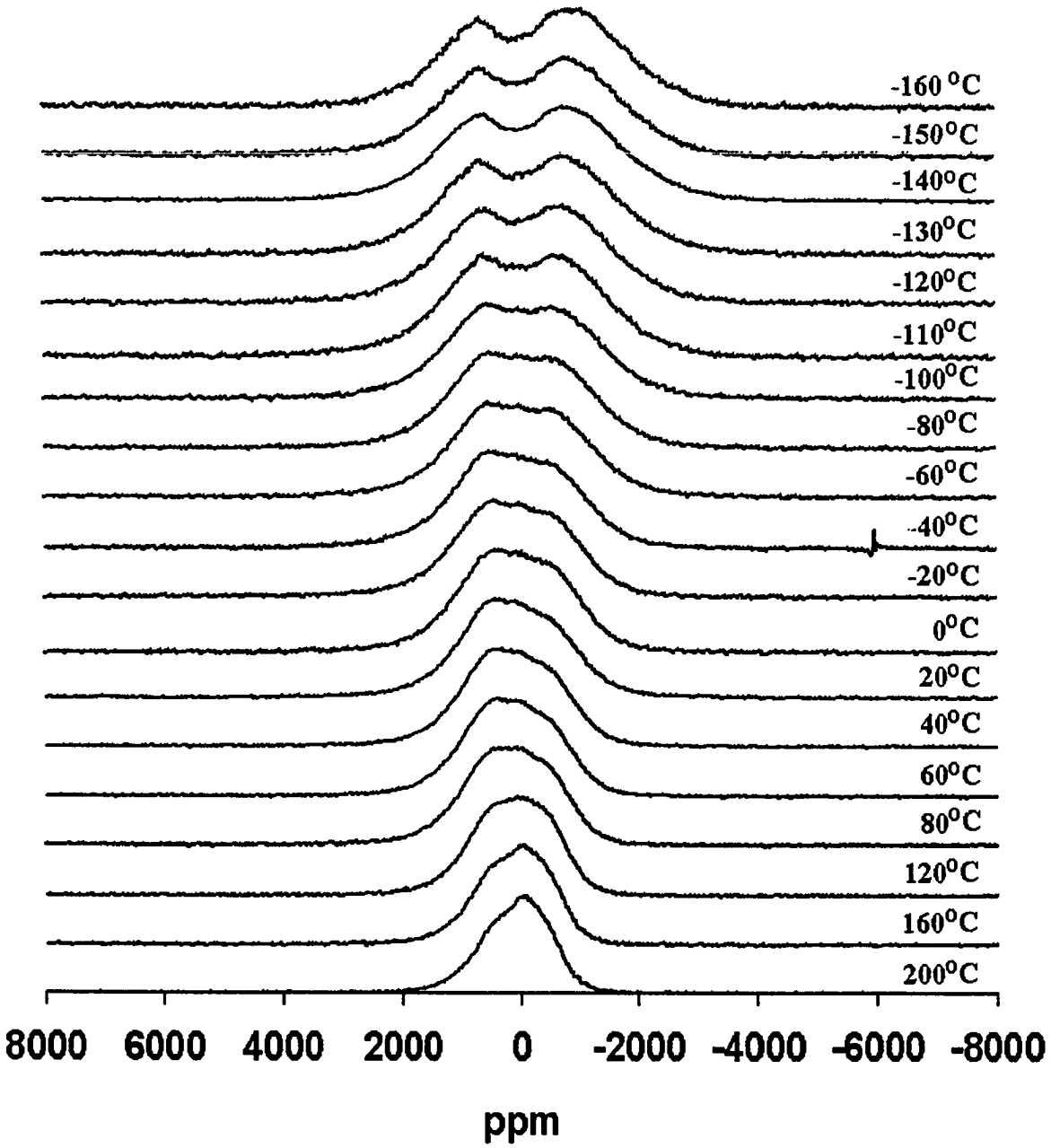

Figure 5-8 ^{7}Li NMR spectra of $LiNi_{0.7}Fe_{0.3}O_2$ vs. temperature.

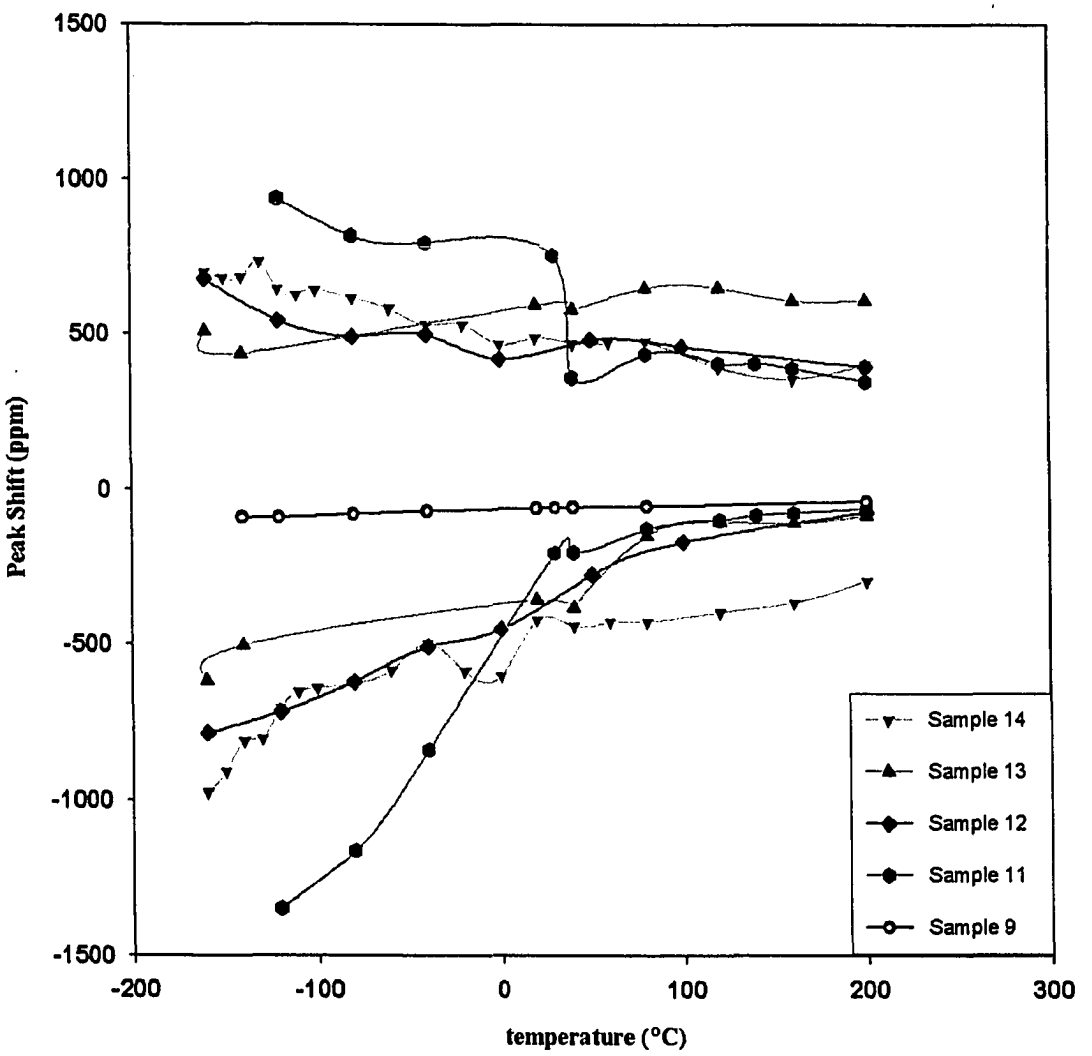

Figure 5-9 Temperature dependence of ^{7}Li NMR resonance peak shift for selected samples. The positive shift is associated with peak at 400~500ppm; the negative shift is associated with peak at -400ppm to -500 ppm. Sample 9 shows only one peak in the whole temperature region.

CHAPTER 6

Cationic Distribution of $LiCo_xNi_{1-x}VO_4$ compounds for Lithium Ion Batteries : a solid-state ^7Li and ^{51}V NMR study

(Collaboration with M.Arrabito, S.Bodoardo, N.Penazzi, Politecnico di Torino, 10129 Torino, Italy and S.Panero, P.Reale, B.Scrosati, Universita La Sapienza, 00185 Rome, Italy, where the materials were prepared and characterized by XRD, SEM(scanning electron microscopy) and CV(cyclic voltammetries).)

6.1 Introduction

The importance of lithium-ion power sources in portable electronics applications[69] has stimulated research on new types of lithium insertion electrode materials. Considerable effects are presently devoted to evaluation of high voltage, lithium-rich materials which can be employed as cathodes in Li-ion batteries. The main candidates are the layered $LiMO_2$ (M = Co, Ni)[70,71] and the spinel structures of types $LiMn_2O_4$[72].

A current trend of research is directed towards the study of positive materials with even higher voltage than the materials cited above, i.e. approaching 5 V vs. Li , in order to improve energy density values and allow the use of alternative anode materials. Towards this end, we have investigated the lithium and vanadium environments of the mixed Li transition metal vanadates like those already reported by

Fey and coworkers[73,74]. The goal of this study is to correlate the local structural characteristics of these materials with their electrochemical behavior.

The compositional dynamics of the $LiCo_xNi_{1-x}VO_4$ compounds have not been fully characterized, especially regarding the distribution of Li, Co, Ni and V tetrahedral and octahedral sites as a function of synthesis procedure. Spinel structures can be studied via XRD and information regarding the fractions of octahedral and tetrahedral Co, Ni and V can be obtained. This study employs ^7Li and ^{51}V NMR to obtain additional information concerning phase content and microstructure. NMR provides an independent quantitative measure of tetrahedral and octahedral lithium and vanadium environments as a function of composition parameter, x. The XRD data suggested that when the metal ion is Ni^{2+} or Co^{2+}, the corresponding $LiCo_xNi_{1-x}VO_4$ compounds adopt an inverse spinel structure, where Li^+ ions reside in octahedral sites, Ni^{2+}, Co^{2+} ions and V^{5+} ions can be distributed both in octahedrally and tetrahedrally coordinated sites.[75,76] This structure should allow easy removal of lithium at potentials of order of 4.2~4.8 V vs. Li, depending upon the Ni/Co ratio.

As it is well known, different preparation routes can lead to materials with different electrochemical efficiency. In order to investigate this aspect, we decided to compare various $LiCo_xNi_{1-x}VO_4$ (x=0,0.2,0.5,0.8,1) compounds via two different preparation methods, i.e. wet chemistry (WCh) and solid state (SS) routes. Previously, The XRD method, although a indispensable tool in the structural characterization of battery cathode materials, provides information averaged over hundreds of lattice sites and is relatively insensitive to the local structure variations that occur when one kind of transition metal ion is substituted sequentially for another(although it does give the

average change in lattice parameter according to Vegard's Law[89,90]). On the other hand, NMR is particularly sensitive to short range interactions, and thus yields information on short-range spatial correlations, especially when the ions being substituted into the lattice are paramagnetic.

6.2 Experimental

A compound of this family having the $LiCo_xNi_{1-x}VO_4$ composition, namely $LiCoVO_4$, $LiCo_{0.2}Ni_{0.8}VO_4$, $LiCo_{0.5}Ni_{0.5}VO_4$, $LiCo_{0.8}Ni_{0.2}VO_4$ and $LiNiVO_4$ have been considered in this work. These compound have been synthesized by two different preparation methods: a WCh and a SS route.

In the WCh preparation, the precursors, $Co(NO_3)\cdot 6H_2O$, $Ni(NO_3)\cdot 6H_2O$, $LiOH\cdot H_2O$ and NH_4VO_3 were dissolved in water. Mixing of the solutions resulted in a brownish suspension. After prolonged stirring for assuring homogeneity, the solvent was evaporated, the precipitate collected, ground and calcined at 120°C for 12 hours. The powders were then reacted in air by rapidly heating to 400°C, then annealed at 500°C. The annealing time at each temperature was 48 hours.

In the solid state route the precursors were $LiCO_3$, CoO, NiO, V_2O_5. These precursors were finely ground in a ball mill before the annealing at 530°C. The samples were annealed for about 200 to 230 hours, and during this time the powders were ground each 24 hours to reduce grain dimensions.

$LiCo_xNi_{1-x}VO_4$ samples were packed into 5 mm OD pyrex tubes for the NMR measurements. Both simple ($\pi/2$ pulse) and two-pulse solid echo excitation

sequences $\left(\frac{\pi}{2}\right)_X - \tau - \left(\frac{\pi}{2}\right)_Y - \tau - acq.$ were employed. A typical $\pi/2$ pulse width was 2.5 μs. The pulse separation in the solid echo sequence was 150 μs for preliminary measurement; then variable τ from 10 μs to 500 μs were used for detailed measurement. Chemical shift references were aqueous solutions of LiCl and $VOCl_3$.

6.3 Results and Discussion

^{7}Li NMR spectra of all samples are displayed in Figure 6-1. The spectrum of $LiNiVO_4$ is a relatively narrow line with no evidence of quadrupole satellite transitions, consistent with Li ions in an undistorted octahedral environment. Substitution of Co^{2+} for Ni^{2+} broadens the ^{7}Li resonance line significantly due to the strong magnetic dipolar interaction with spins localized on the Co site. In sample compositions for which both preparation mechanisms were employed, the ^{7}Li NMR lineshapes are substantially different, reflecting a different spatial distribution of paramagnetic Co^{2+} ions with respect to the Li^+ ions. An example of this is shown for $LiCo_{0.5}Ni_{0.5}VO_4$. The linewidth of the solid synthesis sample is narrower than that of the wet chemistry synthesis material, and the peak positions of the two lines differ, with the SS peak appearing between the main peak and observable shoulder of the WS sample. This is consistent with a statistically random distribution of Li-Co spatial correlations in SS as opposed to a non-random distribution in WCh.

A similar effect is present in the ^{51}V spectra displayed in Figure 6-2. The $LiNiVO_4$ spectrum is characterized by a relatively narrow central transition and a single set of

resolved first order quadrupole satellite transitions. The narrow central transition linewidth is expected from the diamagnetic nature of the unsubstituted compound. Although all vanadium ions are presumed to reside in tetrahedral sites, all of the other spectra show two nonequivalent V environments. As in the case of the ^{7}Li results, this reflects the different magnetic environments of ^{51}V nuclei as a function of Co^{2+} substitution. However, further details are required to explain the presence of two V sites in the "pure" Co compound as well as in the "pure" Ni compound, the latter of which also exhibits a small but broad feature to the left of one of the quadrupole satellites. The middle spectra in Figure 6-2 again highlight the difference between the SS and WS materials at the same composition, implying a random V-Co spatial distribution in the former vs. a non-random one in the latter.

The analysis of the XRD data confirms that all prepared samples have a spinel structure. In comparing the $LiCo_xNi_{1-x}VO_4$ NMR spectra prepared via the WCh with that of the SS, it is evident that each synthesis method produces distinct changes to the vanadium line. The SS spectrum contains very narrow lines and sharp peaks, which is indicative of the high degree in crystallinity of the samples prepared via the SS route, while the WCh spectrum consists of very broad lines and peaks. These two kinds of spectra contain an abundant amount of information regarding how the structural features of the vanadate compounds are affected by synthesis method.

The two-pulse solid echo responses were recorded as a function of pulse delay τ. The ^{51}V NMR spectra of SS and WCh samples are illustrated in Figure 6-3—Figure 6-7 and Figure 6-8--Figure 6-12, respectively. These spectra clearly show that V^{5+} ions reside in both octahedral and octahedral sites. This is somewhat consistent with

the XRD data[77] but deviate in the relative distribution of V^{5+} between tetrahedral and octahedral sites.

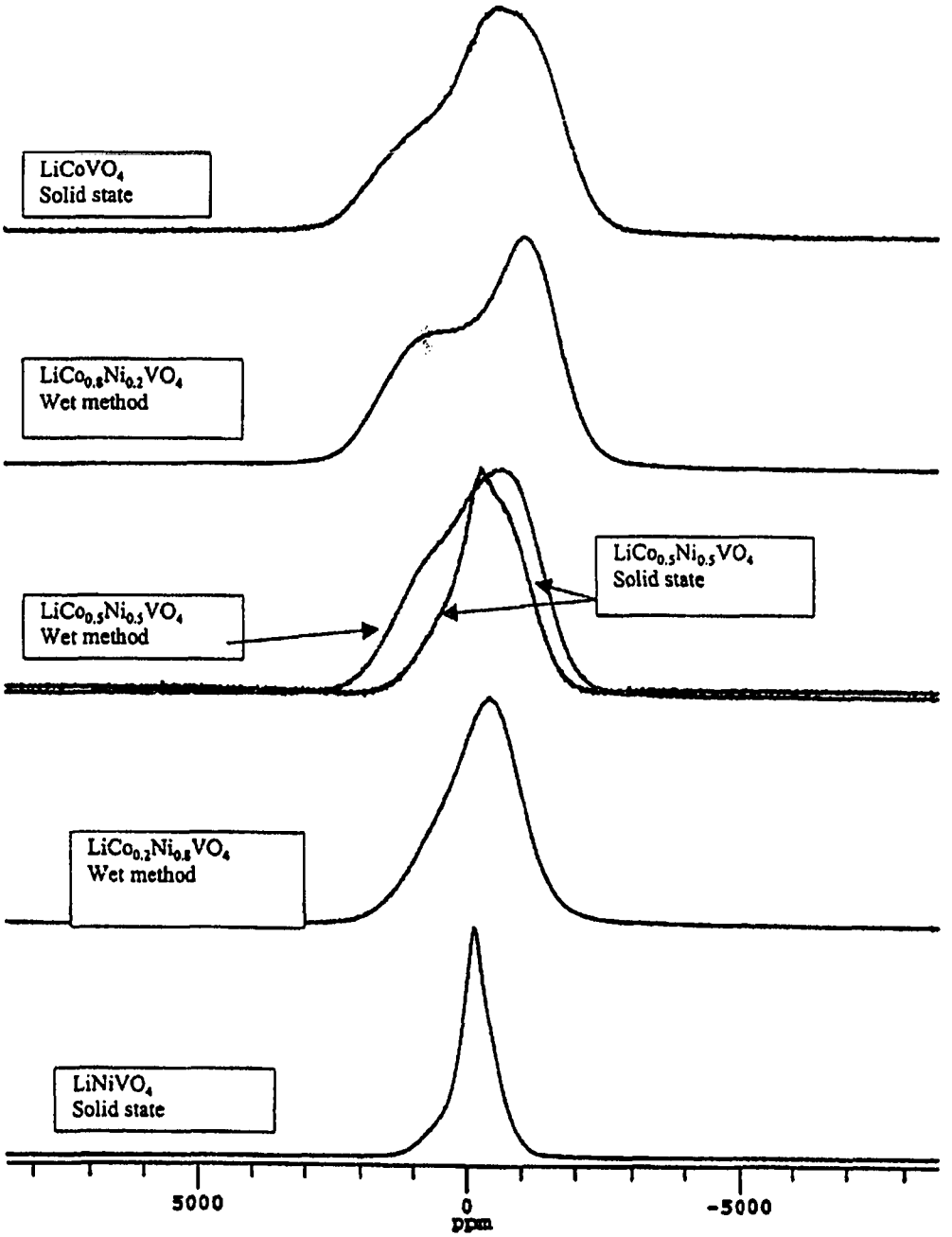

Figure 6-1 ^{7}Li NMR spectra of $LiCo_xNi_{1-x}VO4$(x =0,0.2,0.5,0.8,1).

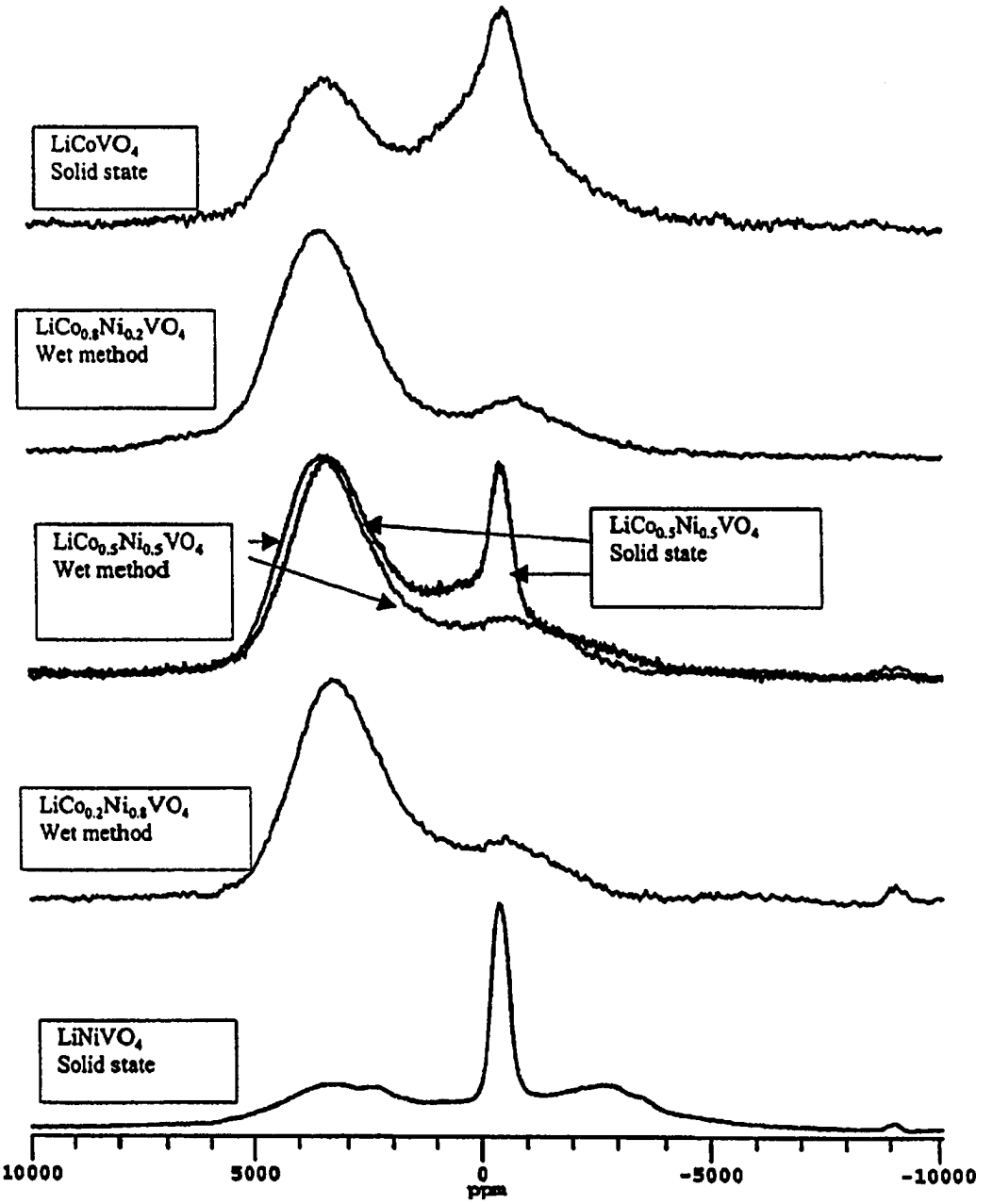

Figure 6-2 ^{51}V NMR spectra of $LiCo_xNi_{1-x}VO4$ (x =0,0.2,0.5,0.8,1).

The relative distribution of V^{5+} among tetrahedral and octahedral sites was derived by the deconvolution of the NMR spectra. Figure 6-13 gives a example of the deconvolution of the NMR spectra for $LiNiVO_4$ via SS route. The top curve is the experimental data. The simulated Gaussian tetrahedral site and the octahedral site (obtained by difference) are shown under the experimental data. The tetrahedral site shows large paramagnetic effects and the Gaussian type simulation is reasonable since the large broadening mechanism will smooth narrow features and obscure asymmetric features. It is noted that the octahedral site displays well resolved quadrupole features. Integrated intensities will give the weight of both sites when the total spectral intensities are normalized, assuming all the ^{51}V resonance were observable. The variable pulse delay spectra indicate the tetrahedral features have shorter T_2 than octahedral ones. Assuming that the ^{51}V resonance follows simple exponential decay and letting ${}^{tet}T_2 << {}^{oct}T_2$. After simple analysis, the fraction of tetrahedral site spectral intensity can be written as following,

$$I(\tau) = (1 + \beta e^{C\tau})^{-1} \qquad (6\text{-}1)$$

where, β and C are fitting parameters. In order to gather the intensity of the NMR line at τ = 0, spectral results must be fit with the above function as shown in Figure 6-14. The y intercept gives $I(0) = (1 + \beta)^{-1}$, which is the fraction of vanadium atoms at tetrahedral sites. From this, the fraction of vanadium atoms at the octahedral sites is determined as $\beta/(1+\beta)$. The parameter C is a measure of the relaxation rate difference between tetrahedral and octahedral sites and proportional to $(\frac{1}{{}^{tet}T_2} - \frac{1}{{}^{oct}T_2})$.

Figure 6-15 shows the fractional spectral intensity of the tetrahedral site vs. the compositional parameter, x, for both the NMR and XRD data. There are differences between the NMR data and the X-ray results with the largest discrepancies observed for low Co substitution in the WCh samples and the fully substituted Co sample in the SS materials.

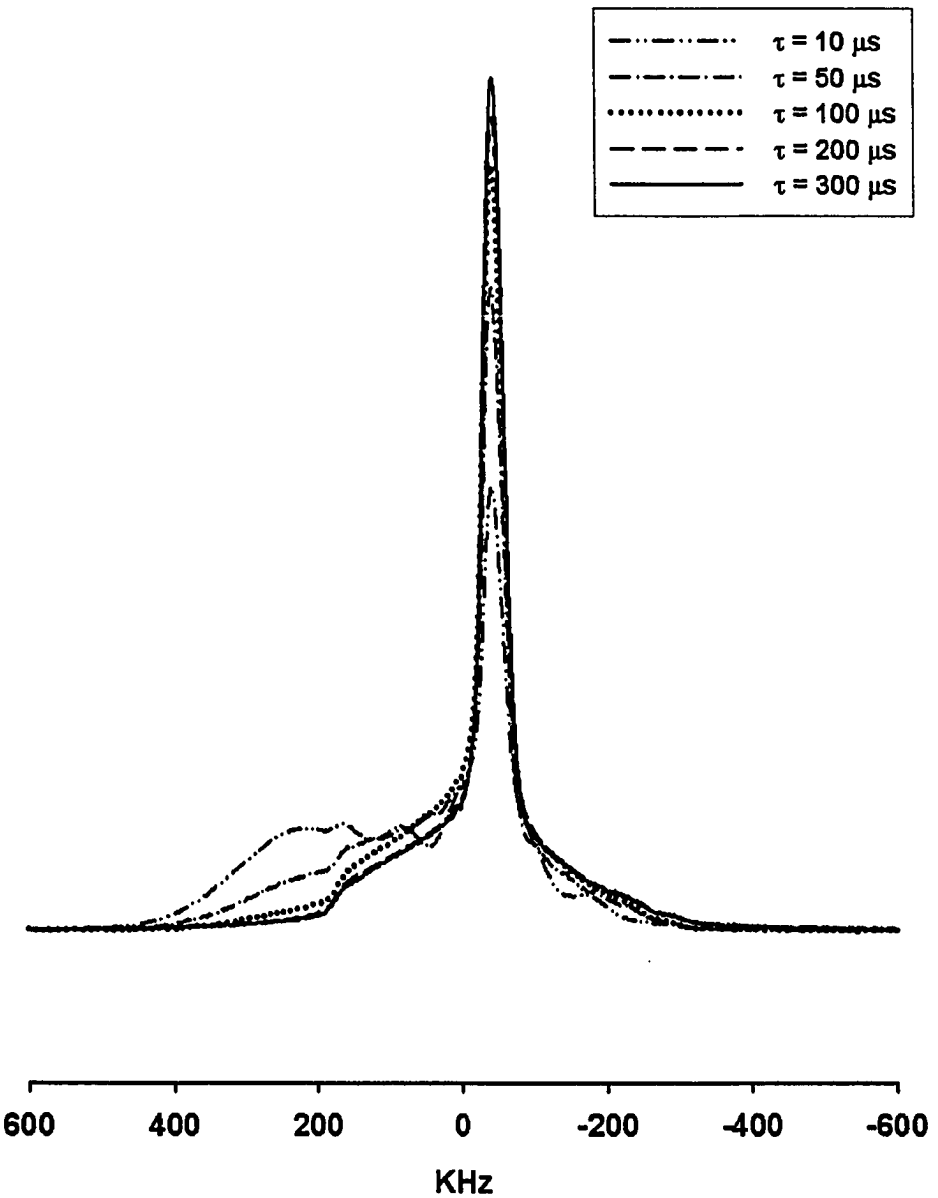

Figure 6-3 ^{51}V NMR spectra of $LiNiVO_4$ synthesized via solid-state route. These spectra were obtained with solid echo sequence with variable pulse separation τ.

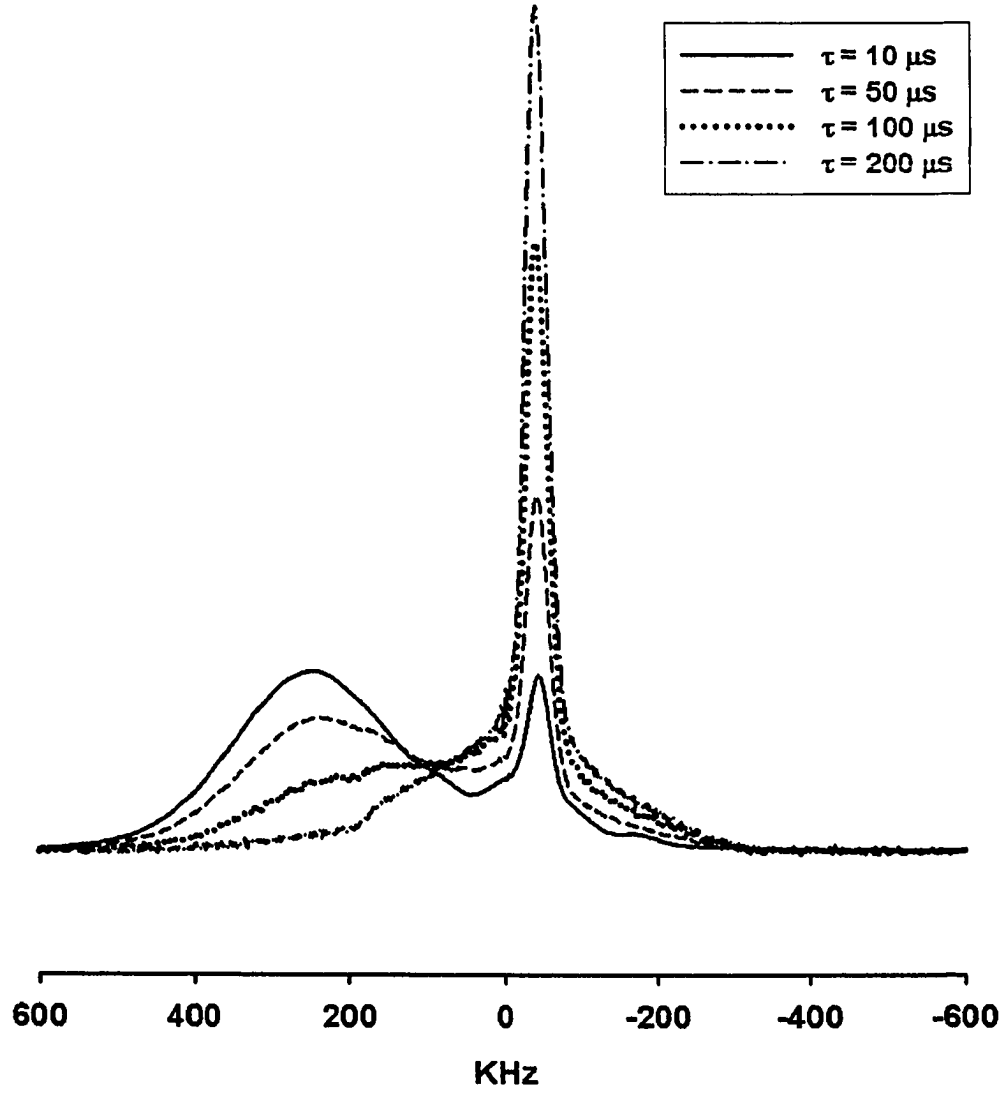

Figure 6-4 ^{51}V NMR spectra of $LiCo_{0.2}Ni_{0.8}VO_4$ synthesized via solid-state route. These spectra were obtained with solid echo sequence with variable pulse separation τ.

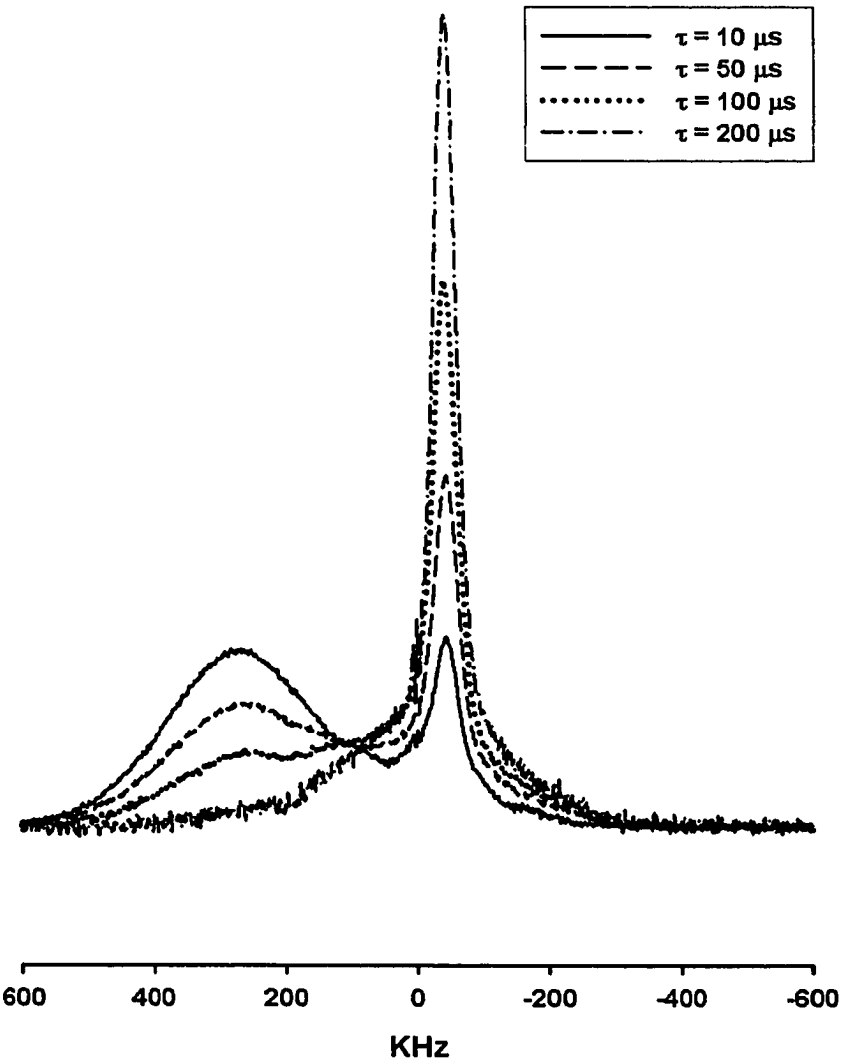

Figure 6-5 ^{51}V NMR spectra of $LiCo_{0.5}Ni_{0.5}VO_4$ synthesized via solid-state route. These spectra were obtained with solid echo sequence with variable pulse separation τ.

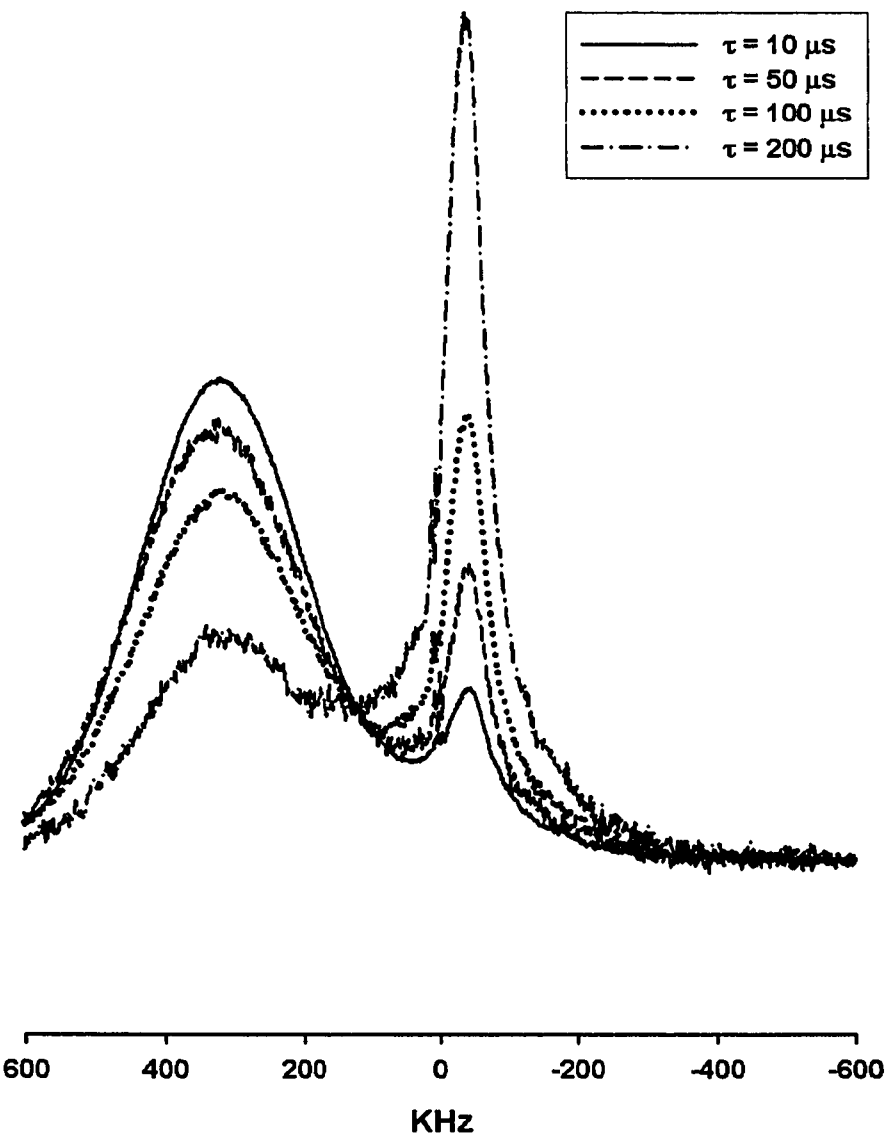

Figure 6-6 ^{51}V NMR spectra of $LiCo_{0.8}Ni_{0.2}VO_4$ synthesized via solid-state route. These spectra were obtained with solid echo sequence with variable pulse separation τ.

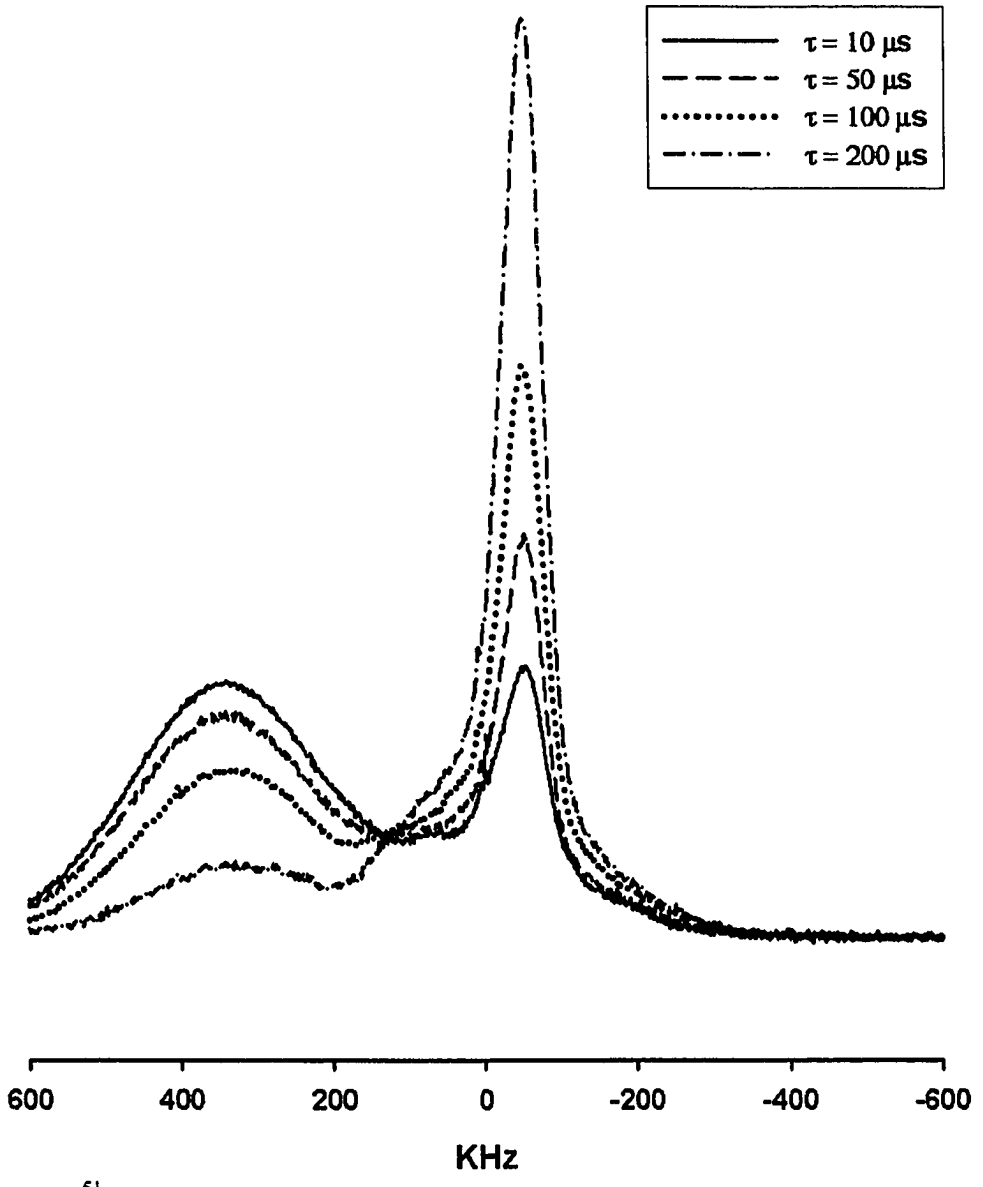

Figure 6-7 ^{51}V NMR spectra of $LiCoVO_4$ synthesized via solid-state route. These spectra were obtained with solid echo sequence with variable pulse separation τ.

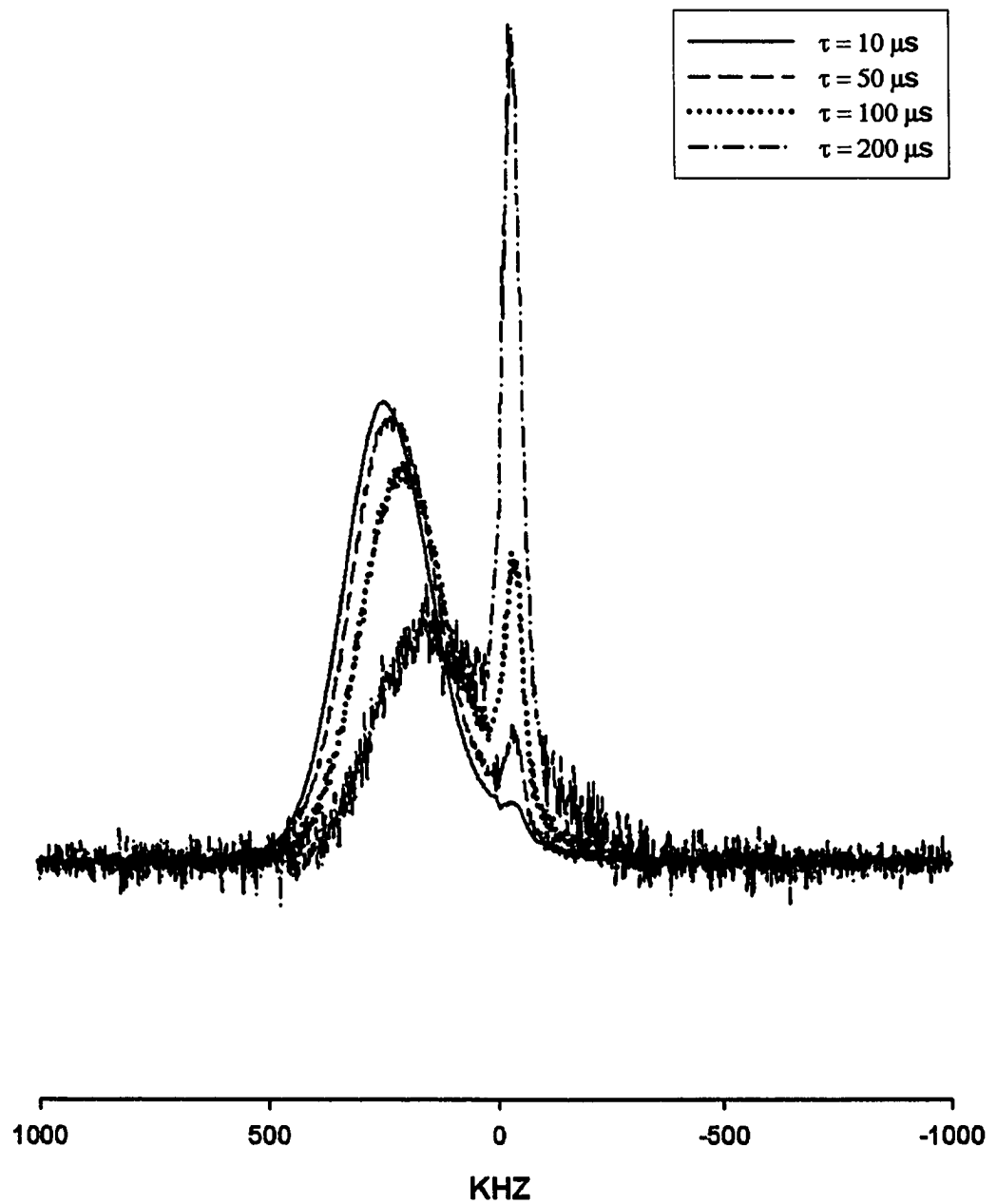

Figure 6-8 ^{51}V NMR spectra of $LiNiVO_4$ synthesized via wet-chemistry route. These spectra were obtained with solid echo sequence with variable pulse separation τ.

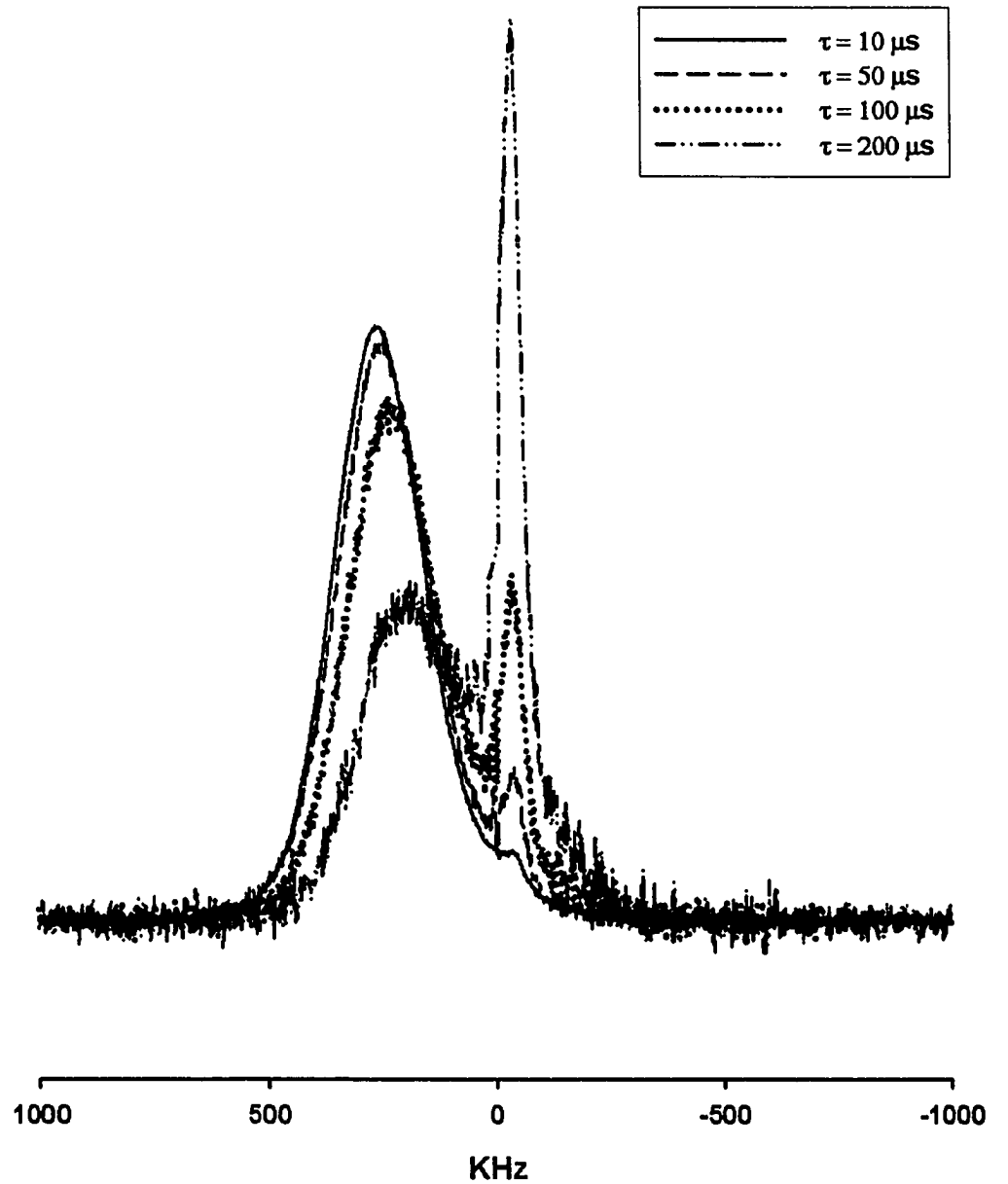

Figure 6-9 ^{51}V NMR spectra of $LiCo_{0.2}Ni_{0.8}VO_4$ synthesized via wet-chemistry route. These spectra were obtained with solid echo sequence with variable pulse separation τ.

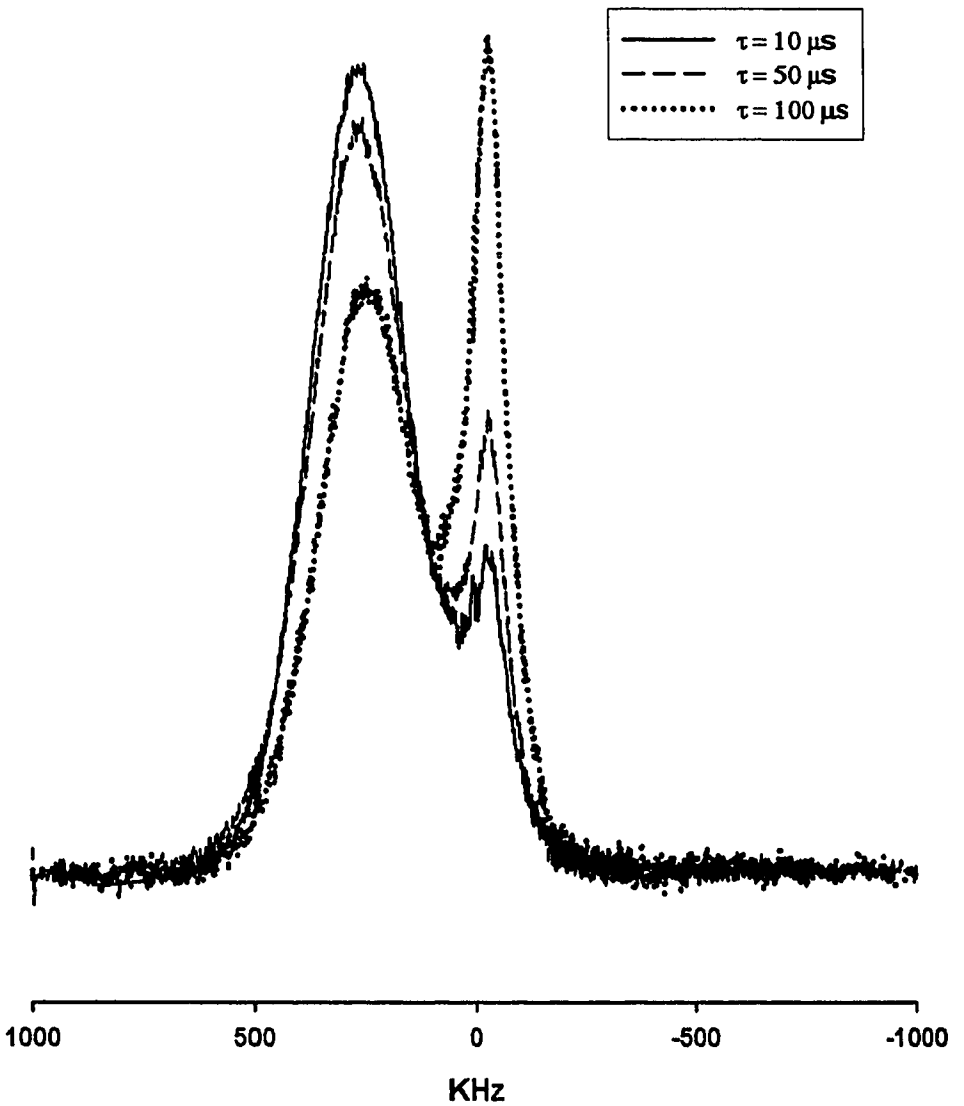

Figure 6-10 ^{51}V NMR spectra of $LiCo_{0.5}Ni_{0.2}VO_4$ synthesized via wet-chemistry route. These spectra were obtained with solid echo sequence with variable pulse separation τ.

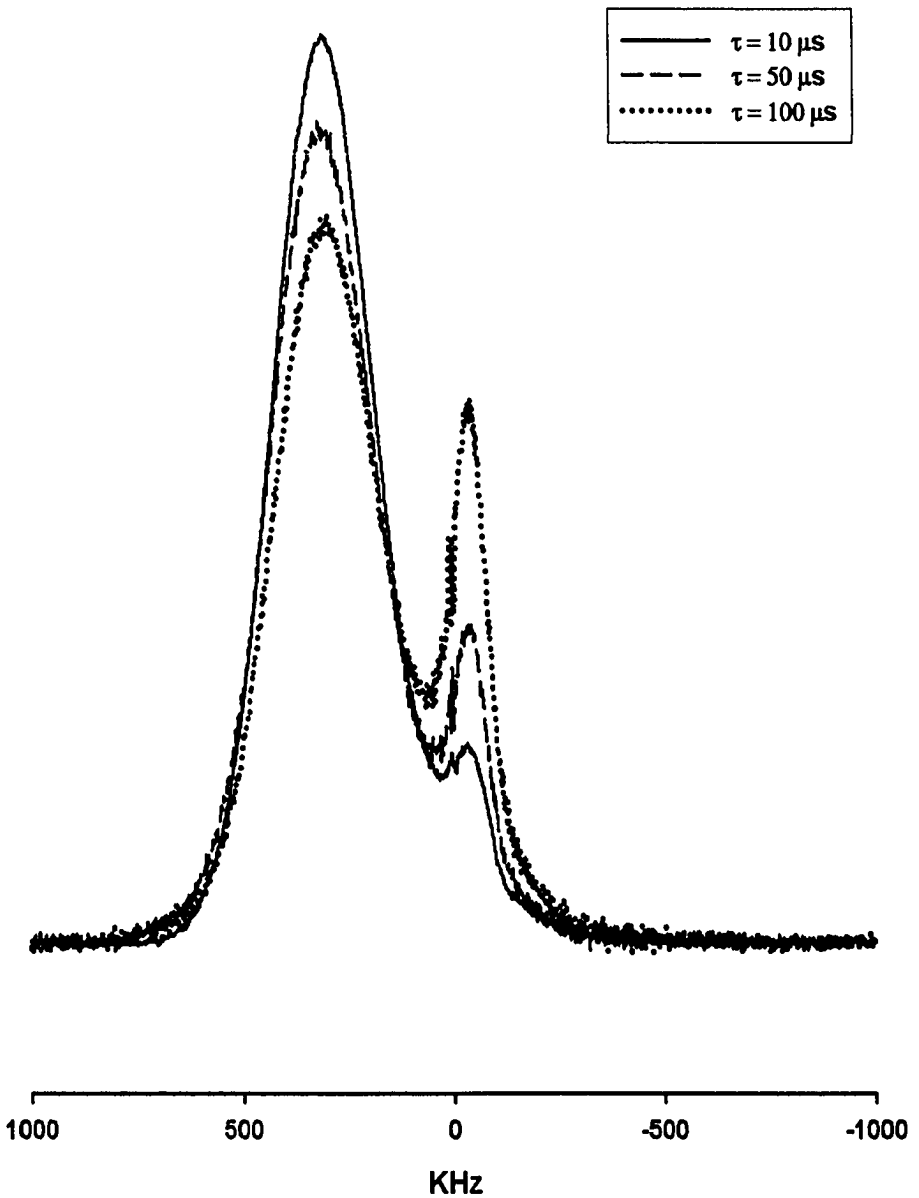

Figure 6-11 ^{51}V NMR spectra of $LiCo_{0.8}Ni_{0.2}VO_4$ synthesized via wet-chemistry route. These spectra were obtained with solid echo sequence with variable pulse separation τ.

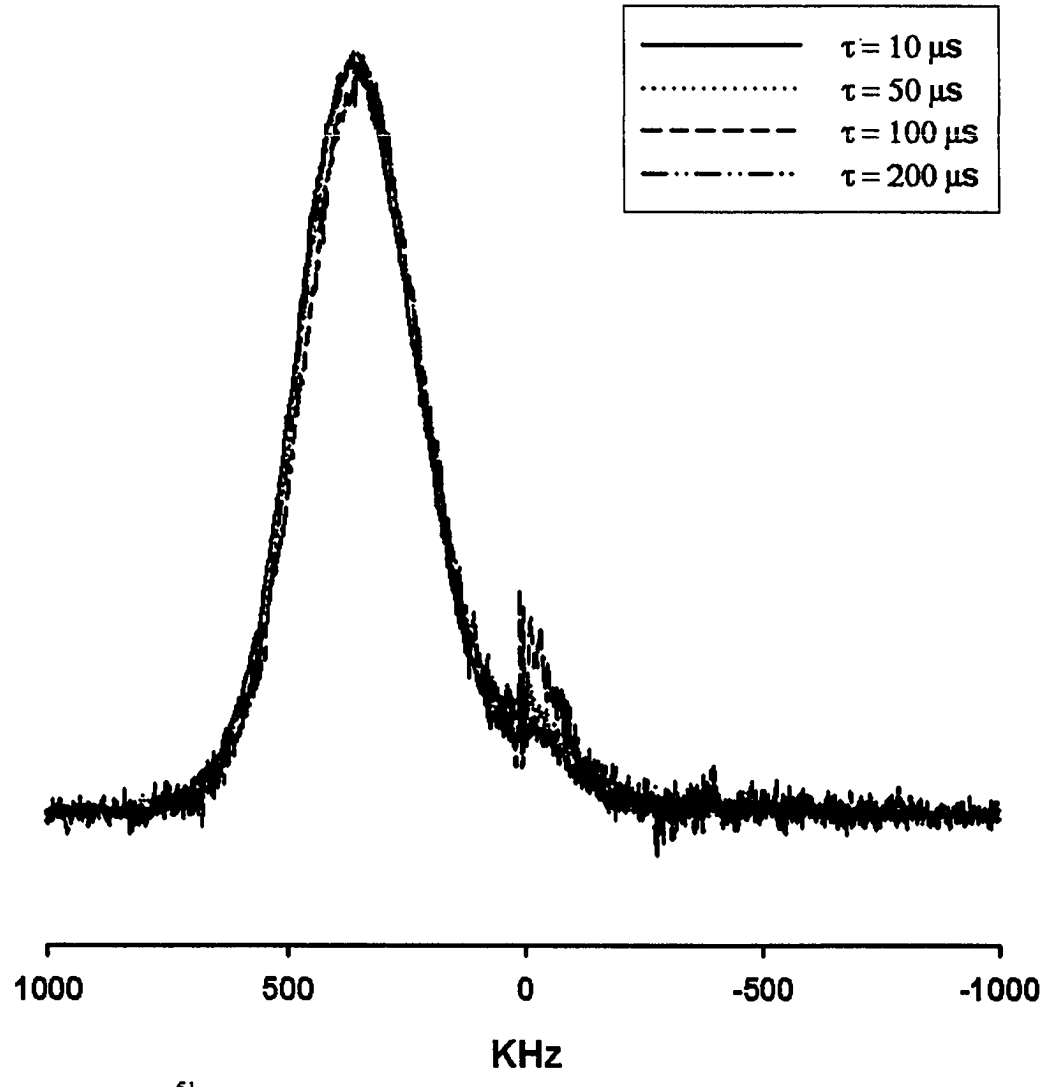

Figure 6-12 ^{51}V NMR spectra of $LiCoVO_4$ synthesized via wet-chemistry route. These spectra were obtained with solid echo sequence with variable pulse separation τ.

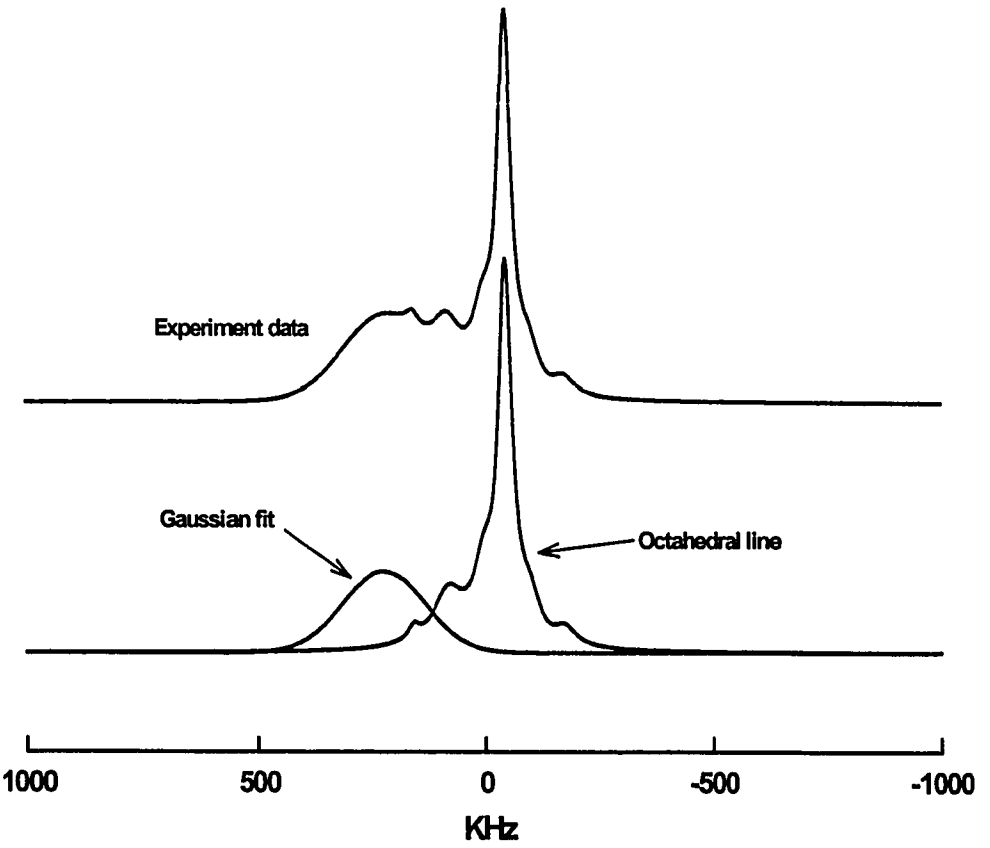

Figure 6-13 Simulation of ^{51}V NMR spectrum of $LiNiVO_4$ synthesized via solid-state route. The tetrahedral site was fitted by Gaussian peak; the octahedral site is derived by the difference.

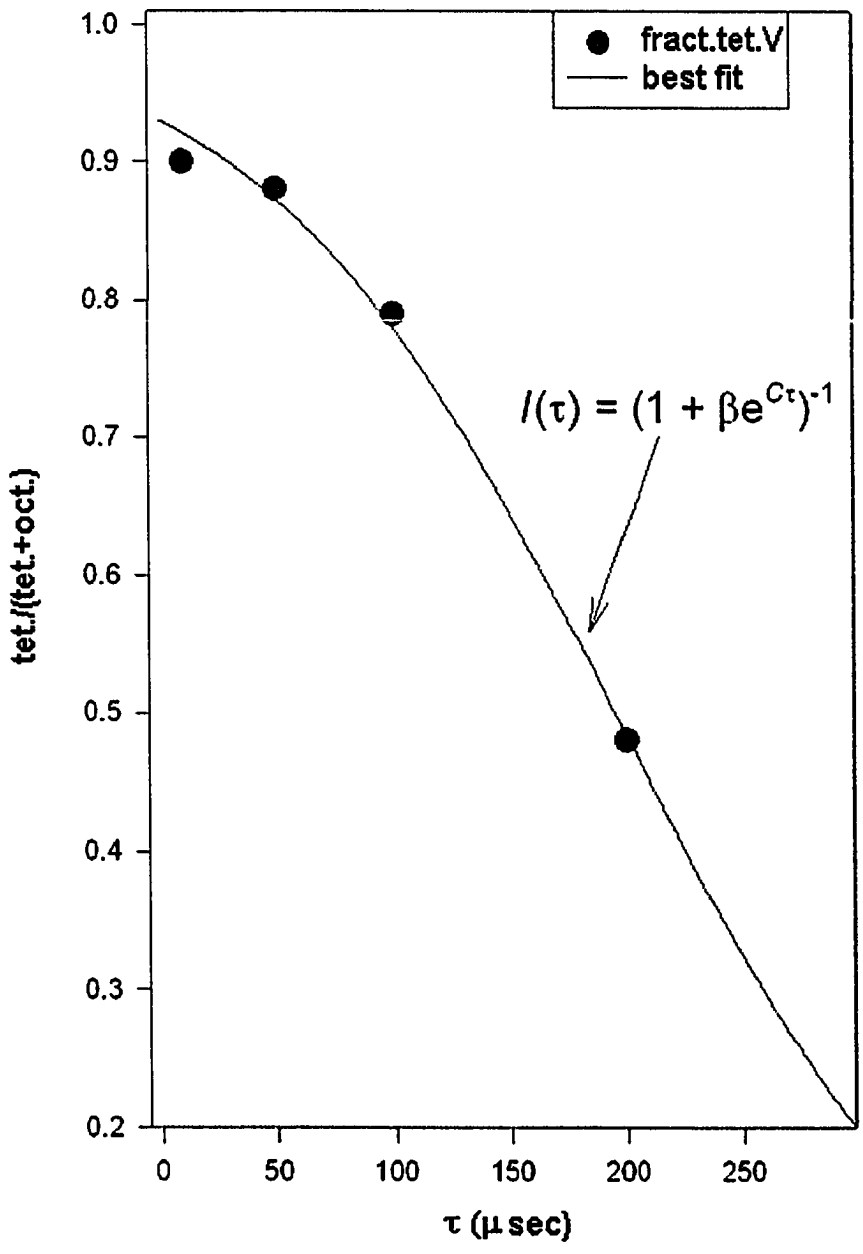

Figure 6-14 The fractional spectral intensity versus pulse separation (τ) of solid echo sequence.

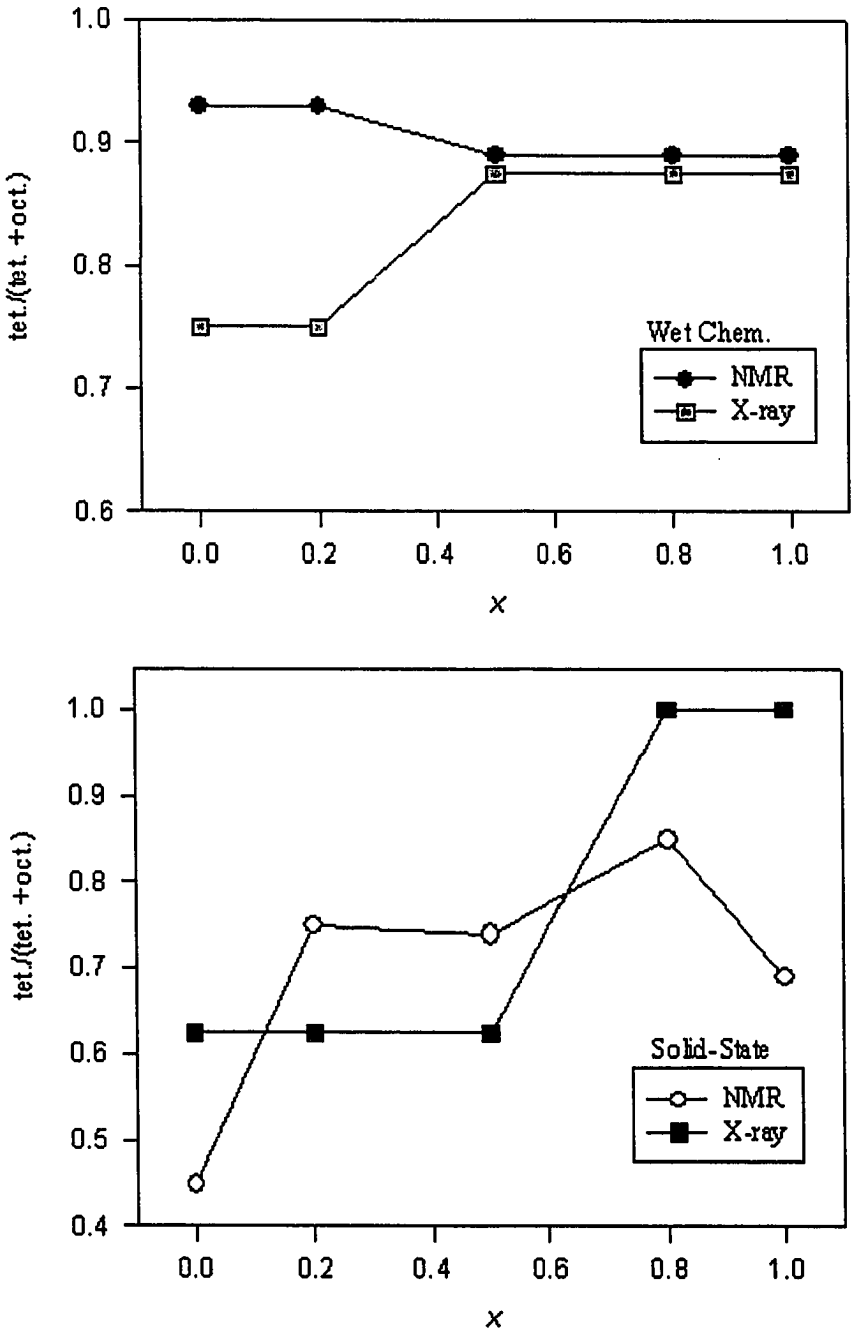

Figure 6-15 The fractional spectral intensity of the tetrahedral site versus compositional parameter (x) of $LiCo_xNi_{1-x}VO_4$ for both NMR and XRPD data.

^{7}Li quadrupole echo spectra with variable pulse separation τ of SS and WCh samples are shown in Figure 6-16 and Figure 6-17, respectively. ^{7}Li NMR indicates that at least two types of lithium sites for $LiCo_xNi_{1-x}VO_4$ materials. It is speculated that the Gaussian-fit line in Figure 6-18 is a tetrahedral lithium site compensating for the extra octahedral V sites encountered in some samples. The octahedral response is simulated by CSA (chemical shift anisotropy) and magnetic dipolar interactions. Based on the CSA simulation, the octahedral site indicates axial distortion. The larger distributions observed in wet-chemistry samples are due to enhanced magnetic interaction between lithium and cobalt.

The fact that the Gaussian feature of the ^{7}Li NMR spectra relax faster than the octahedral feature strongly implies a special correlation with cobalt which allows a model of the system to be created along these lines.

^{7}Li NMR spectra demonstrate that $LiCo_xNi_{1-x}VO_4$ samples prepared through the WCh route which involves dissolving of the precursor compounds initially, yield a less disordered system than those prepared through SS route.

The inverse spinel structure requires that in $LiCo_xNi_{1-x}VO_4$, the total number of octahedral sites of lithium, cobalt, nickel and vanadium should add up to 2. The tetrahedral sites of these four elements must add up to 1. These relationships are modeled by equations 6-2 and 6-3.

$$V_{oct} + Li_{oct} + (Ni/Co)_{oct} = 2 \qquad 6\text{-}2$$

$$V_{tet} + Li_{tet} + (Ni/Co)_{tet} = 1 \qquad 6\text{-}3$$

Like the treatment of ^{51}V NMR spectra, the relative distribution of Li^+ sites was also derived by deconvoluting the ^7Li NMR spectra as shown in Figure 6-18. The fractional spectral intensity of the tetrahedral site vs. the compositional parameter, x, for the SS samples is shown in Figure 6-19. No attempts were made to figure out the fractional spectral intensity for wet-chemistry route samples as there was little effect on the ^7Li NMR spectra when the variable pulse separation excitation sequence was applied to these samples. Figure 6-19 shows that, for x = 0.2, 0.67 of the ^7Li spectrum is octahedral while 0.33 is speculated to be tetrahedral. Figure 6-15 shows that 0.75 of the original ^{51}V spectrum is tetrahedral while 0.25 is octahedral. When these value are inserted into equation 6-3, a value greater than 1 is obtained. This shows deviations from the ideal spinel structure cited in reference [77].

It was observed in reference [77] that as greater amount of cobalt were substituted, CSA was initially large, then immediately decreased followed by a rapid increase. Materials prepared through WCh showed smaller CSA than materials prepared through SS. Data presented here reflected entirely contradictory conclusions. The reason for this is not known.

Based on electrochemical data acquired and previous studies[78], the WCh sample $LiCo_{0.2}Ni_{0.8}VO_4$ displayed that the electrochemical lithium insertion-deinsertion process occurs reversibly in the 4.3-4.4 V range vs Li/Li^+. The solid-state sample $LiNiVO_4$ shows considerably lower electrochemical performance, especially regarding reversibility of this electrode.

6.4 Conclusions

Both ^{51}V and ^{7}Li NMR studies were applied for a series of $LiCo_xNi_{1-x}VO_4$ (x = 0, 0.2, 0.5, 0.8, 1) prepared by two different methods, solid-state and wet-chemistry routes. Two magnetically nonequivalent sites of V^{5+} can be observed from the ^{51}V NMR spectra, indicating the deviation from the ideal inverse spinel structure. The relative amount of V^{5+} ions at tetrahedral and octahedral sites can be derived from the integration of the NMR spectra because the resonance signal is proportional to the number of resonant NMR nuclei in the sample. ^{7}Li NMR spectra also indicate distribution of Li^{+} between tetrahedral and octahedral sites. An analysis of the data suggests that wet-chemistry samples are less disordered than those synthesized via solid-state method; the site distributions are virtually independent of x for materials fabricated via wet-chemistry. NMR provides a more complete picture of distributions of cations as compared to x-ray diffraction. The most important conjecture made here is that, as suggested in reference [78], the difference observed in Li intercalation-deintercalation capacity is a consequence of the route of preparation rather than the compositional difference.

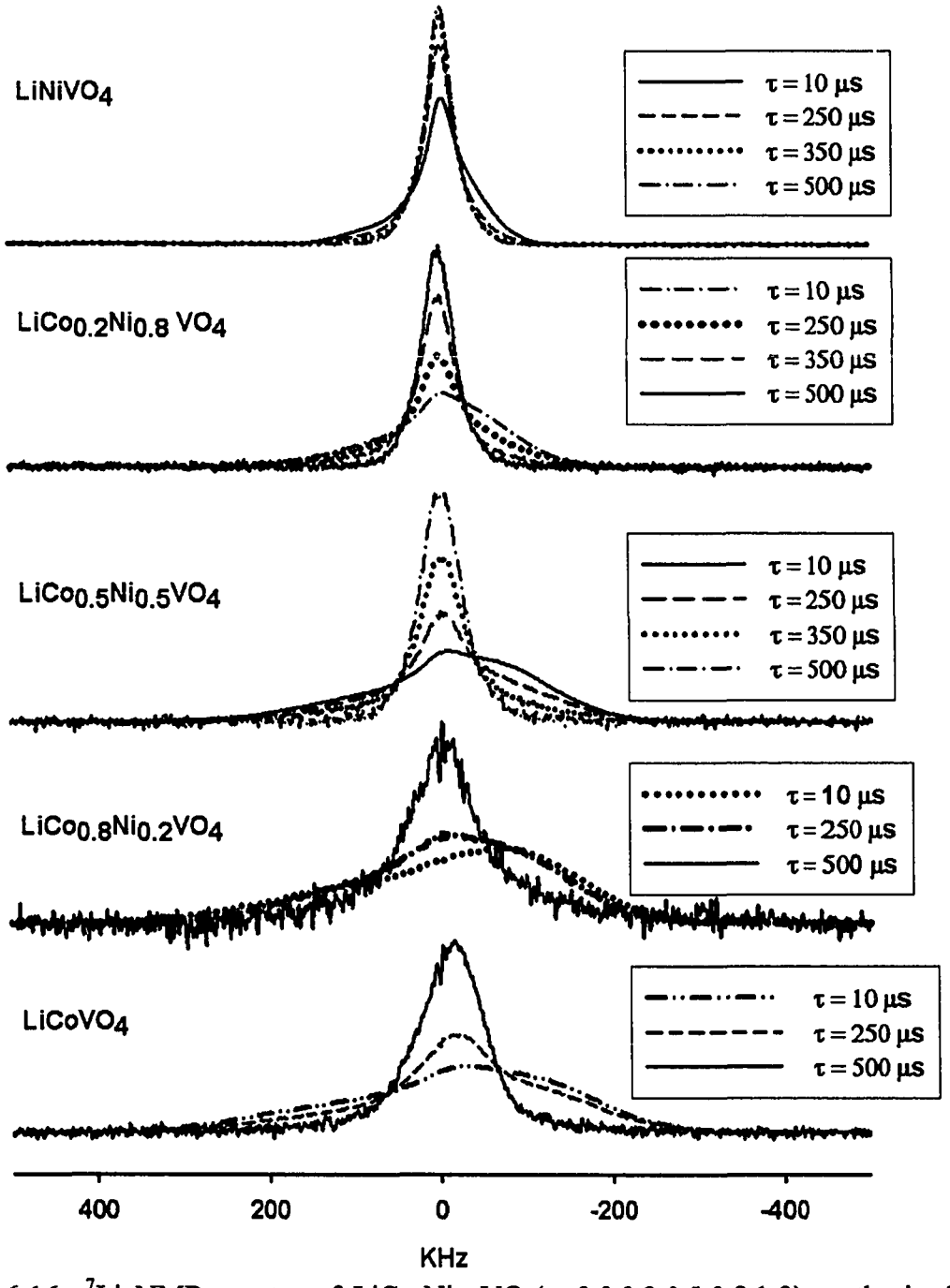

Figure 6-16 ^{7}Li NMR spectra of $LiCo_xNi_{1-x}VO_4$(x=0.0,0.2,0.5,0.8,1.0) synthesized via solid-state route. These spectra were obtained with solid echo sequence with variable pulse separation τ.

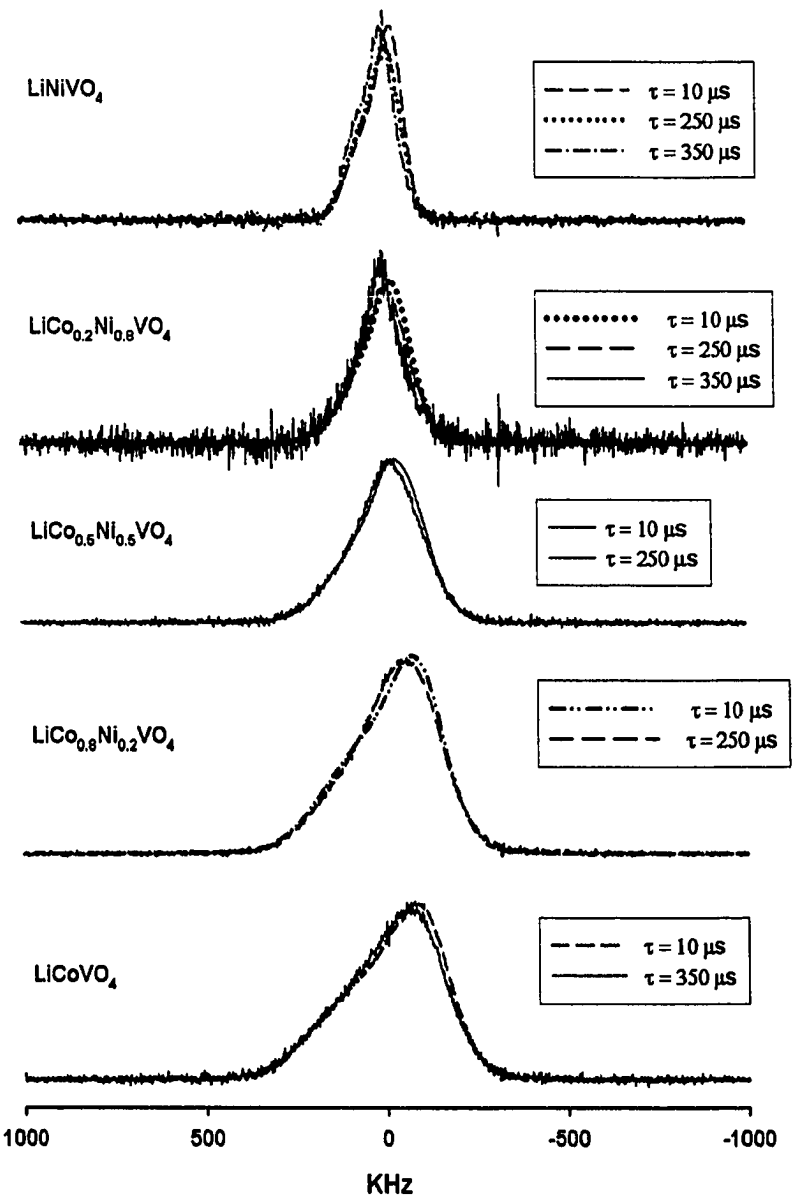

Figure 6-17 ^{7}Li NMR spectra of $LiCo_xNi_{1-x}VO_4$(x=0.0,0.2,0.5,0.8,1.0) synthesized via wet-chemistry route. These spectra were obtained with solid echo sequence with variable pulse separation τ.

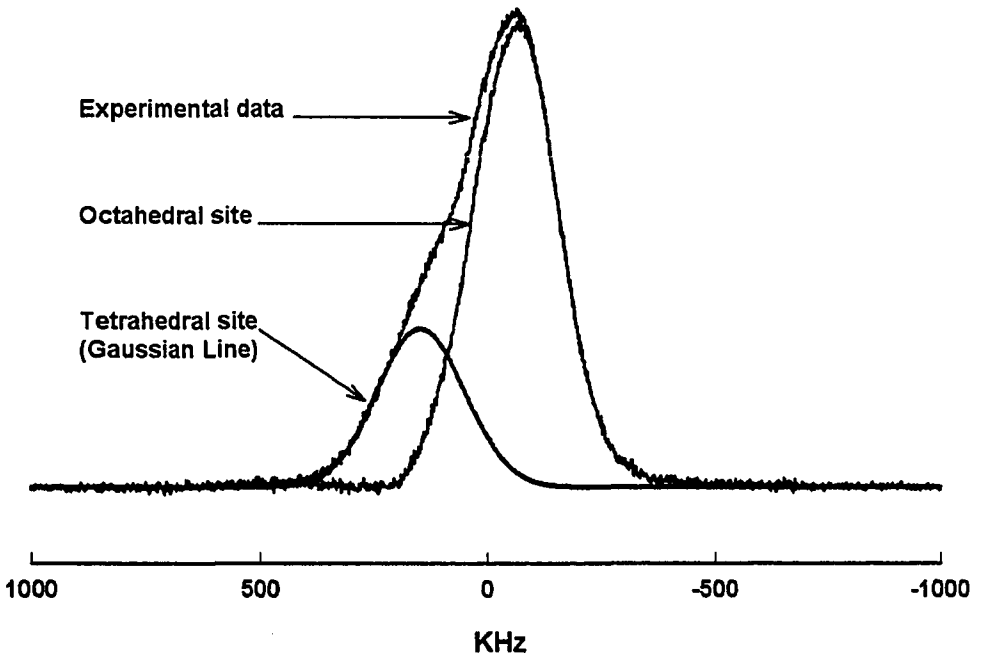

Figure 6-18 Simulation of ^{7}Li NMR spectrum of $LiCo_{0.8}Ni_{0.2}VO_4$ synthesized by solid-state route. The tetrahedral site was fitted by Gaussian peak; the octahedral site was derived by the difference.

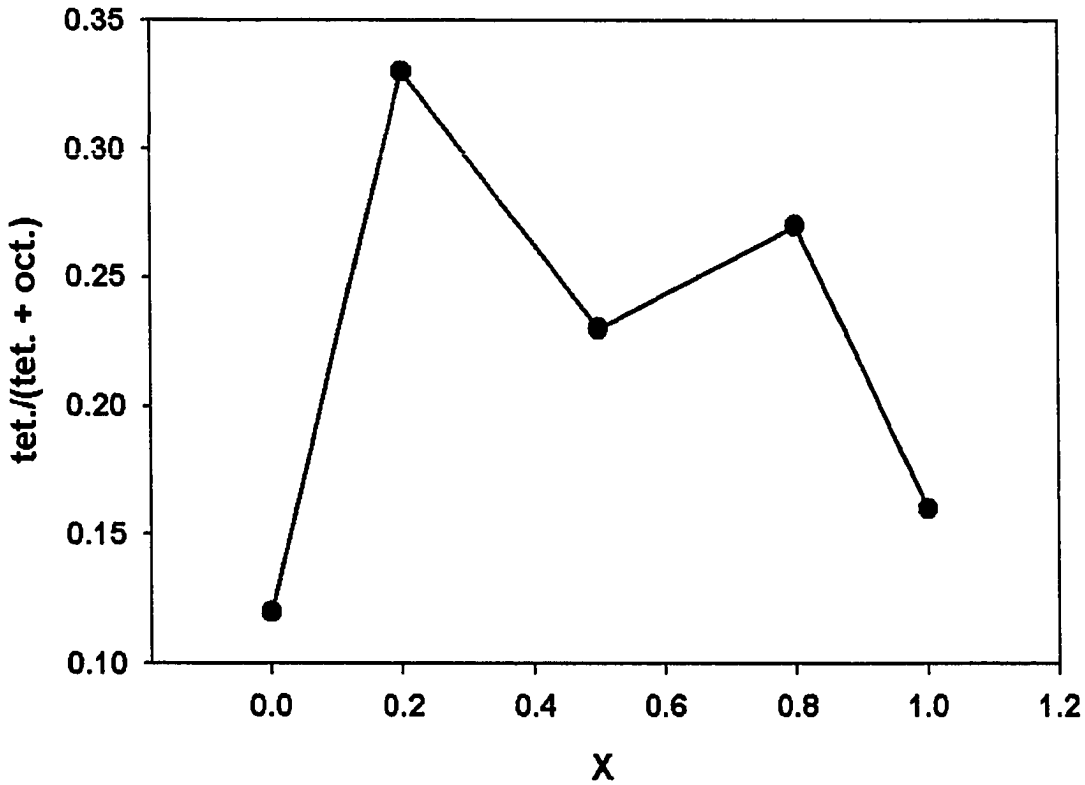

Figure 6-19 The fractional spectral intensity of the tetrahedral site versus compositional parameter (x) of solid-state route $LiCo_xNi_{1-x}VO_4$ for ^7Li NMR data.

CHAPTER 7

Conclusions

The full potential of portable devices remains limited by battery performance; while the enhancement in battery performance is limited by available materials. Current battery technology is still far from the physical and electrochemical materials limits and there is much room for improvement. X-ray powder diffraction techniques, while still very important in structural studies of battery materials, lack information about short-range order and the scatter factor of Li is small. In contrast, NMR is a powerful tool for probing the immediate environments of ions such as Li^+ in the solid state, especially in disordered materials.

In this dissertation, selected electrode materials have been studied by solid state pulse NMR spectroscopy. These materials involve layered structure pristine and partially oxidized lithiated graphite, transition metal cation (Fe,Co) substituted lithium nickelate and mixed inverse spinel structure $LiCo_xNi_{1-x}VO_4$. The experimental results prove that the NMR spectrum is sensitive to local atomic and electronic structure. NMR is nuclear-specific and can be used to directly examine the species that are involved in the working battery. As a probe of the immediate environment of the nucleus under investigation, NMR demonstrates an ideal method for investigating the small change in local structure that occur on doping and for illustrating lithium insertion-extraction mechanisms. Furthermore, the integrated spectroscopic signal is

proportional to the number of resonant NMR nuclei in the sample. Thus, NMR analysis can be used to ascertain the relative phase content of a material in cases where individual spectral contribution can be resolved. For example, the SEI content on the positive electrode surface and the distribution of Li^{+} and V^{5+} between tetrahedral and octahedral sites have been directly derived from the NMR spectra.

References

1. M.Armand, Materials for Advanced Batteries, D.W.Murphy, J.Broodhead, and B.C.H. Steele, Editors, p145, Plenum Press, New York (1980).

2. F.Bonino, M.Lazzari, L.Peraldo Bicelli, B. Di Pietro, and B.Scrosàti, in Lithium Batteries, H.V.Venkatasetty, Editor, The Electrocchemical Society Softbound Proceedings Series, Pennington, NJ (1981).

3. T.Nagaura and K.Tazawa, Prog. Batteries Sol.Cell, 9 (1990) 20 .

4. Lithium Batteries-New Materials, Developments and Perspectives, G.Pistoia, Editor, p.1, Elsevier, Amsterdam (1994).

5. J.R.Dahn, R.Fong and M.J. Spoon, Phys.Rev., B. 42 (1990) 6424.

6. R.Fong, V.Von Saken, and J.R.Dahn, J. Electrochem. Soc., 137 (1990) 2007 .

7. N.Imanishi, S.Ohashi, T.Ichikawa, Y.Takeda, O.Yamamoto and R.Kanno, J.Power Sources, 39 (1992) 185 .

8. H.Imoto, A.Omaru, H.Azuma and Y.NiShi in Proc. Lithium Batteries, Electrochem. Soc., 93 (1993) 9.

9. Kenji Sato, Minoru Noguchi, Atsushi Demachi, Naohiko Oki, Morinobu Endo, Science, 264 (1994) 22.

10. J.R.Dahn, T.Zhang, Y.liu, J.S.Xue,Science, 270 (1995) 590.

11. Bruno Scrosati, Electrochimica Acta , 45 (2000) 2461-2466.

12. I.I.Rabi, S.Millman,P.Kusch and J.R.Zacharias Phys.Rev., 55 (1939) 526.

13. Purcell, Torrey, Pound, Physical Rev., 69 (1946) 37 .

14. Bloch, Hansen, Packard, Physical Rev., 69 (1946) 127 .

15. A.Abragam, The Principles of Nuclear Magnetism, Oxford University Press, 1961.

16. C.P. Slichter, The Principles of Magnetic Resonance, Harper and Row, New York, 1978.

17. Brian Cowan, Nuclear Magnetic Resonance and Relaxation, Cambridge

University Press, 1997.

18. R.K.Harris, Nuclear Magnetic Resonance Spectroscopy: A Physicochemical View, Pitman, London, 1983.

19. E.Fukushima and S.B.Roeder, Experimental Pulse NMR, A Nuts and Bolts Approach, Addison-Wesley, Massachusetts, 1981.

20. H.Y.Carr and E.M.Purcell, Phys.Rev., 94 (1954) 630-638 .

21. J.G.Powles and J.H.Strange, Proc.Phys.Soc., (London) 82 (1963) 6-15 .

22. E.R.Andrew, Prog.NMR Spectroscope, 8 (1971) 1-39.

23. M.S.Dresselhaus, G.Dresselhaus, Adv.Phys., 30 (1981) 139.

24. J.Conard and H.Estrade, Mater.Sci.Eng., 31 (1977) 173.

25. Y.Matsumura, S.Wang, J.Mondori, Carbon, 33 (1995) 1457.

26. K. Tatsumi, T.Akai, T.Imamura, K.Zaghib, Y.Sawada, J.Electrochem.Soc., 143 (1996) 1923.

27. N.Imanishi,K.Kumai,H.Kokugan,Y.Takeda, and O.Yamamoto, Solid State Ionics, 107 (1998) 135 .

28. K.Zaghib,K.Tatsumi,Y.Sawada,S.Higuchi,H.Abe,andT.Ohsaki, J.Electrochem.Soc., 146 (1999) 2784

29. E.Peled, C.Menachem, D.Bar-Tow, A.Melman, J.Electrochem.Soc. ,143 (1996) L4.

30. C.Menachem, Y.Wang, J.Flowers, E.Peled, S.G.Greenbaum, J.Power Sources, 76 (1998) 180.

31. G.Ardel, D.Goldnitsky, E.Strauss, Epeled, Proceedings of the 37th Power Sources Conference (ARL), 283(1996).

32. J.Conard and H.Estrade, Mater.Sci.Eng., 31 (1977) 173.

33. K.Amine and J.Liu, ITE Lett., 1 (2000) 59.

34. K.Amine, M.J.Hammond, J.Liu, C.Chen, D.W.Dees, A.N.Jansen, and G.L.Henriksen, Abstract 332, The 10th International Meeting on Lithium Batteries, Como, Italy, May 28-June 2, 2000

35. E.Peled, J.Electrochem.Soc., 126 (1979) 2047.

36. D.Aurthbach, I.Weissman,A.Zaban, and O.Chuzid (Youngman), Electrochim.Acta, 39 (1994) 51

37. G.Ardel,D.Golodnitsky, and E.Peled, J.Electrochem.Soc.,144 (1997) L208.

38. M.C.Smart, B.V.Ratnakumar, Y.Wang, X.Zhang, S.G.Greenbaum, S.Surampudi, A.Hightower,C.Ahn, and B.Fultz, J.Electrochem.Soc., 146 (1999) 3963.

39. J.Liu, C.H.Chen, J.S.Luo, G.L.Henriksen, and K.Amine, Abstract 185, The Electrochemical Meeting Abstracts, Vol. 2000-2, Phoenix, AZ, Oct 22-27, 2000.

40. M.Menetrier, A.Rougier, and C.Delmas, Solid State Commun., 90 (1994) 439.

41. T.Ohzuku and A.Ueda, Solid State Ionics, 69 (1994) 201.

42. I.Saadoune and C.Delmas, J.Mater.Chem., 6 (1996) 193.

43. E.Rossen, C.D.W.Jones and J.R.Dahn, Solid State Ionics, 57 (1992) 311.

44. J.N.Reimers, E.Rossen, C.D.Jones and J.R.Dahn, Solid State Ionics, 61 (1993) 335.

45. G.Prado, A.Rougier, L.Fournes and C.Delmas, J.Electrochem.Soc., 147 (2000) 2880.

46. C.Marichal, J.Hirschinger, P.Granger, M.Menetrier, A.Rougier and C.Delmas, Inorg.Chem., 34 (1995) 1773.

47. P.Ganguly, V.Ramaswamy, I.S.Mulla, R.F.Shinde, P.P.Bakare, S.Ganapathy, P.R.Rajamohanan, and N.V.K. Prakash, Phys.Review B, Vol.46, 18 (1992) 11595.

48. R.D.Shannon, Acta Crystallogar. A 32, (1976) 751.

49. C.A. Vincent and B.Scrosati, Modern Batteries, E.Arnold Ed., London (1997).

50. J.B. Goodenough, A.Manthiram and B.Wnetrzewski, J.Power Sources, 43-44 (1993) 269.

51. M.M.Thackery, J.Electrochem.Soc., 142, 8 (1995) 2558.

52. T.Ohzuku, A.Ueda and M.Nagayama, J.Electrochem.Soc. , 140 No.7 (1993)

1862.

53. J.R.Dahn, U.von Sacken and C.Michal , Solid State Ionics, 44 (1990) 87.

54. J.B.Goodenough, D.G. Wickham and W.J.Groft, J.Appl.Phys. 29 (1958) 382.

55. H.Arai, S.Okada, H.Ohtsuka, M.Ichimura and J. Yamaki, Solid State Ionics, 80 (1995) 261.

56. A.Rougier, P.Gravereau and C.Delmas, J.Electrochem. Soc., 143, 4 (1996) 1168.

57. W.Liu,G.C.Farrington, F.Chaput and B.Dunn, J.Electrochem. Soc., 143, 3 (1996) 879.

58. A.Rougier, I.Saadoune, P.Gravereau, P.Willmann and C.Delmas, Solid State Ionics, 90 (1996) 83.

59. E.Zhecheva and R.Stoyanova, Solid State Ionics, 66 (1993) 143.

60. T.Ohzuku, A.Ueda, M.Nagayama, Y.Iwakoshi and H.Komori, Eletrochimica Acta, 38 (1993) 1159.

61. A.Ueda and T.Ohzuku, J.Electrochem.Soc., 141, 8 (1994) 2010.

62. J.Molenda, P.Wilk and J.Marzec, Solid State Ionics, 119 (1999) 19.

63. Y.J.Lee, F.Wang and C.P.Grey, J.Am.Chem.Soc.,120(1998)10601.

64. Y.J.Lee and C.P.Grey, Chem.Mater., 12 (2000) 3871 .

65. P.E.Stallworth, S.Kostov, M.L.denBoer, S.G.Greenbaum and C.Lampe-Onnerud, J.Appl.Phys., 83 (1998) 1247.

66. C.Julien, Ionics, 6 (2000) 30.

67. R.Alcàntara, P.Lavela, J.L.Tirado, R.Stoyanova, E.Kuzmanova and E.Zhecheva, Chem.Mater., 9 (1997) 2145.

68. F.Ronci, Degree Thesis, Dipartimento di Chimica, Università " La Sapienza", Rome, Italy.

69. B.Scrosati, Nature, 373 (1995) 557.

70. S.Megahed, B.Scrosati, J.Power Sources, 51 (1994) 79.

71. S.Megahed, B.Scrosati, Interface, 4 (1995) 34

72. J.M.Tarascon, W.R.McKinnon, F.Coowar, T.N.Bowmer, G.Amatucci, D.Guyomard, J.Electrochem.Soc., 141 (1994) 1421.

73. G.T.K. Fey, K.S.Wang, S.M.Wang, J. Power Sources, 68 (1997) 159.

74. G.T.K. Fey, D.L.Huang, Electrochim, Acta , 45 (1999) 295.

75. S.Panero, P.Reale, F.Bonino, B.Scrosati, M.Arrabito, S.Bodoardo, D.Mazza, N.Penazzi, Solid State Ionics, 128 (2000) 43.

76. G.T.K.Fey, W.Li, J.R.Dahn, J.Electrrochem.Soc., 141 (1994) 2279.

77. Peter P.Chu, D.L.Huang, G.T.K.Fey, J.Power Sources, 90 (2000) 95.

78. M.Arrabito, S.Bodoardo, N.Penazzi, S.Panero, P.Reale, B.Scrosati, Y.Wang, X.Guo, S.G.Greenbaum, J. Power Sources, 97-98 (2001) 478.

79. J.G.Powles, P.Mansfield, Phys.Lett., 2 (1962) 58.

80. J.B.Goodenough and A.L.Loeb, Phys.Rev., 98 (1955) 391.

81. J.Mason, Multinuclear NMR, Plenum Press, New York, 1987.

82. G.A.Webb, Annu Rep. NMR Spectrosc, 6A (1975) 1.

83. P.C.Taylor, J.F.Baugher and H.M.Kriz, Chem.Rev., 75 No.2 (1975) 203.

84. E.R.Andrew, A.Bradbury, R.G.Eades, Nature 182 (1958) 1659.

85. I.J.Lowe, Phys.Rev.Lett., 2 (1959) 285.

86. Y.J.Lee, F.Wang, C.P.Grey, J.Am.Chem.soc., 120 (1998) 12601.

87. Y.Wang,J.Sakamoto,C.K.Huang,S.Surampudi, and S.G.Greenbaum, Solid State Ionics, 110 (1998) 167.

88. Y.Wang, V.Yufit, X.Guo, E.Peled, and S.G.Greenbaum, J.Power Sources 94 (2001) 230.

89. L. Vegard, Z. Phys. **5** (1921) 17.

90. L.Vegard, Z.Krist., 6 (1928) 239.